A TES Detector for ALPS II

Characterising a cryogenic, low-background,
low energy single photon detector

Dissertation

submitted for the award of the title
“Doctor of Natural Sciences”

to the Faculty of Physics, Mathematics, and Computer Science
of Johannes Gutenberg University Mainz
in Mainz

Rikhav Shah
born in Mumbai

Mainz, November 30, 2022

Rikhav Shah
A TES Detector for ALPS II

Date of Exam: 26 October, 2022

JGU Mainz
Institute for Physics
Staudingerweg 7
55128 Mainz

Declaration

I declare that I have written this thesis independently, and have not used any sources or aids other than those specified, and have identified quotations.

Hamburg, November 30, 2022

Rikhav Shah

Abstract

Axions are Weakly Interacting sub-eV Particles (WISPs) predicted to explain phenomena like the lack of Charge-Parity (CP) violation in Quantum Chromodynamics (QCD). With axion-like-particles, they can also contribute to dark matter and explain other astrophysical phenomena. These particles can couple to photons, a process used in most experiments attempting to search for them. One such experiment is ALPS II, a light-shining-through-a-wall experiment. Photons stored in an optical cavity can convert to axions or axion-like-particles, aided by the presence of a magnetic field. These can traverse an opaque wall and, in another such optical cavity, reconvert to photons which can be detected. The rate of these low energy (1.165 eV) 1064 nm photons comprising the signals for ALPS II is $\mathcal{O}(10^{-5})$ cps. A Transition Edge Sensor (TES) can prove to be a suitable candidate to detect them. This sensor exploits the drastic dependence of the resistance of a superconducting microchip near its transition temperature, which can detect the incidence of a photon (as energy) on it from a macroscopic change in its resistance. The characterisation of a such a TES system to serve as a detection scheme for ALPS II is covered by this work.

Firstly, the setup and design of this scheme is detailed with its defining features and readout with SQUIDs (Superconducting Quantum Interference Devices). It is housed in a dilution refrigerator capable of stably cooling down to temperatures $<$30 mK. The working, response and operation of this TES system and SQUID readout is detailed, readying it for the reception of signals and background alike with a data acquisition and processing scheme.
Secondly, the analysis of these TES pulses is discussed. Here, the pulses can be fit with a variety of fitting schemes (as best suited to the TES) and studied with a PCA (Principal Component Analysis) as well. The application of these procedures yields an energy resolution $\Delta E/E \sim 7 - 12\%$ for 1064 nm photons. The fitting scheme which best assimilates the data in a TES pulse is adopted as the baseline for pulse characterisation and forms the basis for a pulse selection procedure.
Thirdly, the discussion turns to background events inveigling the detection scheme. For use in ALPS II, a background rate of $8.1 \cdot 10^{-6}$ cps over 20 days of data taking is the upper

limit for the detector, assuming a detection efficiency of 50%. The backgrounds are split into extrinsic and intrinsic backgrounds i.e. those detected with an optical fiber coupled to the TES and those detected without. It is essential to substantiate the viability of the TES for use in the ALPS II experiment. In order to do this, a 20 day intrinsic background dataset is subjected to the pulse selection procedure(s), resulting in a rate of $6.9 \cdot 10^{-6}$ cps, with a 1064 nm-photon selection $\geq$ 90%. Considering the intrinsic backgrounds, the TES is thus viable for use in the ALPS II experiment.
A setup to measure the detection efficiency of the system has also been developed and is also described. This influences the extrinsic background events detected. The first measurements with this setup have resulted in an efficiency of at least 5% and will be optimised. The backgrounds can in general originate from a variety of sources including cosmic rays and radioactivity, but are suspected to be dominated by photons from blackbody radiation and their pile-ups. To suppress this, hardware options such as an in-cold filter bench and fiber curling are being investigated for use in the main detection line to the TES. Testing these suppression methods forms the next series of investigations for the TES system along with background studies, simulations, and the use of machine learning techniques for pulse analysis. These forthcoming steps form the efforts to fully characterise the TES detection system in preparation for ALPS II.

Zussammenfassung

Axionen sind prognostizierte *Weakly Interacting sub-eV Particles* (WISPs), die Phänomene wie das Fehlen der Ladungs-Paritäts-Verletzung (CP-violation) in der Quantenchromodynamik (QCD) erklären sollen. Mit axion-like-particles (ALPs) können sie auch zur dunklen Materie beitragen und sich auch in der Lage bestimmte andere astrophysikalische Phänomene zu erklären. Diese Teilchen können an Photonen koppeln, ein Prozess, der in den meisten Experimenten, die nach ihnen suchen, genutzt wird. Ein solches Experiment ist ALPS II, ein sogennantes *light-shining-through-a-wall* Experiment. In einem optischen Hohlraum, gespeicherte Photonen können sich (in Präsenz eines Magnetfeldes) in Axionen oder ALPs verwandeln. Diese können eine undurchsichtige Wand durchqueren und sich in einem anderen optischen Hohlraum wieder in Photonen verwandeln (auch in Präsenz eines Magnetfeldes), die detektiert werden können. Die Rate dieser niederenergetischen (1,165 eV) 1064 nm-Photonen, aus denen die Signale für ALPS II bestehen, beträgt $\mathcal{O}(10^{-5})$ cps. Ein Übergangskanten-Sensor (*Transition Edge Sensor*, TES) kann sich als geeigneter Kandidat für deren Detektion erweisen. Dieser Sensor macht sich die drastische Abhängigkeit des Widerstands eines supraleitenden Mikrochips in der Nähe seiner Übergangstemperatur zunutze, der das Auftreffen eines Photons auf ihn anhand einer makroskopischen Änderung seines Widerstands erkennen kann. Die Charakterisierung eines solchen TES-Systems, das als Detektionssystem für ALPS II dienen soll, ist Gegenstand dieser Arbeit.

Zuerst wird der Zusammensetzung und die Aufbau dieses Systems, inklusive charakteristischen Merkmalen und der Auslesung mit SQUIDs (supraleitende Quanteninterferenzgeräte) beschrieben. Das Detektionssystem befindet sich in einem Verdünnungskryostaten, der in der Lage ist das Detektionssystem stabil auf Temperaturen <30mK herunterzukuehlen. Die Funktionsweise und der Betrieb dieses TES-Systems und der SQUID-Auslese werden detailliert beschrieben, sodass es auf den Empfang von Signalen und Hintergrundsignalen mit einem Datenerfassungs- und Verabeitungsschema vorbereitet ist.
Zweitens wird die Analyse dieser TES-Pulse erörtert. Hier kann der Puls mit einer Vielzahl von Anpassungsschemata (die für die TES am besten geeignet sind) angepasst und auch mit einer Hauptkomponentenanalyse (Principal Component Analysis, PCA) untersucht werden. Die Anwendung dieser Verfahren ergibt eine Energieauflösung $\Delta E/E \sim 7 - 12\%$ für 1064 nm Photonen. Das Anpassungsschema, das die Daten in einem TES-Puls am besten assimiliert, wird als Grundlage für die Pulscharak-terisierung angenommen und bildet die Grundlage für ein Pulsauswahlverfahren.

Drittens werden Hintergrundereignisse erörtert, die das Nachweisverfahren stören. Für die Verwendung in ALPS II ist eine Untergrundrate von $8,1 \cdot 10^{-6}$ cps über 20 Tage der Datenaufnahme die Obergrenze für den Detektor, wobei eine Detektionseffizienz von 50% angenommen wird. Die Untergründe werden in extrinsische und intrinsische Untergründe unterteilt, d. h. in solche, die mit einer an den TES gekoppelten optischen Faser detektiert werden, und solche, die ohne diese Faser detektiert werden. Es ist wichtig, die Eignung des TES für das ALPS II-Experiment nachzuweisen. Zu diesem Zweck wird ein 20-tägiger intrinsischer Untergrund-datensatz dem Pulsselektionsverfahren unterzogen, was zu einer Rate von $6,9 \cdot 10^{-6}$ cps führt, mit einer 1064 nm-Photonenauswahl $\geq$ 90%. In Anbetracht der intrinsischen Untergründe ist das TES somit für den Einsatz im ALPS II-Experiment geeignet.
Ein Aufbau zur Messung der Detektionseffizienz des Systems wurde ebenfalls entwickelt und wird beschrieben. Diese beeinflusst die erfassten extrinsischen Untergrundereignisse. Die ersten Messungen mit diesem Aufbau haben eine Effizienz von mindestens 5% ergeben und werden noch optimiert werden. Die Untergründe können im Allgemeinen aus einer Vielzahl von Quellen wie kosmischer Strahlung und Radioaktivität stammen, aber es wird vermutet, dass sie von Photonen aus Schwarzkörperstrahlung und deren Anhäufungen (Pile-Ups) dominiert werden. Um dies zu unterdrücken, werden Hardware-Optionen wie eine Filterbank und Faser-Biegung für den Einsatz in der Hauptnachweisleitung zum TES untersucht. Die Erprobung dieser Unterdrückungsmethoden bildet die nächste Untersuchungsreihe für das TES-System, zusammen mit Untergrundstudien, Simulationen und dem Einsatz von maschinellen Lernens für die Pulsanalyse. Diese bevorstehenden Schritte bilden die Bemühungen zur vollständigen Charakterisierung des TES-Detektionssystems in Vorbereitung auf ALPS II.

Contents

1 Introduction

> *Wake! For the sun, who scatter'd into flight*
> *The stars before him from the field of night,*
> *Drives night along with them from heav'n, and strikes*
> *The sultan's turret with a shaft of light.*
>
> — **Omar Khayyám**
> (from *The Rubáiyát*)

Ever newer experiments in the world of particle physics are looking for ever fainter signals, from rarer and hitherto undetected physical processes. New and revolutionary physical frameworks are anticipated to explain these phenomena, like dark matter and dark energy, and their origins, which are not in the purview of Standard Model (SM) physics. Physical models stretching known frameworks like the SM are also expanded to investigate what currently makes up the unknown. These require increasingly precise measurements and, by extension, increasingly sensitive detectors. Advancements in detector technologies has also opened up newer fields of research, offering new methodologies with which physical models can be substantiated. Extraordinary demands and constraints on detectors of varying types has become a mainstay of fundamental physics.

The current understanding of the physical universe requires more than what the SM - as it currently stands - has to offer [1]. The discovery of the Higgs boson [2, 3] may have completed it, but there are hints at the existence of particles and interactions beyond those in the SM framework, as will be discussed next.
Prominent among these missing features are the understanding of dark matter and dark energy and matter-antimatter asymmetry. Others include the lack of Charge-Parity (CP) violation within Quantum Chromodynamics (QCD) [4] (from fine-tuning considerations). Using the SM to describe the particle nature explaining these anomalous phenomena has led to the investigations of different particles such as Weakly Interacting Massive Particles (WIMPs) [5], and supersymmetric particles [6] (which can also comprise WIMPs) at high energies achievable at the Large Hadron Collider (LHC), and with other searches (for

dark matter candidates). These have not turned up any uncontested results [7] and in their absence, interest has also been focused on the smaller and lighter - and just as difficult to find - particles. Among these are WISPs (Weakly Interacting sub-eV Particles), a class of extremely light particles exhibiting very faint interaction with SM particles. The world of axion physics exists in this liminal space, with suggestions of its existence from multiple unexplained phenomena from astrophysics, QCD and cosmology. In extensions of the SM, the axion field(s) can solve these seemingly disparate problems of the CP conservation in QCD and be a viable candidate for cold dark matter.

Axions and axion-like-particles can couple to photons which is the basic mechanism used in most axion and axion-like-particle search experiments. Various types of such experiments can be realised, one of which is the ALPS II experiment. This features a unique implementation of lasers and optical cavities in a magnetic field: photons from a laser, stored in an optical cavity can convert to axions or axion-like-particles, aided by the presence of a magnetic field. These can travel across an opaque wall, and reconvert to photons in another optical cavity, also in the presence of a magnetic field. The rate of these low energy (1.165 eV) 1064 nm photons comprising the signals for ALPS II is $\mathcal{O}(10^{-5})$ cps, or about 1 photon per day. This necessitates a the detection system which can detect low-energy near-infrared single photons with an ultra-low background level, high efficiency and stable long term operation; making a Transition Edge Sensor (TES) an ideal candidate for such an experiment. The characterisation, operation and analysis of such a photon detector to search for the telltale signal photons is described.
Succinctly, this work:

- motivates the theoretical background for the existence of axions and axion-like-particles, and the technical design and experimental setup of the ALPS II experiment, in Chapter 1. Here, the detection requirements corresponding to the experiment are also discussed.

- describes the design, setup and operation of the TES in Chapter 2, along with its readout scheme. This section includes the theoretical response and working of the detector, the corresponding readout, its housing, and chosen operation settings. The setup of the detector in its cryogenic environment is also described.

- describes the analysis of detector signals in Chapter 3, with the multiple approaches used to understand data pulses. Traditional fitting methods and an analysis using

principal components (PCs) are employed. These differing approaches are compared and contrasted so as to achieve the best description possible of the signals, and obtain parameters that can then be used for pulse discrimination.

- delves into the backgrounds that can limit the viability of the detector setup in Chapter 4, and how pulse discrimination schemes are used to alleviate the influence of background events. The pulse selections algorithms developed are based on fit parameters described in Chapter 3. This selection scheme is further fine-tuned, and is used to suppress the background pulses to ultra-low levels. This section also discusses the broad types of backgrounds in the detector and the setup used to measure the detection efficiency. Strategies to reduce the influence of these backgrounds are discussed, focusing on the challenges involved in the final setup with ultra-low background levels and a high efficiency.
- presents the final results and status in the concluding Chapter 5, and outlines the next steps in the investigations necessary for the detection system.

Parts of this thesis have also been published in [8] and presented in [9].

1.1 Axions and axion-like-particles

A missing feature of the SM is an explanation of the experimentally observed lack of CP violation in the QCD sector. The general QCD Lagrangian features the CP-violating term:

$$\mathcal{L}_{QCD} \supset \mathcal{L}_{CP\ violating} = \frac{\alpha_s}{4\pi}\theta\,\mathrm{tr}\,G_{\mu\nu}\tilde{G}_{\mu\nu} \tag{1.1}$$

where α_s is the strong coupling, θ is an angle parameter $\in [0, 2\pi]$ (CP-violating parameter), and $G_{\mu\nu}$ is the gluonic field strength with its conjugate $\tilde{G}_{\mu\nu}$. CP violation is not ruled out but is not experimentally indicated or detected [10].
With the measurement of the neutron electric dipole moment $|d_n| < 6.3 \cdot 10^{-26}\,e$-cm [11], the effective CP-violating angle parameter $\bar{\theta} \equiv \theta + \det \mathcal{M}$ has an upper bound [12]:

$$\left|\bar{\theta}\right| \leq 10^{-10}, \tag{1.2}$$

where $\mathcal{M}$ is the quark mass matrix. As θ can take any value ($\theta \in [0, 2\pi]$), this value is very small and is understood as a fine-tuning feature. This fine-tuned aspect can be explained by extensions of the SM to include additional symmetries which can explain Eq. 1.2. The first such solution was proposed by Peccei and Quinn [13, 14] by 1978 [15], which essentially upgrades the parameter θ to a dynamical field spontaneously relaxing to zero. This spontaneous breakdown of the chiral $U(1)_{PQ}$ symmetry generates a very light pseudoscalar Nambu-Goldstone boson, the aptly[1] named axion [16]. As its existence is motivated by QCD, it is called the QCD axion. There are also other solutions to the CP problem without the postulation of axions, but these have no convincing framework so far and/or may not provide any experimental technique with which any described mechanism may be tested [17].

The axion models used (as extensions to the SM) can vary, with the conservative benchmark DFSZ[2] [18] and KSVZ[3] [19] models featuring an axion with very faint coupling to SM particles. Other models, like the clockwork axion model [20] or $\mathbb{Z}_N$ model [21], though they involve stronger coupling to SM particles and may make the axion more 'visible' (easier to detect) as a result, increase in complexity drastically with the addition of extra fields, etc. More recent models include, for example, one focusing on total asymptotic freedom [22], and others such as the one with a photophilic hadronic axion

[1] Named for a washing detergent of the same name.
[2] Dine-Fischler-Srednicki-Zhitnitsky (DFSZ) model
[3] Kim-Shifman-Vainshtein-Zakharov (KSVZ) model

[23]. The latter puts the axion squarely in the parameter range that can be probed by the ALPS II experiment.
The axions a have a small but non-vanishing mass, due to their coupling to gluons. This is given by [12]:

$$m_a \approx \frac{m_\pi f_\pi}{f_a} \approx 0.6\,\text{meV} \times \left(\frac{10^{10}\,\text{GeV}}{f_a}\right) \tag{1.3}$$

where m_a, m_π are the axion and pion masses and f_π the (pion) decay constants. f_a determines the strength of the interaction of the axion with SM particles. The weak coupling of the axions to photons is given by the interaction Lagrangian $\mathcal{L}_{a\gamma\gamma}$ (as would be the case for any such pseudoscalar particle):

$$\mathcal{L}_{a\gamma\gamma} = -\frac{1}{4} g_{a\gamma\gamma} a F_{\mu\nu} \tilde{F}^{\mu\nu} = g a \vec{E} \cdot \vec{B}, \tag{1.4}$$

which is highly suppressed [24]:

$$g_{a\gamma\gamma} = \frac{\alpha}{2\pi f_a} C_{a\gamma\gamma}\ , \tag{1.5}$$

where $C_{a\gamma\gamma}$ is a model-dependent constant. This coupling is expected to be very small, but if axions exist, can result in observable results which can occur wherever large or strong enough electromagnetic fields are concerned - in astrophysics [25] or manufactured laboratory environments, as will be discussed in the following section.
The generic axion-like-particle (henceforth referred to as an ALP) does not fall within the purview of the QCD physics, as it does not pose a solution to the CP problem. These are motivated mainly by the symmetries which are broken at high energies, in a similar fashion to axions, and are also pseudo Nambu-Goldstone bosons. They are also unconstrained by the mass-coupling relation necessary to QCD axions and can consequently span a wider range. They are a consequence of the top-down view of string theory, where they are the compactifications of the spatial dimensions [26, 27] and also feature in dark energy [28]. Other WISP candidates include hidden photons, minicharged particles and hidden $U(1)$ gauge bosons [29].

By hints and bounds

The theoretical motivation for the existence of axions and ALPs, as discussed in the section above, is appended by other hints that WISPs can exist. These are laid out below:

- **Cold Dark Matter (CDM)**: Axions are prime candidates for cold dark matter which could have been produced non-thermally in significant quantities in the early universe [30, 31]. The Bose-Einstein condensation of axions, which gain their mass m_a after temperatures drop below the GeV scale, could explain CMB anisotropies [32] and caustic rings in the rotational curves of some galaxies [33], as described in [34].

- **TeV transparency**: The high transparency of the universe to TeV radiation [35] could be explained by their conversion to ALPs and reconversion to photons near the Earth [36] or in intergalactic magnetic fields [37]. Bounds on $g_{a\gamma\gamma}$ from these hints can be seen in [38].

- **Stellar Cooling and White Dwarfs**: WISPs, rarely produced though they may be in the stellar interiors, can escape with some energy and thus contribute to the overall energy loss [39]. The general ALP-photon coupling from the observation of horizontal branch stars in globular clusters provides the strongest coupling ($g_{a\gamma\gamma}$) constraints for this [40]. The Sun is not as strong a possible emitter as other stars but provides a limit nonetheless on the coupling [41] and is used for experiments looking for WISPs, discussed in the following section. The anomalous cooling in the white dwarf luminosity function could be explained by axions [42], corresponding to an axion-photon coupling of $g_{a\gamma\gamma} \sim 10^{-12}\,\text{GeV}^{-1}$.

- Additional hints for WISPs (and bounds on the corresponding coupling $g_{a\gamma\gamma}$) are also derived from Big Bang nucleosynthesis, the cosmic microwave background, and observation of the supernova 1987A (and others); these are also summarised in [12].

1.1.1 Experimental Searches

The main searches for axions and ALPs, based on $g_{a\gamma\gamma}$, are divided into three categories, depending on what probable source or guiding model is being investigated for their existence. The important interaction that drives most ALPs search experiments is the Primakoff-like Sikivie effect [43] describing photon-ALP conversions in the presence of a magnetic field (Figure 1.1). These are (adapted from [44] and others as mentioned):

- **Haloscopes**: These investigate the ALPs that could make up the dark matter halo in the center of galaxies. Haloscopes typically use microwave cavities where axions or

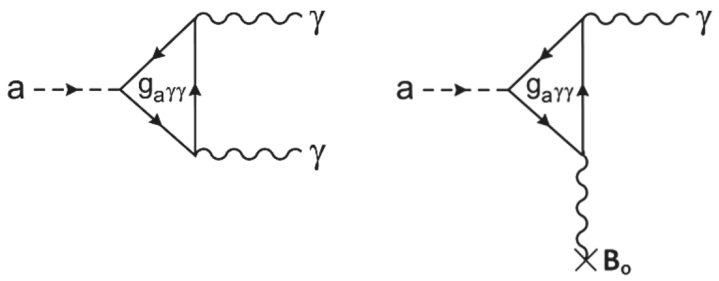

Fig. 1.1.: The Feynman diagrams for the photon-ALP conversion is shown above, where a is the axion field, γ is the photon, and B_0 is the magnetic field. The diagram to the right shows the inverse Primakoff-like Sikivie effect used to great effect in axion and ALP search experiments. Figure from [45].

ALPs can resonantly convert to a quasi-monochromatic signal in a strong magnetic field; the signal is extracted from the cavity by an antenna. Haloscopes, like ADMX (Axion Dark Matter Experiment [45]), scan a restrictive mass range due to resonance requirements but can probe large swaths of the coupling $g_{a\gamma\gamma}$ and the limits assume that the dark matter consists of axions only. This is exemplified in Figure 1.2. Such searches are model-dependent, factoring in the rotational velocity of the Earth through the halo, and density of the axionic dark matter. Other experiments like CASPEr (Cosmic Axion Spin Precession Experiment) [46] seek to probe the axionic dark matter by detecting the spin precession caused by it, using NMR (Nuclear Magnetic Resonance) techniques.

- **Helioscopes**: These investigate the axions that could be emitted by the Sun, which can lose energy due to the production and propagation of axions and ALPs. The inverse Primakoff-like Sikivie effect is used again here in the detection: an optical cavity in the presence of a strong magnetic field trails the sun, with incoming axions or ALPs converting to signal photons. Helioscopes such as CAST (CERN Axion Solar Telescope) [47] are shown in blue in Figure 1.2. Helioscopes are also model dependent (though to a lesser extent than haloscopes), and newer generations of these are being developed like IAXO[4] (International Axion Observatory) [49] also mentioned in Figure 1.2.

- **LSW (Light-Shining-through-a-Wall) Experiments**: These investigate the existence of axions and ALPs in a purely laboratory-based setting, without the use of any astrophysical sources, in a model-independent approach. This is done by using

[4]After the prototype babyIAXO [48], the only ones being currently developed.

two optical cavities; photons in the first cavity can be converted to axions/ALPs in the presence of a magnetic field. These can pass an opaque barrier or wall and enter the second cavity where they can be reconverted to photons in the presence of another magnetic field. This regenerated photon is the signal, and can be detected with an appropriate photon detector. If a photon signal will be detected behind this wall, this would be a strong evidence for physics beyond the SM. The coupling that such experiments have probed is shown in gray in Figure 1.2. ALPS I (Any Light Particle Search) [50] at DESY had the best limits for LSW experiments, which were then augmented by OSQAR (Optical Search for QED Vacuum Bifringence, Axions and Photon Regeneration) [51] and this will be bettered multifold by the ALPS II experiment.

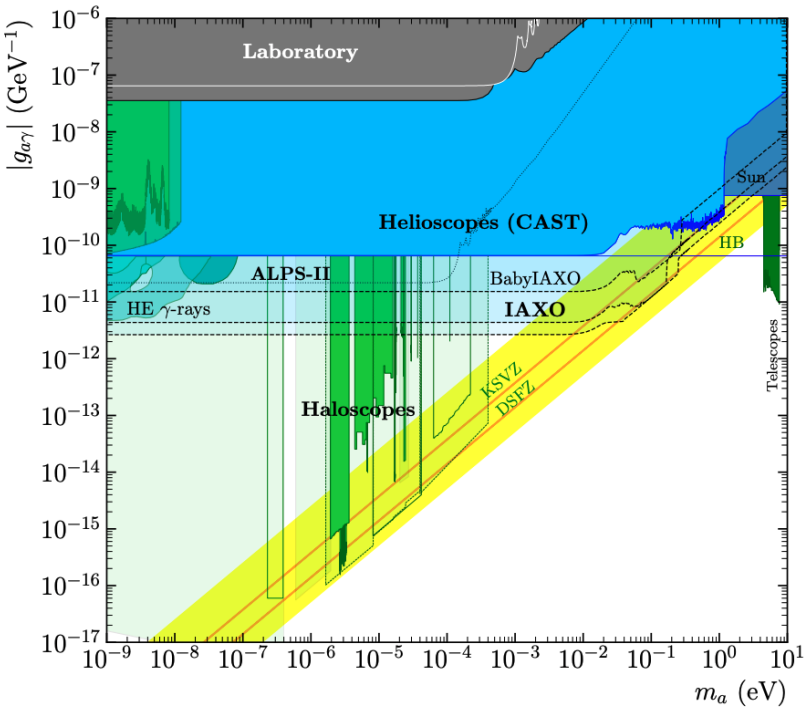

Fig. 1.2.: The sensitivity plot is shown above for the coupling $g_{a\gamma\gamma}$ and the ALP mass m_a. Some benchmark QCD axion models are shown in the yellow band, and with some other parameter spaces of interest from constraints set by HB (Horizontal Branch) stars and high energy γ rays are shown as well. The new parameter space investigated by upcoming experiments like ALPS II are shown with dotted or dashed boundaries. Figure from [48].

For a LSW experiment, the signal rate ($\dot{\eta}_{det}$, from the reconverted photons) is given by [52]:

$$\dot{\eta}_{det} = \eta P_{\gamma\to a} P_{a\to\gamma} \dot{\eta}_{produced}, \tag{1.6}$$

where $P_{\gamma\to a}$ is the probability of a photon to convert to an axion or ALP (vice versa for $P_{a\to\gamma}$), $\dot{\eta}_{produced}$ is the rate at which photons are produced at the source in the first cavity and η is a generic detection efficiency taking into account the full detector line. The probabilities P are given by the following equation, for a photon or an axion/ALP travelling a homogenous magnetic field with strength B over a length L [44]:

$$P_{a\leftrightarrow\gamma} = \frac{1}{4}\frac{\omega}{k_a}\left(g_{a\gamma\gamma}BL\right)^2 |F(qL)|^2, \tag{1.7}$$

where ω is the photon energy, k_a; $(k_a^2 = \omega^2 - m_a^2)$ is the axion momentum, and q is the momentum transfer to the magnetic field $q \equiv n\omega - \sqrt{\omega^2 - m_a^2}$ where n is the refractive index. $F(qL)$ is a form factor, which, for a contiguous homogenous magnetic field along an axis over a length L, is given by:

$$|F(qL)|^2 = \left[\frac{2}{qL}\sin\left(\frac{qL}{2}\right)\right]^2, \tag{1.8}$$

which gives the probed parameter space (Figures 1.2) its distinctive oscillation pattern as the mass m_a increases, which is then damped. For lower masses this parameter space is relatively flat. The design of LSW experiments aims to achieve $F \sim 1$ as much as possible, for a wide range in the mass $m_a << \omega$. With $n = 1$ and $\frac{qL}{2} << 1$, we get:

$$P_{a\leftrightarrow\gamma} = \frac{g_{a\gamma\gamma}^2 B^2 L^2}{4} \tag{1.9}$$

Other optical LSW setups (beside ALPS I [50]) included LIPSS (Light Pseudoscalar and Scalar Search) [53] at Jefferson Lab, GammeV [54] at Fermilab, OSQAR [51] at CERN[5] as well as LSW setups with BMV (Birefringence Magnétique du Vide) [55] and BFRT (Brookhaven-Fermilab-Rochester-Trieste, Collaboration) [56].

[5] European Council for Nuclear Research

1.2 The ALPS II Experiment

The Any Light Particle Search (ALPS) II is a laboratory-based LSW experiment in Hamburg. It succeeds the ALPS I experiment, and is set up and will be operated in a straight section of the HERA[6] tunnel. Compared to ALPS I, the final stage is expected to probe an overall sensitivity increased by three orders of magnitude [57]. Though this covers limits set from astrophysical observations and helioscope results, ALPS II will test regions which overlap with further astrophysical hints or possible (ALP and axionic) cold dark matter regions.
The essential make up of the experiment (shown schematically in Figure 1.3) consists of:

- **Production Cavity** (PC) and **Laser Input**: The optical cavity in front of an opaque wall, where photons are introduced and stored to increase the light power by a factor $\mathcal{F}_{PC}$, related to the cavity finesse. Light with a wavelength of 1064 nm from a high powered laser (30 W, upto 70 W) will be introduced in the PC. The stored energy will be built up due to this high cavity finesse. This cavity is in a magnetic field B, in whose presence the photons can convert to axions/ALPs.

- **Regeneration Cavity** (RC): The RC is a cavity similar to the PC, also in the magnetic field B, where a generated axion/ALP can reconvert to a photon. This cavity is beyond the light-tight wall, and has a power build-up factor $\mathcal{F}_{RC}$. This cavity is mode-matched to the PC, allowing for the resonant regeneration of photons which enables significant improvements in experimental sensitivity [57].
  These are high-finesse cavities, propagated through two strings of 12 HERA dipole magnets (i.e. 12 per cavity) each, and each magnet string has a length ∼105 m.

- **Magnetic Environment**: The superconducting magnets from the erstwhile HERA accelerator are repurposed and upcycled for use in ALPS II after being straightened [58], which required significant effort. Each magnet is 8.8 m long, will have a current of 5.7 kA flowing through it and will achieve a magnetic field of $B = 5.3$ T, resulting in a magnetic field length $BL \sim 560$ Tm on either side of the wall.

- **Central Optical Bench** (COB): The wall is realised as a shutter (and the mirrors in the cavities) on the central optical bench. This also includes a setup to hold them on resonance with each other [59], realised with the use of a 532 nm laser locking system. This is in particular for the TES system being the detection scheme for ALPS II.

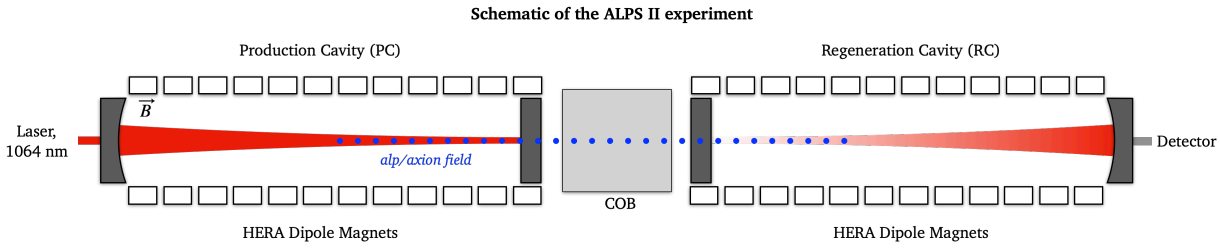

Fig. 1.3.: The general schematic diagram of the ALPS II experiment is shown above.

The final component of ALPS II is the detection scheme, such that the regenerated single photons can be reliably detected; this is detailed in Section 1.3. The upgrades to ALPS II from ALPS I are discussed in more detail in [57], and are summarised in short here:

- **Signal photons**: 1064 nm light is used in the optical setup due to the availability of optical equipment for this wavelength. One crucial technical reason is the stability of the high efficiency end mirrors in the resonant cavities: ALPS I struggled with damaged mirrors due to the 532 nm light used. These form the signal photons that can be detected after they are resonantly regenerated in the RC. The reduction in the energy of the signal photons poses significant challenges when it comes to detection, and also the reduction of backgrounds when using the requisite detection scheme.
- **Magnetic Length**: ALPS I used only one HERA dipole magnet (straightened) for the PC and RC, while ALPS II will use 12 such dipoles for each.
- **Power build-up**: The finesse of the optical cavities is enhanced. This improves the power built up in the PC from 1 kW to 150 kW and by a factor of 40,000 in the RC, compared to ALPS I.

The probability of a photon being regenerated in such a setup is given by using Eq.s 1.7, 1.9, which need to be modified for the presence of multiple non-contiguous magnetic fields [60]. This is done and given by the overall probability $P_{\gamma\to a\to\gamma}$ [44]:

$$P_{\gamma\to a\to\gamma} = \frac{1}{16}\mathcal{F}_{PC}\mathcal{F}_{RC}\left(g_{a\gamma\gamma}Bl\right)^4 \tag{1.10}$$

$$= 6\cdot 10^{-38}\cdot\mathcal{F}_{PC}\cdot\mathcal{F}_{RC}\cdot\left(\frac{g_{a\gamma\gamma}}{10^{10}\,\mathrm{GeV}^{-1}}\,\frac{B}{1\,\mathrm{T}}\,\frac{l}{10\,\mathrm{m}}\right)^4 \tag{1.11}$$

[6]Hadron Elektron Ring Anlage

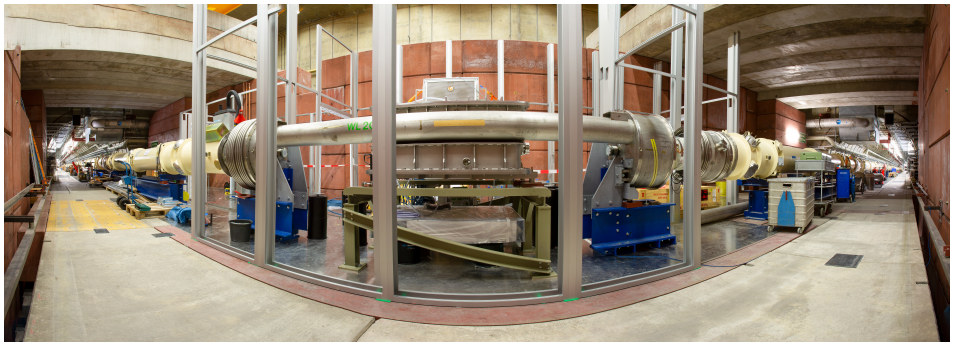

Fig. 1.4.: A panorama shot of the ALPS II experimental hall is shown above, in HERA North (DESY). The central clean room is in the centre with the magnet strings for the production and regeneration cavities to the left and right respectively; all the magnets have been installed and tested with a cool down to 4 K and a current of 5.7 kA through them. Construction of the clean rooms has also been completed.

ALPS II was originally planned as a series of three sub-experiments (ALPS IIa, b, and c), but the final version of the version (i.e. ALPS IIc, Figure 1.4) is the only one described and summarised here for purposes of brevity and for discussion of the detection system. ALPS IIb was not realised. The detailed setup is found in [57]. The detector part of the experiment will be discussed in the following section.

1.3 Detection requirements

Following from Eq.s 1.10, 1.6, the final number of regenerated photons, when probing the coupling $g_{a\gamma\gamma} = 2 \cdot 10^{-11}$ GeV^{-1}, corresponds to a power of $\sim 10^{-24}$ W. This translates to an expected photon rate $\dot{\eta}_{produced} \sim 2.8 \cdot 10^{-5}$ cps. These signal photons are 1064 nm (1.165 eV) single photons. A sensitivity for the ALP-photon coupling $S\left(g_{a\gamma\gamma}\right)$ can be found [52]:

$$S\left(g_{a\gamma\gamma}\right) \propto \frac{1}{BL}\left(\frac{DC}{T}\right)^{\frac{1}{8}}\left(\frac{1}{DE \cdot \mathcal{F}_{PC} \cdot \mathcal{F}_{RC} \cdot \dot{\eta}_{produced}}\right)^{\frac{1}{4}} \tag{1.12}$$

$$\implies S\left(g_{a\gamma\gamma}\right) \propto \left(\frac{\sqrt{DC}}{DE}\right)^{\frac{1}{4}} \tag{1.13}$$

where DC is the dark count (DC) rate of the detector, DE its detection efficiency, T the measurement time, $\mathcal{F}_{PC,\ RC}$ the power build up factors, and $\dot{\eta}_{produced}$ the rate of photon

production in the PC. This necessitates important criteria for a detector that can be used for ALPS II:

- **Low Energy Photon Detection**: The signal comprises low energy near-infrared (IR) single 1064 nm photons. The chosen detector has to be sensitive to these low energies of approx. 1 eV.
- **Low DC**: The dark count rate of the detector has to be comparably low with respect to the regenerated photon rate of $\mathcal{O}(10^{-5})$ cps. This rate, importantly, is before any photons are introduced to the detector line, which can entail significant losses as well due to connections and couplings.
- **High DE**: In order to best detect photons with such a low signal rate over this detection line, the (quantum) detection efficiency of the detector itself must be comparably high.
- **Stability**: The data taking time T which is required to achieve a good enough sensitivity to the coupling is enhanced by a detector with good long-term stability of operation.
- **High Energy Resolution** (ER): To detect the photons, a good energy resolution of at least $16 - 20\,\%$ is needed. This energy resolution $\Delta E/E$ corresponds to the resolving power $E/\Delta E \approx 5 - 6$ [57]. The signal photon pulses can be significantly overrun by backgrounds at the ultra-low levels ($\mathcal{O}(10^{-5}, 10^{-6})$ cps), and a high ER can help with signal discrimination, especially when it comes to distinguishing signal 1064 nm photons from the 532 nm photons which will be used to lock the cavities and can make their way to the detector.

1.4 ALPS II: Detection Schemes

For ALPS II, two detection systems are foreseen to be used: the Heterodyne and TES schemes. These feature different systematics, and the Heterodyne scheme will be implemented in the experiment first. Following a science run with this, the TES detection system will succeed it.

Heterodyne Scheme

The heterodyne detection system uses the coherence between the axion production and photon regeneration processes in ALPS II. It can detect very weak photon fields, at the

shot-noise limit, as demonstrated in [61]. The mixing of the regenerated field with a much stronger optical field, called a local oscillator (LO) field, a 'beat note' varying in time at the frequency difference of the two fields can be generated. This beat signal is a measure of the amplitude and the phase of the field regenerated in the RC. However, this method entails more stringent requirements on the phase and long-term stability of the setup [62, 63]. The fundamental limit is the Poissonian shot noise of the LO, which decreases over integration time; the heterodyne scheme can achieve low enough background levels $\mathcal{O}(10^{-5})$ cps. The results of this detection scheme can and will be in turn checked by the TES when it will be connected to ALPS II after the heterodyne run will be completed. The TES will be able to resolve the signal photon energy and, in effect, complete the picture of what the heterodyne scheme could detect.

1.4.1 A Suitable TES

The burgeoning field of cryogenic single photon detectors [64] can provide sensitive detectors which can be used for such searches. Superconducting photon detectors can cover an exceptionally broad range of energies, from high-energy gamma and X-rays ($>$100 eV) through to terahertz (10^{-3} eV) frequencies. These typically have an intrinsically low dark count rate due to reduced thermal noise [65]. These include superconducting tunnel junctions (SJTs), microwave kinetic inductance detectors (MKIDs or KIDs), superconducting nanowire single photons detectors (SNSPDs) or TESs. The main mode of operation in these devices is the read-out, usually using SQUIDs (Superconducting QUantum Interference Devices), of short-lived phenomena like a resistance or induction change upon the incidence of a single photon on the detector (Section 2.2).

Of these, using a TES offers possible tailor-made solutions and meets the requirements of a detector scheme for ALPS II. TESs have nearly no innate dark counts (save for those which may come from the setup realised), and have no dark currents like a CCD (charged-couple device) sensor. A CCD was used for ALPS I but has a dark current-induced dark rate of $\mathcal{O}(10^{-3})$ cps [57] and (in principle) lower efficiency to detect 1064 nm photons.

TESs have been realised for a profusion of purposes, from astronomy experiments, neutrino mass experiments, and DM searches to quantum optics. They have achieved measurably better energy resolution than other, more traditional, semiconductor - based devices on that front, though at energies typically $\sim$keV [66]. The ambit of this work

aims to describe the successful detection and characterisation of single 1064 nm photons in the TES, to show that a TES can reach the sufficiently low backgrounds required for ALPS II, and with the long-term stable operation needed. In the scope of this work, the characterisation of the TES and its operation in the cryogenic environment will be undertaken. This involves understanding the response of the TES and its working points, the analysis of the corresponding pulses for signal and background photons. The long term stability and correspondingly low background rate of the TES need to be investigated and confirmed such that further operation of the TES will be continued for its use in ALPS II. This then gives way to calculating other detection parameters and TES properties such as its efficiency.

2 Detector and Readout

In this section, the working of a TES will be described, its readout with SQUIDs will be detailed, and its setup in a cryogenic environment will be elaborated on. The response of the TES will be theoretically explained following the work of Irwin and Hilton [67]; which builds on the work of McCammon [68] by considering the inductance of the TES circuit and its effects on stability and operation. The formalism of the TES response is broken down into its electrical and thermal components, following Irwin and Hilton which serves as the standard review and touchstone for TES physics and applications. Further, the work of Jan-Dreyling Eschweiler [69] is followed as well for a similar setup[1], allowing for more brevity here.
Other models which describe the TES resistance and associated sensitivites are discussed and compared in the review by Ullom and Bennett [66] as well, but will not be discussed here for the operation of this module. These models can serve as extensions and to understand better the TES physics, though the underlying formalism of [67] is still used. The readout of the detector with Superconducting QUantum Interference Devices (SQUIDs) will also be described, insofar as it pertains to the system employed in the TES detector setup. This follows Clarke and Braginski [70] (and [69]).

2.1 Introduction

The two main components of the TES setup, namely the detector itself and its read out system are based on the properties of superconductivity. The Bardeen-Cooper-Schrieffer (BCS) theory [71] describes this phenomenon, where a non-dissipative electric current is present in some materials below a critical temperature T_C. This current is comprised of electron pairs; these are called Cooper pairs and have electrons with antiparallel momenta and spins. These can overall be described with a single wavefunction and follow Bose-Einstein statistics, acting as composite bosons. The transition to this behaviour in many materials is very sharp, occurring over very short temperature scales. Within these

[1] A predecessor to the current setup and is no longer in use.

transition temperatures, the material can exhibit properties both superconducting and normal (Ohmic) conducting (with some macroscopic normal conducting resistance), but does not follow Ohm's law expressly. It is this transition region which is employed in the design and use of transition edge sensors. More details of superconductivity are given in many reviews and texts [72, 73]. Furthermore, it is at these low temperatures that thermal noise is suppressed and detections with greater precision can be made.

The superconductors have a critical supercurrent density j_c for a current flowing through them. This corresponds to the kinetic energy of the Cooper pairs and an increase in the current density beyond j_c can cause the Cooper pairs to break as it exceeds their binding energy. In order to bias the transition edge sensors to their working points within the transition regions, a predetermined current is used to take advantage of this feature.
This is different to the mechanism of Cooper pairs breaking due to the photoelectric absorption of signal photons, which are dominated by the production of quasiparticles and dividing energies between the electrons and phonons in the superconductor [74, 75]. The presence of other magnetic fields in the vicinity of the superconductor carrying a current close to its j_c can also cause the superconductor to transition into its normal conducting phases due to the induction of additional current in it (Meissner-Ochsenfeld effect [76]) to expel the fields. These are also a source of background signals in the TES, which will be discussed in Section 4.2, and require the shielding of the superconductor from external magnetic fields.

2.2 Single Photon Detection with a TES

The TES is a cryogenic microcalorimeter, exploiting the drastic dependence of the resistance of superconducting chip near its transition temperature T_C. Considering a classical calorimeter with some thermal capacitance C, the increase in temperature ΔT upon absorbing some energy ΔE is given by $\Delta T = \Delta E/C$. The temperature $T(t)$ exponentially decreases with a decay time constant τ, with its coupling to a thermal bath with a thermal link facilitated by the conductance G:

$$T(t) \sim \exp(-t/\tau),\ \tau = \frac{C}{G}. \tag{2.1}$$

The operation of the TES in its transition region uses this sensitivity to incident photon pulses, making it one of the most sensitive photon detectors [77]. Using this macroscopic change in the TES's resistance R_{TES}, the TES is in turn operated as a sensitive thermometer. This is expressed by the temperature sensitivity of the TES, α (evaluated for a working point (R_0, T_0)):

$$\alpha = \left.\frac{\partial \log(R)}{\partial \log(T)}\right|_0 = \frac{T_0}{R_0}\frac{\partial R}{\partial T}. \tag{2.2}$$

It must be ensured then, that this working point of the TES is within its transition edge[2]. The transition width can be very narrow; typically for low-T_C superconductors this is 0.1 - 1 mK. Just using the bath temperature T_{bath} to set the TES temperature is difficult, it is regulated better by sending in an operational or biasing current for an appropriate $T_{bath} < T_C$. This tunable current can then help break Cooper pairs to achieve a mixed state in the TES of normal and superconducting regions, within its transition edge. This also gives us the current sensitivity of the TES, β (evaluated for a working point as well):

$$\beta = \left.\frac{\partial \log(R)}{\partial \log(I)}\right|_{T_0} = \left.\frac{I_0}{R_0}\frac{\partial R}{\partial I}\right|_{T_0}. \tag{2.3}$$

This describes the temperature and current dependence of the TES resistance $R_{TES}(I, T)$, and allows the setup of a feedback mechanism, in contrast to a classical calorimeter.

The absorption of a photon causes the temperature and the resistance to increase. For a TES held at a constant biasing voltage V_{BIAS} this would in turn lower the corresponding

[2]This amounts to ensuring the resistance of the TES, R_{TES} at the working point corresponds to a temperature within the transition region/width.; this is how it is realized in this setup.

Joule heating to the TES, and the coupling to the cold bath allows the TES to cool back down to its equilibrium state.
The use of a constant voltage to bias the TES allows this negative electro-thermal feedback (ETF). Were a constant biasing current used, the Joule power upon resistance increase would also increase. This would correspondingly be a positive ETF. A negative ETF is more desirable as it does not lead to potential thermal runaways, results in a faster signal times but may not ensure a better signal-to-noise ratio.
The load resistance $R_L = R_{SH} + R_{PAR}$ dictates the biasing conditions, for a TES with working point resistance R_0 (R_{SH} is the shunt resistance, and R_{PAR} is the parasitic resistance):

- For strong negative ETF: $R_L << R_0$ (amounts to strong voltage-biased TES)
- For strong positive ETF: $R_L >> R_0$ (amounts to strong current-biased TES)

TES: Electrical and Thermal response

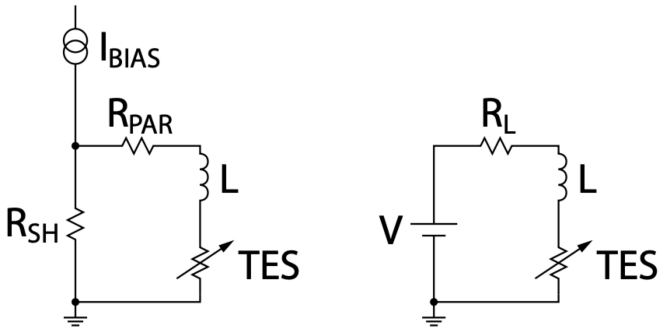

Fig. 2.1.: The circuit diagram for TES biasing with some input I_{BIAS}, from [67]. The diagram on the left is the Thevenin equivalent circuit, with $R_L = R_{SH} + R_{PAR}$, where R_{SH} is the shunt resistance and R_{PAR} is the parasitic resistance coming from any non-superconducting components in the circuit. This is where the strong negative ETF plays out: $R_L << R_0$, maintaining the biasing voltage $V_{BIAS} = I_{BIAS}R_{SH}$ across the TES.

In order to describe the TES response in the small signal limit, for an incident delta-function energy impulse (keeping in mind calorimetry) as a power load, we have to consider the electrical and thermal systems that the TES is coupled to[3]. These can be separated into the two aforementioned systems: the electrical (which biases the TES to a chosen operational stage) and the thermal (which cools back down the TES to its

[3]The response is in the bias line of the TES circuitry.

operational stage).
The thermal system is expressed by considering all the different powers influencing the TES: the power flow to the cryogenic bath P_{bath} includes the time-varying power P_{TES} across the TES, the Joule heating P_{Joule} of the TES, as well as arbitrary power inputs P like noise or signals:

$$P_{TES} = -P_{bath} + P_{Joule}(R(T,I)) + P \tag{2.4}$$

$$\implies C\frac{dT}{dt} = -P_{bath} + P_{Joule}(R(T,I)) + P \tag{2.5}$$

The electrical system is expressed by considering all the voltages along the TES circuit, as shown in Figure 2.1. These are obtained by using Kirchhoff's law of voltages across the entire TES circuit. The biasing voltage V_{BIAS} is then the sum of the voltages V_{Load} across the load resistance R_L, V_{TES} across the TES, and V_{ind} across the inductor (which varies with time). This is given by:

$$V_{BIAS} = V_{Load} + V_{Inductor} + V_{TES} \tag{2.6}$$

$$\implies L\frac{dI}{dt} = V_{BIAS} - IR_{Load} - IR(T,I) \tag{2.7}$$

The coupled differential equations in Eq.s (2.5), (2.7) are solved by assuming the small signal limit around the working point of the TES.
A small deviation from the steady state (i.e. the working point, as in Figure 2.2a) is assumed, denoted by δ: $R_0 \to R_0 + \delta R$ and $T_0 \to T_0 + \delta T$. This results in the linearization of several parameters like the resistance of the TES $R_{TES}(T,I)\,(\equiv R(T,I))$:

$$R_{TES}(T,I) \approx R_0 + \alpha\frac{R_0}{T_0}\delta T + \beta\frac{R_0}{I_0}\delta I\ , \tag{2.8}$$

where R_0 and T_0 denote the values of the parameter at the chosen working point, α and β are the temperature and current sensitivities of the TES, from Eq.s (2.2) and (2.3). The Joule power of the TES, P_J, (with steady state power $P_{J_0} = I_0^2 R_0(T_0, I_0)$) is given by:

$$P_J = I^2 R(T,I) \approx P_{J_0} + 2I_0R_0\delta I + \alpha\frac{P_{J_0}}{T_0}\delta T + \beta\frac{P_{J_0}}{I_0}\delta I, \tag{2.9}$$

after expanding it as well around the working point. The power flow to the thermal bath P_{bath} is given by (using the definition of the thermal conductance G; $G \equiv \frac{dP_{bath}}{dT}$):

$$P_{bath} = \frac{G}{nT^{n-1}}(T^n - T_{bath}^n), \tag{2.10}$$

where n is the coupling of the sensor to the thermal bath. Linearizing this gives:

$$P_{bath} \approx P_{bath_0} + G\delta T. \tag{2.11}$$

The resulting linearized DEs (from Eq.s (2.5), (2.7)) are:

$$\frac{d\delta T}{dt} = \frac{I_0 R_0(2+\beta)}{C}\delta I + \frac{1}{\tau_I}\delta T + \frac{\delta P}{C} \tag{2.12}$$

$$\frac{d\delta I}{dt} = -\frac{1}{\tau_{el}}\delta I - \frac{\mathcal{L}_I G}{I_0 L}\delta T + \frac{\delta V}{L}\ , \tag{2.13}$$

where:

- The low-frequency feedback loop gain under constant current is

$$\mathcal{L}_I \equiv \frac{P_{J_0}\alpha}{GT_0}, \tag{2.14}$$

  which for very strong negative ETF is $\mathcal{L}_I >> 1, \beta$.

- The current biased thermal time constant is

$$\tau_I = \frac{\tau}{1-\mathcal{L}_I}. \tag{2.15}$$

  $\mathcal{L}_I > 1$ would result in a negative time constant and further the instability due to thermal runaways.

- Th electrical time constant is

$$\tau_{el} = \frac{L}{R_L + R_0(1+\beta)}. \tag{2.16}$$

A homogenous solution, which has $\delta P = 0$ and $\delta V = 0$, can be found for the differential equations. The signal is represented by an impulse of energy which is instantly thermalized, expressed by the initial conditions $\delta T(0) = \Delta T = \Delta E/C$ and $\delta I(0) = 0$. With the homogenous solution, and following also Lindeman [78] as in [67], this results in (for $t > 0$):

$$\delta T(t) = \left(\left(\frac{1}{\tau_I} - \frac{1}{\tau_-}\right)e^{-t/\tau_+} - \left(\frac{1}{\tau_I} - \frac{1}{\tau_+}\right)e^{-t/\tau_-}\right)\frac{\Delta T}{(1/\tau_+ - 1/\tau_-)} \tag{2.17}$$

$$\delta I(t) = \left(\frac{\tau_I}{\tau_+} - 1\right)\left(\frac{\tau_I}{\tau_-} - 1\right)\frac{C\Delta T}{(2+\beta)I_0 R_0 \tau_I^2}\frac{\left(e^{-t/\tau_+} - e^{-t/\tau_-}\right)}{(1/\tau_+ - 1/\tau_-)}, \tag{2.18}$$

where τ_-, τ_+ are the fall and rise time of the pulse respectively. These are the inverse eigenvalues obtained by the diagonalization of the coupled system, and are given by:

$$\frac{1}{\tau_\pm} = \frac{1}{2\tau_{el}} + \frac{1}{2\tau_I} \pm \frac{1}{2}\sqrt{\left(\frac{1}{\tau_{el}} - \frac{1}{\tau_I}\right)^2 - 4\frac{R_0}{L}\frac{\mathcal{L}_I(2+\beta)}{\tau}}. \tag{2.19}$$

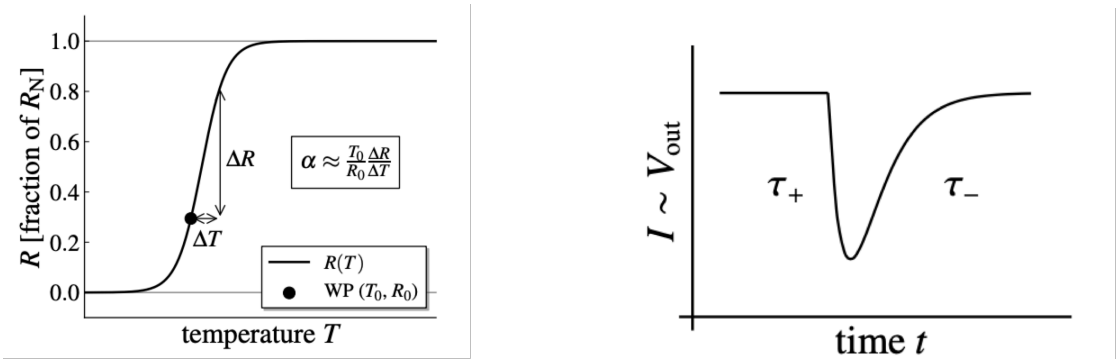

(a) (b)

Fig. 2.2.: The transition of the TES from its superconducting stage with resistance $R = 0$ at temperatures below critical temperature T_C to higher temperatures is illustrated in (a). With increasing temperatures, the sharp increase in the resistance (in a mixed state) for temperatures very close to T_C is shown, after which the normal conducting behaviour of the TES takes over, with resistance R_N. This transition width depends on many factors including the geometry of the TES, its internal properties, etc. [79]. These widths are typically < 1 mK. (b) shows the generic behaviour of a TES pulse in response to the incidence and absorption of a photon, with the rise and fall times described by Eq.s (2.19), (2.20). The TES heats up with photon absorption, the higher resistance causes a reduction in the current flowing through it. The ETF mechanism then allows the system to relax to its equilibrium state, i.e. as dictated by its working point and biasing. Figures from [69].

For small inductance L and with $\tau_+ << \tau_-$, these are further simplified to:

$$\tau_+ \to \tau_{el} = \frac{L}{R_L + R_0(1+\beta)} \tag{2.20}$$

$$\tau_- \to \tau_{eff} \equiv \tau \frac{1+\beta+R_L/R_0}{1+\beta+R_L/R_0+(1-R_L/R_0)\mathcal{L}_I}. \tag{2.21}$$

These form the pulse in the TES, shown in Figure 2.2b. For $T_{bath} < T_0$, we can approximate $P_{bath_0} \approx GT_0/n$, which results in the ETF time constant:

$$\tau_{eff} \to \tau_{ETF} = \frac{\tau}{1+\alpha/n}. \tag{2.22}$$

The current response Eq. (2.18) of the TES corresponds thus to the energy absorbed while the TES is operated with the ETF mechanism, and the time integral over it describes the so-called ETF energy:

$$E_{ETF} = -\int_0^\infty V_{TES}\delta I(t)dt \approx -I_{BIAS}R_{SH}\int_0^\infty \delta I(t)dt. \tag{2.23}$$

The fundamental noise in the TES comes from two main sources, which influence the baseline energy resolution. These are[4]:

- the Johnson-Nyquist noise due to the thermodynamic fluctuations in the electrical components such as the resistances R_L and R_{SH} along with the TES resistance R_{TES}, and
- the thermal fluctuation noise (TFN) due to thermodynamic fluctuations in components with thermal impedance, such as G.

The solution for the TES response can also be solved for a small, sinusoidal power load $\delta P = \mathrm{Re}(\delta P_0 \exp(\iota\omega t))$. As elaborated in [67], this particular solution can be found also including the inhomogeneous terms and adding in the homogenous solution. This further helps in describing the noise in the TES. The fundamental energy resolution in the TES is limited by this noise. Without outlining the analytical description, this energy resolution is presented here, for Gaussian noise sources and strong negative ETF [67]:

$$\Delta E_{RMS} = \sqrt{\frac{4k_B T_0^2 C}{\alpha}\sqrt{\frac{n(1+2\beta)}{1-(T_{bath}/T)^n}}} \tag{2.24}$$

2.3 SQUID Readout

Superconducting Quantum Interference Devices (SQUIDs) are essentially cryogenic magnetic flux sensors, combining the dual effects of the magnetic flux quantisation and quantum tunnelling. As low noise sensors, their widespread applicability has been well documented and motivated ([80, 81, 82]) for detectors with slow to ultra-fast signal rates. Predicted first by London [83], flux quantisation was observed by others ([84, 85]) by 1961, showing that flux in a superconducting loop is always quantised in units of the flux quantum $\Phi_0 = h/2e \approx 2.07 \cdot 10^{-15}$ Wb. This section follows the SQUID theory from

[4]Assuming no underlying hidden state variables in the TES (such as noise due to poor heat capacity coupling) and noise due to quantum fluctuations. These can comprise sources of excess noise.

[70] and further laid out in [69].
The prediction of the tunnelling of Cooper pairs through an insulating barrier separating superconductors was made by Josephson [86], stating that the current through this 'junction' is given by:

$$I = I_0 \sin \delta, \tag{2.25}$$

where δ is the difference in the phases ϕ_i in the condensates in the superconductors, and I_0 is the critical current. For a voltage U across the superconducting electrodes, the phase δ evolves with time:

$$\frac{d\delta}{dt} = \frac{2eU}{\hbar} = \frac{2\pi U}{\Phi_0}. \tag{2.26}$$

The current-voltage characteristics of the Josephson junctions are obtained by using the Resistively- and Capacitively-Shunted Junction (RCSJ) model (Figure 2.3a). This describes the junction as a Josephson element with some critical current I_0 connected in parallel to its self-capacitance and a resistance. In the dynamic range, the current through the junction consists not just of Cooper pairs but also of currents due to quasiparticles (I_{qp}) and electron-hole displacements (I_d). These currents can be complex and for practical uses are approximated by the ohmic shunt resistor and capacitor respectively. Other models which avoid the use of the linear resistance R, like the nonlinear resistive junction (RSJN) model or tunnel junction microscopic (TJN) model [87], are not used or discussed here.
In the dynamic range, the current oscillates with the Josephson frequency $w_J = 2\pi V/\Phi_0$ [5]. The construction of SQUIDs entails using a Josephson junction in a closed superconducting loop. A dc SQUID, such as the one described in this work and used to read out the TES, features two symmetric Josephson junctions connected in parallel to each other. A SQUID with a single such junction is called an rf SQUID and can be used as well, but is not optimal for use at frequencies other than microwave frequencies, and has higher intrinsic noise. To eliminate hysteresis on the $I - V$ characteristic of SQUIDs, the operational setups for dc SQUIDs feature a resistive shunt as well. The parallel junction structure of the dc SQUID then dictates the maximum current flowing through the SQUID, and the presence of any external magnetic flux causes fluctuations in the current. This is the effective working principle of the SQUIDs (as magnetometers) and is called the SQUID

[5] Or $f_J = 2\pi/w_J \approx V \times 438.6\,\text{MHz}/\mu\text{V}$.

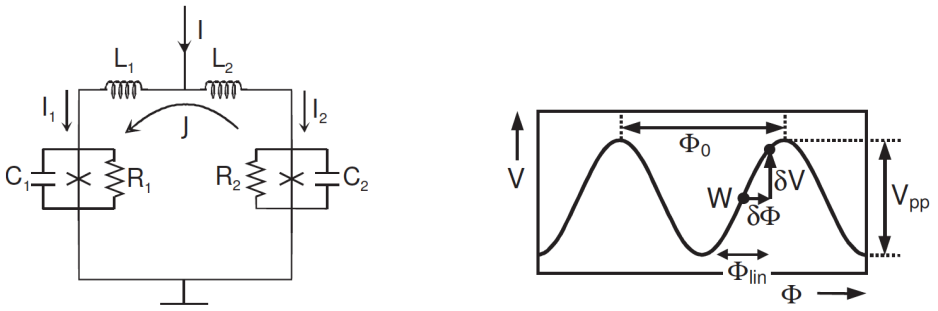

(a) (b)

Fig. 2.3.: (a) shows the equivalent circuit for a SQUID with the Josephson junctions described using the RCSJ model, with a resistance R and capacitance C in parallel with superconducting Josephson element in each junction. A Josephson junction is depicted by the cross in a circuit, otherwise. The junctions are connected in parallel to each other with the currents I_i flowing through them. The external flux is coupled into this system via the inductance of this equivalent circuit $L = L_1 + L_2$. The junctions may in some cases be symmetrical but this may not be desirable in all cases (pertaining also to discrepancies with respect to fabrication). The corresponding $V - \Phi$ characteristic is shown in (b), with a Φ_0-periodicity, and a non-unique working point W. In the linear regime Φ_{lin} with a peak-to-peak voltage $V_{pp} \equiv V(\Phi_a = \Phi_0/2) - V(\Phi_a = 0)$. In practice, the $V - \Phi$ characteristic, though periodic, is not perfectly sinusoidal. The sinusoidal $V - \Phi$-characteristic is linear around the working point only for small values of $\delta\Phi$, $\Phi_{\text{lin}} = V_{pp}/|V_\Phi| \lesssim \Phi_0/\pi$. Figures adapted from [70].

modulation. The voltage measured in the SQUID due to the influence of some magnetic flux Φ_a experienced by it is given by V:

$$V = \frac{R}{2}\sqrt{I_b^2 - I_c^2}, \tag{2.27}$$

where V is the time averaged voltage, and the current I_c is the maximal current possible in the SQUID while I_b is the bias current. For an average bias current I_0 through *both* the junctions, I_c is:

$$I_c = 2I_0\left|\cos\left(\pi\frac{\Phi_a}{\Phi_0}\right)\right|, \tag{2.28}$$

giving the voltage characteristic [6]:

$$V = \frac{R}{2}\sqrt{I_b^2 - \left(2I_0\cos\left(\pi\frac{\Phi_a}{\Phi_0}\right)\right)^2}. \tag{2.29}$$

[6] For with $I_b > I_c$ and the Stewart-McCumber parameter $\beta_C \equiv \frac{2\pi}{\Phi_0 I_0 R^2 C} << 1$.

The Φ_0-periodicity of the voltage is shown in Figure 2.3b. The change in V due to the voltage applied Φ_a is given by $\partial V/\partial \Phi_a$, which usually diverges for $I_b = I_c$ but it is finite in practice due to thermal fluctuations. This is used to define the SQUID characteristic function curve:

$$V_\Phi \equiv \max\left(\left|\frac{\partial V}{\partial \Phi_a}\right|\right). \tag{2.30}$$

The working point of the SQUIDs is decided by the V-Φ characteristic, where the steepest and linear section is chosen as the working point. This is done by the application of some flux. Due to the Φ-periodicity the working point is non-unique. The change in the voltage measured due to the sensing of other flux is then given by the characteristic function curve V_Φ at this working point, making the SQUIDs relative magnetic flux sensors.
The SQUIDs with identical junctions, however, are not necessarily the best SQUIDs. In some cases they may be preferred, but taking into account imperfections and fluctuations the SQUIDs with the screening parameter $\beta_L \equiv \frac{2LI_0}{\Phi_0} \approx 1$ are preferred.

TES Readout

The flux sensing properties of the SQUID enable its use as a very sensitive ammeter or voltmeter. This is done by coupling the SQUIDs to the TES detector inductively, and have the consequent output amplified and used to linearise the SQUID response. The input circuit is the TES with its input coil, as shown in Figure 2.4, with the inductive coupling to the sensing SQUID given by the inverse mutual inductance:

$$M_{\text{in}}^{-1} \equiv \frac{\delta I_{TES}}{\delta \Phi_{\text{in}}}. \tag{2.31}$$

This voltage detected is typically $\mathcal{O}(10)\,\mu$V, necessitating consequent amplification. The M_{in}^{-1} depends on the circuitry and the physical distances between the sensor and the input coil/circuit. The use of the SQUIDs is enhanced by linearising the transfer coefficient, achieved by using a feedback circuit coupled inductively again to the primary sensor SQUID with the mutual (feedback) inductance M_f^{-1}:

$$M_f^{-1} \equiv \frac{\delta I_f}{\delta \Phi_f}. \tag{2.32}$$

This feedback circuit features a feedback resistance R_f with values in kΩ. The looped negative feedback sent to the SQUID linearises its response and increases its dynamic range. This mode to read out the TES current I_{TES} is called the FLL mode (flux-locked loop) mode and is used for all DAQ purposes. The operation of the SQUIDs without the FLL, i.e. using the amplification properties of the circuit only is called the AMP mode. This is important to locate the SQUID working point from its (amplified) characteristic[7]. The operation of the SQUIDs in this fashion yields the I_{TES} as an output voltage V_{out}.

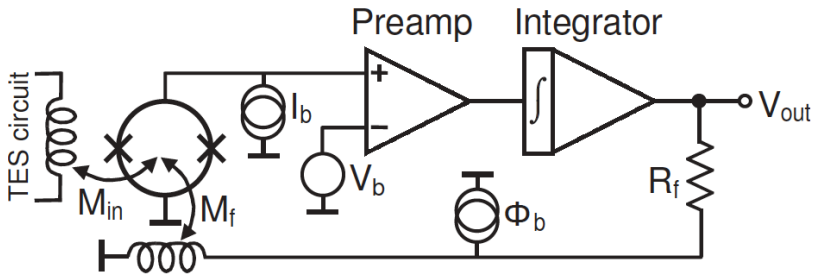

Fig. 2.4.: The layout of a dc SQUID sensor and the input TES circuit is shown above. The primary SQUID is coupled to the input coil inductively via M_{in}, and the output from this is fed back to it again after it is preamplified and integrated; via the inductive coupling M_f. This negative feedback loop is the backbone of the utility of the SQUIDs as highly sensitive ammeters/voltmeters using the FLL mode.

The SQUID has to be set at its working point first, before it can sense any input. The bias current I_X regulates the initial modulation, and a flux source (realised as a current) Φ_X is also used to achieve the working point. The amplification is done, for our system, by a series of SQUIDs which act essentially as just one SQUID and can be treated as such. These are set in their working point also using a current source I_b, voltage V_b and flux input (creating additional shifts) Φ_b.
For a small TES current change δI_{TES}, a small flux $\delta\Phi$ is sensed in the primary SQUID which is preamplified and fed back (negatively). With this FLL mode operation active, we have:

$$\delta V_{out} = R_f \delta I_f. \tag{2.33}$$

[7]Further details regarding the SQUID setup are described in [69].

The negative feed back cancels the initial signal, so $\delta\Phi_f$ corresponds to $\delta\Phi$. This gives the relation:

$$\delta\Phi_f \equiv \delta\Phi = \frac{\delta V_{out}}{R_f M_f^{-1}} \,. \tag{2.34}$$

This, with Eq. (2.31) gives the current-voltage relation:

$$\delta I_{TES} = \delta V_{out} \frac{M_{\text{in}}^{-1}}{R_f M_f^{-1}} \tag{2.35}$$

The proximity of the SQUIDs to the TES has also been noted to have unexpected heating effects on the TES itself, where the use of optimal values for the SQUID working point can drive the TES out of its working region (i.e. out of its transition region). The use of low power SQUID sensors hopes to mitigate this issue but has yet to be employed. With the two-stage SQUIDs readout, the TES signal can be detected. The choice of the working points of the SQUID system, along with other settings, such as the choice of a gain-bandwidth product and R_f can be made using the electronics used to run the SQUIDs.

2.4 Detector Module

2.4.1 Transition Edge Sensors

TESs encompass a large variety of detectors in forms and uses, over a wide energy scale, which can differ in their implementations and use from experiment to experiment. They have also found widespread use especially in the detection of photons and other particles, in addition to the considerable interest in quantum optics applications [88]. This is evidenced by the many materials and designs used for the fabrication of TESs for photon detection over energy ranges such as keV, as in [89] with Mo/Cu TESs and for 0.8 eV with W TESs in [90]. Arrangements of sequenced TES arrays i.e. multiple TESs, such as those in [91], with arrays of Ti/Au TESs, can also be used. These may also be of interest in budding searches for dark matter using TESs.

The design of the TESs as microcalorimeters or bolometers depends on the photon energy under investigation, with energies above 10 keV typically requiring the use of a separate

absorber which the TES is coupled to and which is read out. For energies on the eV-scale, the absorber and the TES chip can be one and the same as they have adequate stopping potential. The response of the TESs has been discussed in Section 2.2, and further developments have been made in understanding the underlying physical mechanics of the TES using models like the resistively-shunted junction 'RSJ' model (described more in [66] and [92]), which mimics the RCSJ approach used to model Josephson junctions (Section 2.3). These models may help to understand further sources of noise seen in TES systems, but have yet to be investigated and is not in the scope of this work, the noise has a considerable effect on dark counts and background events nonetheless.

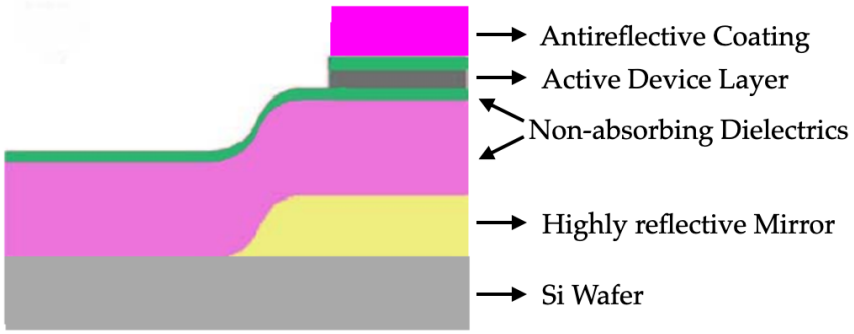

Fig. 2.5.: The cross sectional view of the design of a TES stack, with the various layers tuned to achieve a high absorption of photons incident on the TES. The anti-reflective coating atop the stack and highly-reflective mirror at its bottom increase the absorption in the active layer significantly. The schematic also shows the relative size and dimensions of this active absorbing layer for photons, which is a W microchip for the TES used in this work. There are numerous other structures used for the detection of (typically keV) photons which feature TES bilayers, interdigitated films, etc. and are mentioned in [66]. Figure and details from [93].

Abstaining from further details regarding TES detectors and their makeup, the design and construction of the TES chip used in this work and for the ALPS II experiment is described. TESs, as single photon detectors with high energy resolution and low noise, are embedded in an optical stack (multilayer structure) which strongly increases their detection efficiency, as depicted in Figure 2.5. The application of the optical stack increases the absorption efficiency from ∼20% (for a bare tungsten TES) to ∼99%. The TES used is from NIST[8], USA and has been designed and manufactured for optimal absorption of 1064 nm signal photons by tuning the thicknesses of the constituent layers in the stack. The simulation of these layers to photon absorption is carried out taking into account their refractive indices, transmission, and other properties. As these devices

[8]National Institute of Standards and Technology

are operated at $\mathcal{O}(100)$ mK temperatures, the thermal properties of the materials are also investigated for compatibility. The stresses that can arise from different thermal coefficients are allayed by the use of the (a Si)-W-(a Si) (amorphous silicon) trilayer [94]. Other materials for the active layer (such as Hafnium (Hf)) do not require this stress-relieving layer in the multilayer structure.

W TES Chip

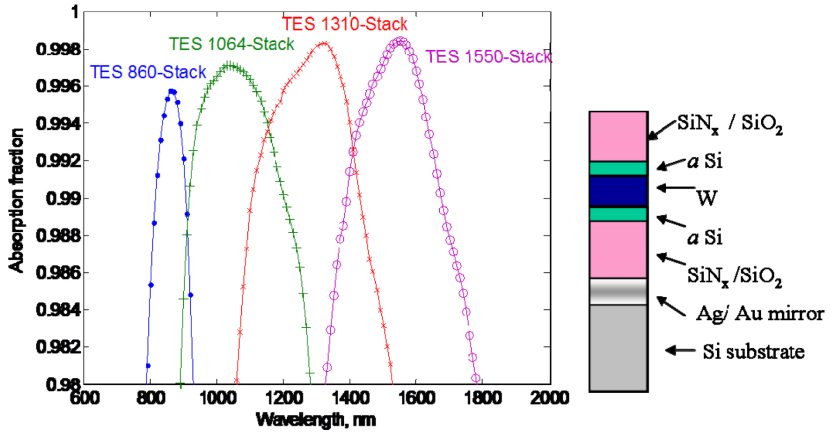

Fig. 2.6.: A generic TES stack is shown (on the right) with the multilayer structure for TESs designed for near-IR photon detection, by tuning the various thicknesses of the layers. These are optimised for 860, 1064, 1310 and 1550 nm photon absorptions, as shown in the plot, from [93]. The TES stack for 1064 nm is pertinent to this work.

The TES chips used are designed and manufactured by NIST[9], and use tungsten as their active absorbing layer. The application of such W TESs is investigated for the absorption of near-IR photons in a similar optical multilayer, shown in Figure 2.6. Tungsten exhibits distinct electron-phonon decoupling [95] at low temperatures, with the electron and phonon system being at different temperatures. This essentially facilitates the use of the electron system as the 'absorber' in the W chip and the phonon system provides the requisite weak link to the bath. In this way, the W microchip is both absorber and sensor in one. The thermal properties of the chip depend on the temperature. The link to the cold bath must provide adequate cooling power such that the TES becomes superconducting and must also be lower than the transition temperature such that the TES can be reliably operated within this temperature region.

[9]National Institute of Standards and Technology, USA

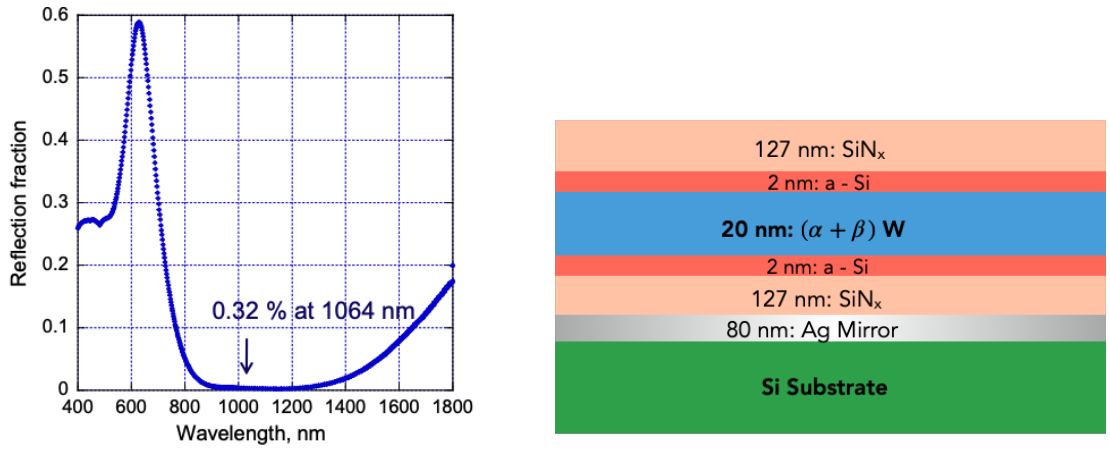

(a) (b)

Fig. 2.7.: The detailed view of the optical multilayers in the TES stack optimised for 1064 nm photon detection. The TES is the $25 \times 25\,\mu$m W microchip with a thickness of 20 nm. The layers allude to the ones described in Figure 2.6, and are all deposited on a-Si substrate ~375 μm thick. The W microchip is tuned to achieve its T_C using the α and β structures of W. The SiN_x layers which improve the anti-reflective properties and the a Si stress-relieving layers are shown as well, with the reflective Ag mirror on the bottom of the stack.

Tungsten's α and β structures are used to tune the critical temperature for the TES. The bcc-lattice α structure exhibits a critical temperature ~15 mK, and the β structure[10] can exhibit $T_C \sim 1 - 4$ K. The use of both in specific ratio can achieve $T_C \approx 50 - 200$ mK, which depends also on the sputtering system during the fabrication process. The large variability in the W TESs that can be used is also due to the T_C required in each case for the photon energy scale under investigation. The incidence of photons on the TES leads to the creation of photoelectrons in the TES, and due to the phonon decoupling, the gradual loss of heat is noted. Hot photoelectrons may escape the TES, and this leads to a loss in the final energy detected. The reflected energy from photon incidence can also be quite high, at about 25%, but the optical stack, Figure 2.7b, (optimised for a selected wavelength) can reduce this and result in near-unity quantum efficiencies.

2.4.2 SQUID Sensors

SQUID chips manufactured at PTB[11], Berlin are used to read out the single TESs. The readout scheme uses a primary or sensing SQUID (front-end), whose output is further

[10] A15 phase, featuring an intermetallic compound.
[11] Physikalisch-Technische Bundesanstalt

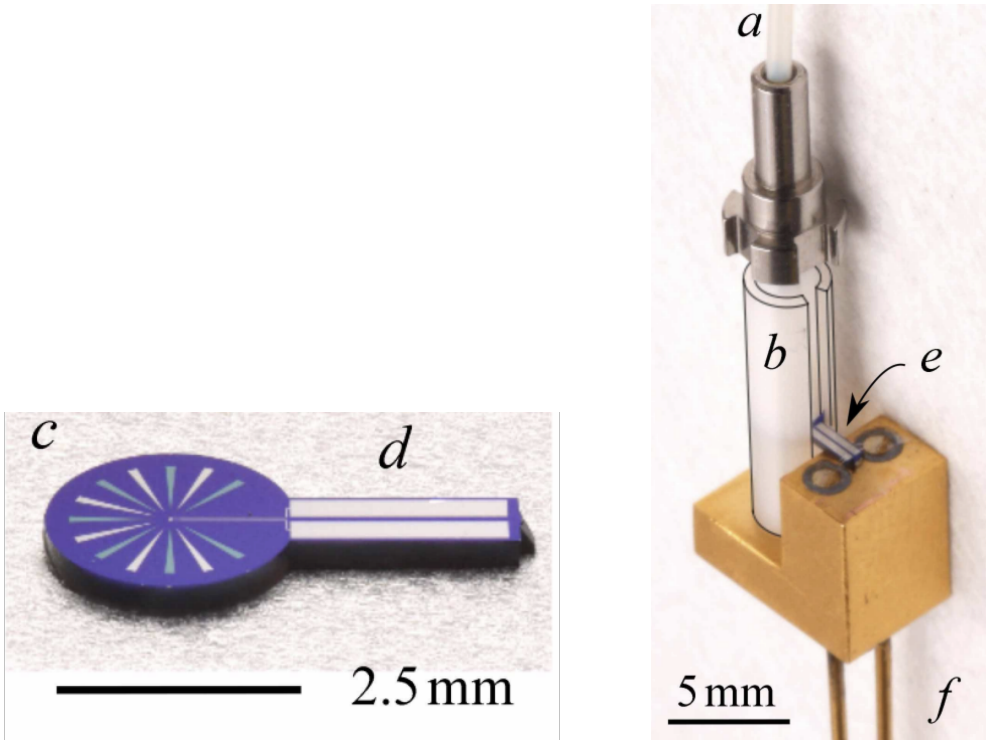

(a) (b)

Fig. 2.8.: (a) shows the NIST TES chip in the centre of the racket-shaped substrate with a diameter 2.5 mm. The white sections near the 'grip' are the aluminium pads to support the bond wires. (b) shows the fiber-to-sleeve coupling, with the fiber tip directly focusing the fiber output on the TES chip. This is an exemplary implementation, and is used sightly differently on the TES detector module. The fiber sleeve is made from zirconia and allows the damage-free assembly of the fiber tip. Figures from [96].

read out and amplified by a series of 14 single SQUIDs. This two-stage implementation is operated as a current sensor for the TES. The series of second-stage SQUIDs are operated as single SQUID (and amplifier) with current and voltage biasing I_b, V_b respectively and flux biasing Φ_b (for working point adjustment). The front-end SQUID is operated with the current and flux biasing I_X and Φ_X respectively. These values are set by using the SQUID electronics XXF-1, from Magnicon GmbH, to operate the sensors. The SQUID chips also incorporate the resistance shunt and input coil of the TES circuit. Each 2-stage SQUID readout is for a single TES chip, and they are designed and integrated on the detector module by PTB.

The power output of the SQUID chips is dominated by the second stage biasing, i.e. $I_b V_b$, a dissipation of $\mathcal{O}(10)$ nW. The use of the 2-stage setup reduces the contribution of electrical noise noise in the line, which is then dominated by only the front-end SQUID.

Module

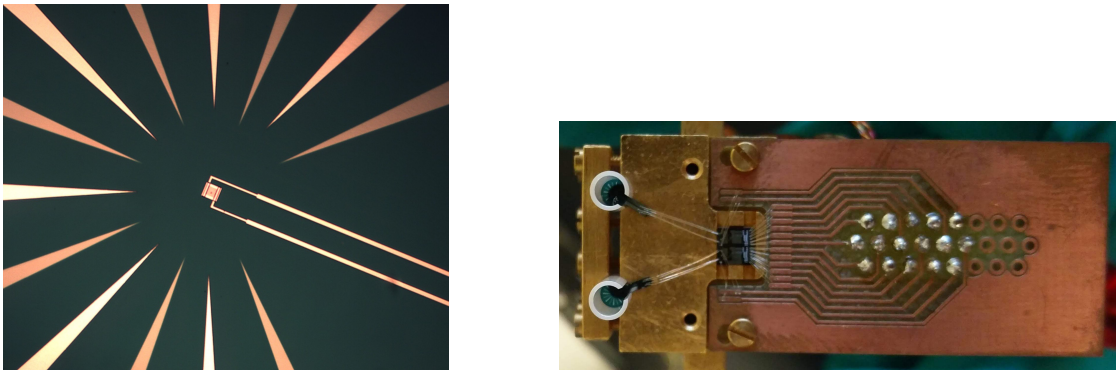

(a) (b)

Fig. 2.9.: A magnified view of the TES chip in Figure 2.8 is shown in (a), from [69]. (b) shows the detector module with the two NIST TESs, and the SQUID readout channels. The approximate size of the module is 1 cm×2 cm. The white zirconia ferrules (from Figure 2.8) around the TESs is connected by bond wires to the SQUIDs, seen between the two screws. The thermalisation of the full NIST TES chips (on the sapphire substrates) is realised via connection to the gold-plated copper it is attached to, with a silicon grease.

The TES detector module used for the experiment, with NIST TESs and PTB SQUIDs, is shown in Figure 2.9. A more detailed setup of this module and few other TES candidates looked into can be found in [69] and [97]. The operation of this module is carried out in the adequately cold environment of a cryostat, where it is mounted. These details are discussed next.

2.5 Cryogenic Environment

The operation of the detector module, with the TES and SQUID read out, requires adequate cooling to achieve stable superconducting behaviour. This is achieved by housing them in a cryogenic environment provided by a dilution refrigerator. The working and setup of the dilution refrigerator is discussed in Appendix A.

Here, the setup of the detector in this refrigerator is discussed, with respect to the optical fiber inputs and the connection to the SQUID electronics.

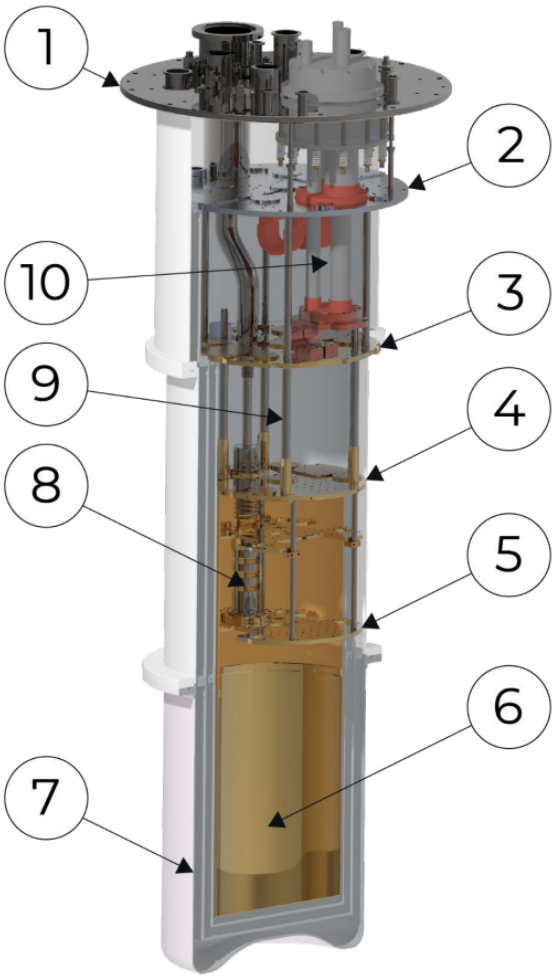

Fig. 2.10.: A cross-sectional view of the cryostat vacuum can is shown above. (1) is the room temperature flange, where additional components can be attached depending on what is required in the detector setup, such as optical fibers, and SQUID read out electronics. (2) and (3) are the 40 K and 4.2 K stages respectively, cooled by the pulse tube (10). Below this, the condensation of the He-mixture starts in the still chamber stage (4), with the dilution cycle as described in Figure A.2 in the dilution unit (8) cooling the mixing chamber stage (5). To this cold plate, at a temperature of ∼25 mK, the experimental setup (6) is attached. The heat switches (9) connect the stages thermally and provide support to the frame. Finally, this entire setup is housed within the vaccum can and with multiple radiation shields, for the various stages (7). Figure from BlueFors.

2.5.1 Detector Setup

In the experimental volume available in the cryostat, shown in Figure 2.10, the detector setup is installed. This is shown in Figure 2.11 and described below:

- The detector module (Figure 2.9) is mounted on a oxygen-free copper cold finger.

- This copper cold finger, which can be designed and manufactured depending on the orientation chosen for the detector module, is connected directly to the cold plate, i.e. under the mixing chamber stage. This helps in the modifications of the detector setup, discussed also in Section 4.3.3.
- The wiring from the SQUID chips are connected to LEMO 00 connectors at the mixing chamber stage with a Micro-D 25 pin connector which is attached directly on the detector module.
- The wires from the LEMO 00 connectors are further connected to the cryocable, feeding the SQUID electronics at the room temperature stage of the vacuum can. They are thermalised at every stage of the cryostat that they pass through.
- The input to the TES via optical fibers is done similarly, by sending them through fiber feed throughs atop the cryostat.
- The cold finger and detector module are further housed in an aluminium can connected to the mixing chamber stage. This acts as a superconducting electromagnetic shield and also provide light-tightness.

With the cryostat in normal circulation mode, and the base temperature achieved, the TES chip(s) in the detector module can be calibrated and tested for their response.

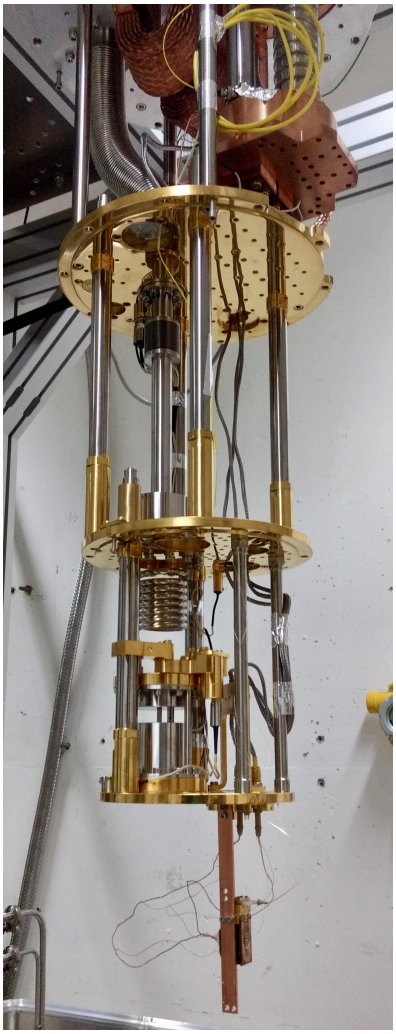

Fig. 2.11.: The opened up cryostat vacuum can is shown above, with the various stages exposed. The radiation shields and vacuum can are removed. The internal dilution unit is seen from the still chamber to the mixing chamber stage. Below this, the copper cold finger is attached to the cold plate and the module is mounted on it with a small copper attachment block, oriented sideways to face the inner 'walls' of the cryostat. The multiple sections in the cold finger provide appropriate portions for mounting the module differently, such as at the very end of the cold finger or in a different orientation entirely. The optical fiber (curled up, and protected by the yellow cladding) is connected to the module and inserted through an opening in the cold plate in the mixing chamber stage. The wiring connections from the Micro-D 25 pin connector (from the SQUID chips) are further connected to the LEMO 00 connectors.

2.6 TES Operation

The appropriate biasing of the TES is essential to use it as required. The response of the TES depends on its working point, realized in terms of its resistance R_{TES}. The strong voltage biasing method adopted in most modern single- and multi-TES systems, described in [98] and used widely since, is implemented. In order to do this, the I-V characteristic of the TES has to be scoped out in order to get the active R_{TES}. The biasing, seen in Figure 2.1, is varied with an external voltage generator and the general TES biasing from the SQUID electronics[12] is bypassed so as to use a time-varying input signal as in Figure 2.12a. The resulting I-V characteristic is shown in Figure 2.12b, where:

$$V_{TES} = I_{BIAS} R_{SH} = \frac{V_{input}}{R_{IBox}} R_{SH} \; (\equiv V_{BIAS}) \tag{2.36}$$

$$I_{TES} = V_{out} \cdot \xi = V_{out} \cdot \frac{M_{in}^{-1}}{M_f^{-1} R_f}. \tag{2.37}$$

The factor ξ is the current-to-voltage conversion factor from the SQUIDs, taking into account their mutual inductances with the TES circuit, following Eq. 2.35, and has the unit Ω^{-1}. From Figure 2.12b we see that:

- For $V_{TES} \lessapprox 0.15\,\mu$V the TES is predominantly superconducting.
- For $V_{TES} \gtrapprox 0.5\,\mu$V the TES is normal conducting with $R_{TES} = R_N$, its normal conducting resistance of $\sim$10 Ω.
- For $0.15\,\mu\text{V} \lessapprox V_{TES} \lessapprox 0.5\,\mu$V we have the TES existing in the mixed state, with normal and superconducting characteristics. The former becomes more pronounced as the input biasing increases. In this transition region, the R_{TES} is expressed best in fractions of the TES's normal conducting resistance R_N.

[12] This is done with the use of an I-Box, on loan from PTB, Berlin. The current sources to the TES from the SQUID electronics are circumvented and replaced by external ones across a resistance of R_{IBox} =20 kΩ. This will be replaced by a commercial one from Magnicon GmbH, with a resistance of R_{IBox} =10 kΩ.

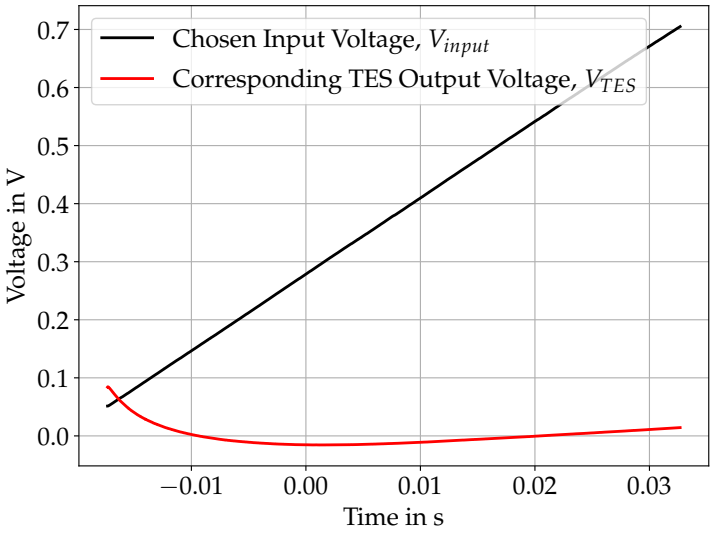

(a)

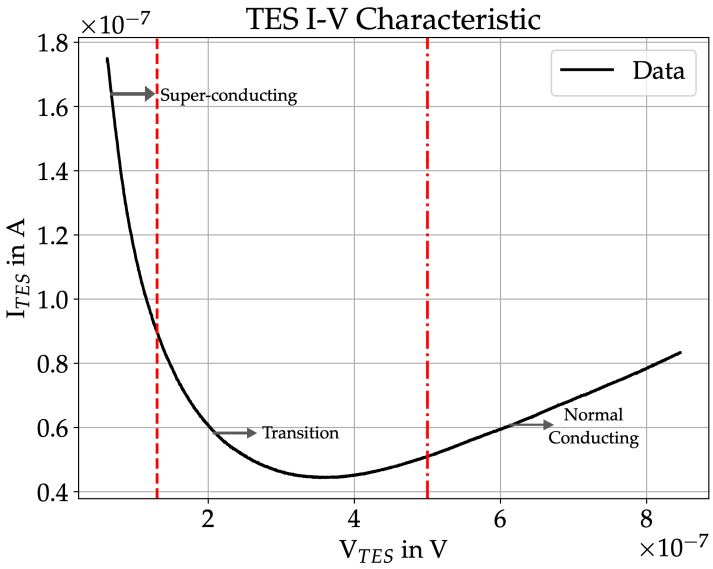

(b)

Fig. 2.12.: Figure 2.12a shows the input voltage V_{input} to the TES from an independent generator and the corresponding V_{output} from the TES over time. The V_{input} typically has a maximum peak-to-peak voltage of 800 mV, a DC offset of 50 mV and frequency of 10 Hz. A chosen 'increasing' arm of the V_{input} is used above, but a 'descending' one (and its corresponding V_{output}) can also be used, to achieve the same I-V characteristic in Figure 2.12b. These start to differ at input frequencies higher than 10 Hz. The I-V characteristic shows the changing current flowing through the TES for the increasing biasing voltages it is held at, and the changing conducting nature of the detector.

It is in this transition region that a working point for the TES can be found, such that the biasing voltage (or correspondingly, the I_{BIAS}) is chosen accordingly[13]. The working point must ensure that:

- The behaviour of the TES is linear around its working point, an essential assumption made to arrive at Eq.s(2.19), (2.17) which describe the TES response.
- A high dynamic range is maintained, such that incident photons may be properly triggered and distinguished
- A high energy resolution may be achieved for 1064 nm photons.

[13]It must be noted that these values depend not only on the input voltage or the V_{BIAS}, but also on the SQUID parameters. These are settings which bias the SQUID(s) for proper operation with respect to sensing and amplification.

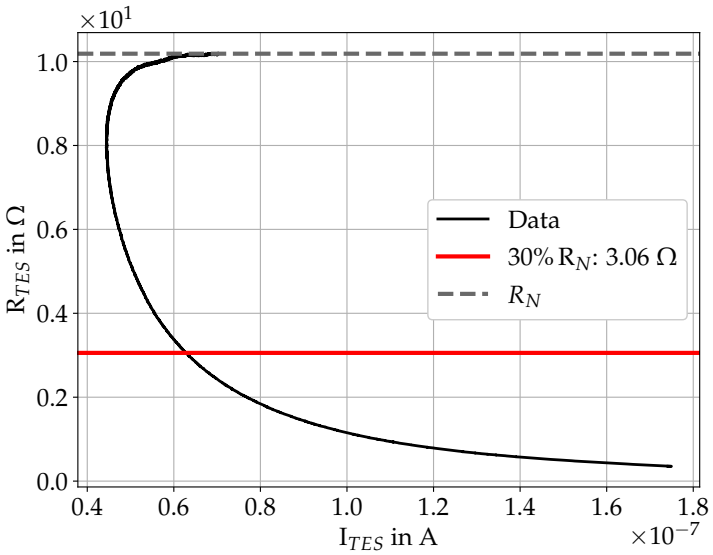

(a)

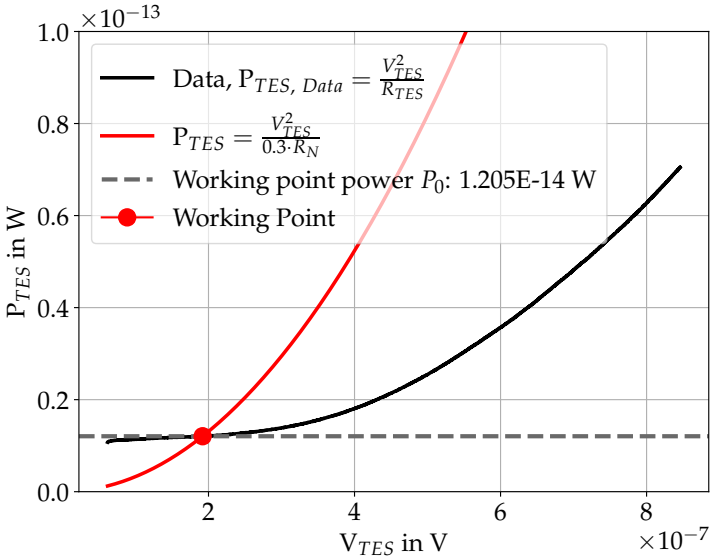

(b)

Fig. 2.13.: (a) illustrates the change in the R_{TES} as a function of the current flowing through the TES. In the vicinity of the working point, chosen to be $30\%R_N$ here, the current sensitivity β (from Eq. (2.3)) for the TES can be calculated. In (b) the power P_{TES} is shown as a function of the biasing, for both the data and for a TES set at $R_{TES} = 30\%R_N$. The intersection point of these curves gives the steady state power P_0 of the TES.

Keeping in mind these requirements, a working point of $30\%R_N$ (i.e. corresponding to a TES resistance $R_{TES} = 30\%R_N$) can be selected (Figure 2.14). To calculate the

Parameter	Value	Comment(s)
R_N	$10.18 \pm 0.1\,\Omega$	V_{TES}/I_{TES}, normal conducting region
$0.3R_N$	$3.06 \pm 0.03\,\Omega$	Exemplary working point, transition region
β	2.14 ± 0.013	Current sensitivity, from Eq. (2.3)
α	354.34 ± 1.39	Temperature sensitivity, from Eq. (2.2)
$I_{TES,WP}$	0.628 ± 0.01 nA	TES working point current, for $0.3R_N$
$P_{TES,\,WP} = P_0$	0.1205 ± 0.0108 fW	TES working point power, for $0.3R_N$
$\mathcal{L}_I$	70.86 ± 0.27	Loop Gain, from Eq. 2.14
τ_+	2.27 ± 0.01 ns	TES pulse, rise time constant, from Eq. 2.20
τ_-	$16.43 \pm 1.5\,\mu$s	TES pulse, decay time constant, from Eq. 2.20

Tab. 2.1.: The parameters of the TES at its working point are shown above, for a selected working point corresponding to $0.3R_N$. The errors shown are statistical in nature. The rise and decay time constants will be contrasted with measured TES pulses. The other TES parameters, such as the heat capacity and thermal conductance, etc. remain unchanged from previous iterations of this module and can be found in [69].

rise and decay times ($\tau_\pm$) of TES pulses at this working point and with the appropriate settings, the current and temperature sensitivities need to be known (Section 2.2). These are calculated from Figures 2.13a, 2.14 at the working point. The same is true for the working point power, obtained and shown in Figure 2.13b. These values are shown in Table 2.1 In order to distinguish better some background pulses arising from the incidence of 532 nm photons, a different working point may also be chosen. This is also true for any background(s) in general, the choice of a working point must also ensure that it triggers the least number of dark events or that the working point is indifferent to it. This will be investigated as well in following sections. Any changes in the TES's thermal

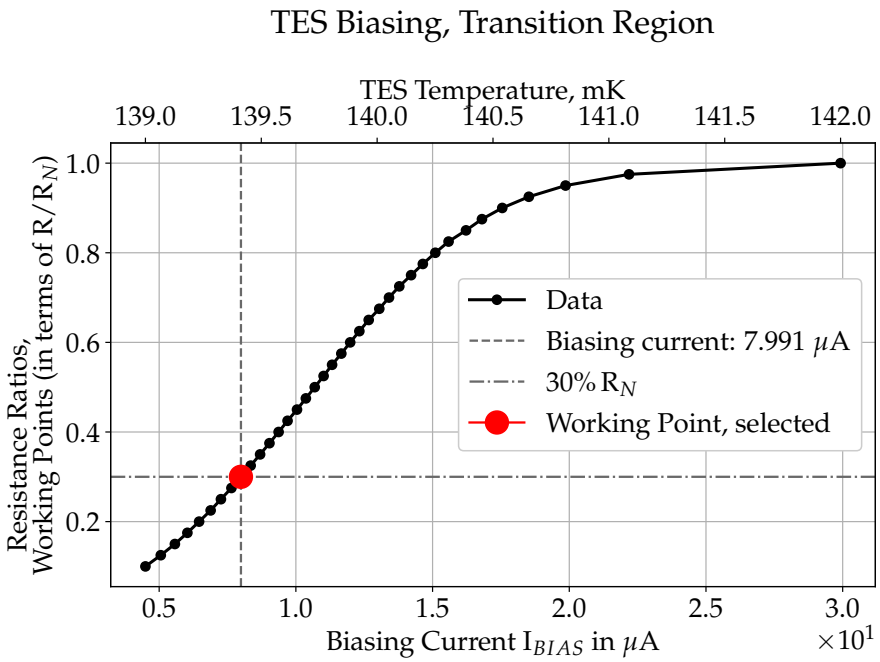

Fig. 2.14.: The transition region of the TES is shown above with possible working points, realized in terms of R_{TES}/R_N for increasing biasing currents I_{BIAS}. In order to operate the TES at a working point corresponding to, for instance, $30\%R_N$, a biasing current of 7.991 μA must be used. For currents $I_{BIAS} \geq 17.5\,\mu$A, the TES is almost completely normal conducting. In the vicinity of the working point in the above plot, the temperature sensitivity α (from (2.2)) can also be calculated. The temperature at the TES is not explicitly measured; the values mentioned are heuristic estimates.

environment (such as changes in the SQUID parameters, etc. or simply another cooldown of the dilution refrigerator or thermalization of wires in the TES setup) necessitates the re-characterisation of the TES in order to set it back at the chosen working point.

3 TES Pulses and Characterisation

The TES (with the setup described in Section 2.5.1) can be set to its specific working point and used to detect incident photons; signals and background alike. The choice of stable working settings also applies to the SQUIDs, and these (should) ideally remain unchanged through the data-taking process. This procedure is described in detail in [69] and the operation manual for the SQUIDs[1]. This section shortly describes the DAQ itself and the analysis of the acquired TES pulses, the various approaches used for the same and their features. Some results of this section are also mentioned in [8].

3.1 Data Acquisition and Processing

The SQUID output voltage is connected to the Alazar Card ATS9625 in the readout computer. With the AlazarGUI interface, the card can sample data at different frequencies for specified amounts of time (in seconds), up to 250 MHz for two channels. This is used to collect data continuously or to record triggered data, i.e., data collected for a specific time frame[2] (e.g. 200 μs) once a voltage lower than the specified trigger threshold has been measured by the card. Data can be collected for a specified time duration before (e.g. 30 μs) and after (e.g. 170 μs) the trigger. This is important to form a full picture of the TES response to photon incidence, and is used to acquire 1064 nm light signal samples from a continuous wave Schaefter-Kirchoff laser[3] used to introduce light to the TES (via a fiber-coupled system) The efficiency fo this system is discussed in Section 4.4. For the acquisition of triggered data from the Alazar card, the following settings are typically used:

- The trigger threshold is set at (-20 mV).
  Any successful trigger must thus have an amplitude < -20 mV. This value can be modified as per type of pulse sought to be recorded, and must be low enough so as

[1] SQUIDViewer software user manual, from Magnicon GmbH
[2] As buffers, then cumulatively stored.
[3] Fiber-coupled Lasers series 58FCM, for 1064 nm output

to not trigger just electrical noise fluctuations in the signal line. These threaten to overwhelm the data acquisition otherwise.

- 200 μs of data is collected, with 170 μs after the trigger threshold has been crossed and 30 μs before it; this chosen timeline is then saved. This rather large timeline (considering 1064 nm pulse activity in the TES lasts $< 30\,\mu$s) is chosen so as to accommodate larger pulses which can be triggered in the TES system due to background activity.
- The data is read out with a sampling frequency of 50 MHz.

The acquired data file includes triggers which contain information of the voltages measured within a time duration, the sampling frequency, etc.

3.2 Measuring pulses

In order to trigger 1064 nm pulses in the TES, it must first be biased appropriately such that it is at a stable working point within its transition region. The absorption of a single 1064 nm photon can produce different TES pulses at different working points. At higher working points $> 70\%R_N$ it can saturate the TES or be indistinguishable from the electrical noise fluctuation in the SQUID output (exemplified in Section 3.3, Figure 3.2). Bearing these requirements in mind, a typical working point of $30\%R_N$[4] (as delineated in Section 2.6) is chosen.

3.2.1 Pulse Fitting Routines

These pulses can then be described by the theoretical expectation of the TES response to photon incidence from the small-signal theory (SST) with Eq. (2.18), simplified as (from [99]):

$$V_{out,\,SST}(t) = \begin{cases} C_0 - A \cdot \left\{ \exp\left(-\frac{(t-t_0)}{\tau_+}\right) - \exp\left(-\frac{(t-t_0)}{\tau_-}\right) \right\} & , \; t > t_0 \\ C_0 & , \; \text{else} \end{cases}, \tag{3.1}$$

[4] Working points such as 20-40%R_N could also be used.

where

$$A = \left(\frac{\tau_I}{\tau_+} - 1\right)\left(\frac{\tau_I}{\tau_-} - 1\right)\frac{C\Delta T}{(2+\beta)I_0 R_0 \tau_I^2}\frac{1}{(1/\tau_+ - 1/\tau_-)}, \tag{3.2}$$

and C_0 is a constant.
A recorded TES pulse (either triggered or from a timeline of the signal output) is not always successfully fitted with Eq. 3.1 due to difficulties converging: such fits usually fail or fit only an exemplary pulse with the start values (Table 3.1) which does not describe the saved trigger.
A modified version is used instead:

$$V_{out}(t) = c - \frac{2a}{\exp\left(-\frac{(t-t_0)}{\tau_+}\right) + \exp\left(-\frac{(t-t_0)}{\tau_-}\right)}, \tag{3.3}$$

where c is a constant DC offset in the recorded trigger, a is the pulse amplitude, t_0 is the trigger time and $\tau_\pm$ are the rise and decay times of the pulse. In principle, $\tau_\pm$ in Eq. 3.3 are distinct from those in Eq. 2.18; they could be similar in value but cannot be used interchangeably and only represent similar physical features of a TES pulse. Fits processed with this function are more successful, robust and reproducible.

This is realised with a dedicated python package *TESPA* written for this purpose. The specifics of the routine are outlined below:

1. A cost function, to be minimised, is prepared. Here, it is the χ^2.
   The error used in the analysis is 1.5 mV for the voltage data measured by the Alazar card.

2. The minimiser *Minuit* is used to reduce the χ^2, with the start values as described in Table 3.1.

3. In *Minuit*, the *migrad* minimisation method is used to find optimal values of the parameters in V_{out} for minimum χ^2.

4. These optimised values are written to a dictionary along with other fit details and further fit parameters (Table 3.2) which can be constructed from the fit data.

This dictionary is the final result of the fitting procedure for TES pulse, containing the results of the fitting procedure for each data sample. In this form it can be used for pulse selection and discrimination and also directly for analyses with machine learning, as discussed in the Section 4.3.1 and Appendix D.

Fit Parameter	Description	Start Value
c	A constant, denoting the possible DC offset.	0 mV
a	Amplitude of the fitted pulse	Half of the minimum voltage recorded within the single trigger.
t_0	The trigger time, this is the approximate time value at which the steepest dip in the measured voltages is determined. This is also approximately the time of the photon incidence on the TES.	The corresponding timestamp when a voltage value equal to 70% of the minimum voltage triggered is recorded. When left unfixed in the fitting procedure, this is an approximate value and the fit is optimised around it which makes the fitting procedure faster and easier.
τ_+ and τ_-	Time constants for the rise time and decay time respectively.	$2 \cdot 10^{-6}$ s. The V_{out} is symmetric in τ_+ and τ_-, so further selection may be needed for rise time and/or decay time, which is summarily assigned to either by the post-fitting procedure.

Tab. 3.1.: The fit parameters of the modified fitting function V_{out} and their corresponding start values for the fit procedure.

In the fit processing, multiple variables from Eq. 3.3 can be set to a fixed value, i.e. these will not be optimised further. Remaining variables are left 'free' for optimisation by default. Each fitting scheme described next is able to fit the TES pulses, be they from 1064 nm photons which comprise the signal, or background pulses, which will be discussed in Section 4.2. This gives rise to various fit schemes which can be realised for a TES pulse:

1. **Free Fit**: In this scheme, no variables in Eq. 3.3 are fixed, each is left free to be optimised by the minimiser from their respective start values (see Table 3.1). Such a fit (Figure 3.1a) captures the most variation in each individual pulse, due to more fit parameters.

2. **Pulse Shape Fit**: This scheme is motivated by the TES response and the feedback mechanism (see Section 2.2) being identical for each pulse, where the TES returns

Fit parameter	Description
pulse height	The minimum of the voltage in the triggered TES pulse, corrected for the DC offset c.
pulse integral fit	The numerical integral of the result of the fit function (of the voltages) in the trigger window, considering only the triggered/recorded pulse without the DC offset c.
pulse integral raw	The numerical integral of the recorded voltages in the trigger window
chi2 reduced	The minimised cost function $\chi^2 = \sum_i \left(\frac{V_{out}(t_i)-y_i}{error_i}\right)^2$ for the data sample; further divided by the number of degrees of freedom.

Tab. 3.2.: Added fit parameters saved in addition to those in Table 3.1 once the fit is successfully performed.

to its equilibrium working point after photon absorption. This may not hold true for pulses from larger energy depositions or influence of electrical noise, and each pulse would be described better individually using a Free fit.
The rise and decay times are maintained constant with values from the theoretical expectation of the TES pulse features. Parameters a[5] and c would be the only ones being optimised. Such a fit (Figure 3.1c) would best describe the ideal TES response following the small-signal theory (Section 2.2).

3. **Trigger time Fit**: This scheme assumes that the approximate time of photon incidence, i.e. the 'trigger time' t_0 is constant for any photon absorbed by the TES[6], and subsequent features of the pulse(s) may differ. Such a fit (Figure 3.1e) expedites the fitting process but is not generally of more use than the Free or Pulse Shape fit; it eliminates possible variation captured in the TES pulse by large energy depositions.

4. **Others**: Fit schemes with either of τ_+, τ_- fixed and/or with the constant c set to a fixed value of 0 may also be performed. A high influence of the TES noise could motivate keeping only τ_- fixed as $\tau_+ << \tau_-$ is more susceptible to fluctuations in

[5]With constant $\tau_\pm$ this would be proportional to the energy deposited in the TES.
[6]Only within a set trigger window or data acquisition time.

the electrical noise and may vary more. Such fits are also more susceptible to failing and may not always converge, when compared to to other fit schemes.

The fit schemes, in Figure 3.1, are shown as examples with 1064 nm pulses. The Pulse Shape Fit uses the average values of $\tau_{\pm}$, obtained using the corresponding fit parameters from multiple Free fits (on the same dataset). The influence of the electrical noise on the fits and consequently, the energy resolution, is seen and described in the following section. The values for the time constants from the fits are also significantly different from those calculated (mentioned in Table 2.1). This could be due to the electrical noise in the signal line, an incomplete understanding of the TES response due to structural and design features, among other effects.

3.2.2 Energy Resolution

The fitting schemes also influence the energy resolution (ER). This is calculated for 1064 nm photons (1.165 eV), with input from a narrow linewidth 1064 nm laser. The ER is calculated using the numerical integral of the (fitted) TES pulse[7], which scales with the energy deposited on the TES substrate. Using a Gaussian function to describe the pulse integral distribution, the ER can be defined as:

$$ER(\%) = \frac{\mu}{\sigma}\bigg|_{Gauss} \cdot 100, \tag{3.4}$$

where μ is the mean of the distribution and σ its standard deviation.
The Pulse Shape fit achieves the best ER of (7.79 ± 0.1)%, the Free Fits achieve an ER of (11.91 ± 0.11)% and the Trigger Time fits achieve the worst ER of (14 ± 0.15)%, as can be seen in Figure 3.1.
The influence of the noise in the signal line is main source of the difference in the ERs obtained from the fit schemes. This influence is minimal for the Pulse Shape fits as $\tau_{\pm}$ are fixed and it slightly increases for the Free fits, which find better (and thus more varying) fit values for every individual pulse. The Trigger time fit is highly restrictive in its choice where the $\tau_{\pm}$ must be found as t_0 is fixed; thus varying values for the $\tau_{\pm}$ are obtained.

[7] The numerical integral of the raw TES pulse can also be obtained but is not used here.

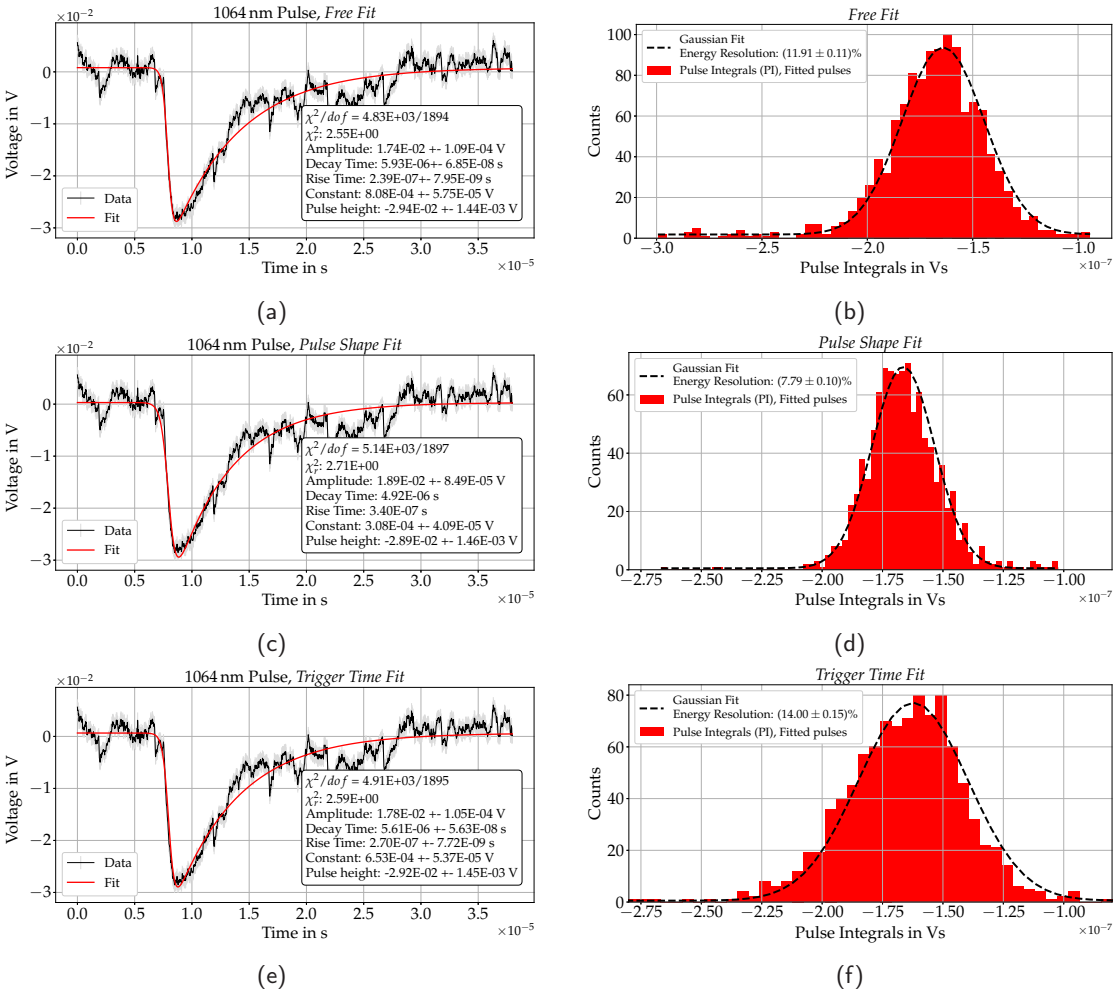

Fig. 3.1.: Examples of some fit schemes for a 1064 nm photon pulse (in a shorter 38 μs trigger window, and at TES working point of 30%R_N and gain-bandwidth product 1.5 GHz) and their corresponding energy resolution (ER). (a) shows the pulse fitted with the Free Fit, (b) with the Pulse Shape Fit and (e) with the Trigger Time Fit described in Section 3.2.1. The Pulse Shape Fit uses the average values of $\tau_\pm$ from the Free fits of 1000 1064 nm photon pulses: $\tau_+ = 0.34 \pm 0.1\,\mu$s and $\tau_- = 4.92 \pm 0.7\,\mu$s. Minor differences in each approach can be seen from the fit itself and the fit parameters. The energy resolutions for each type of fit, calculated from the corresponding pulse integrals of 1000 fitted 1064 nm pulses, are shown in (b), (d), and (f).

3.3 Working Points

As previously mentioned, the incidence of a photon can produce different pulses in the TES depending on the chosen working point (Figure 3.2b). This translates to pulses with pulse heights larger in magnitude for a lower working point, e.g. 30%R_N, compared

to a higher working point $70\%R_N$, as can be seen from Eq. 2.18 where $\delta I(t) \propto \frac{1}{R_0}$ (R_0 being the working point TES resistance). Due to the influence of electrical noise in the output, features of the TES pulse may vary but the rise and decay times remain largely unchanged.

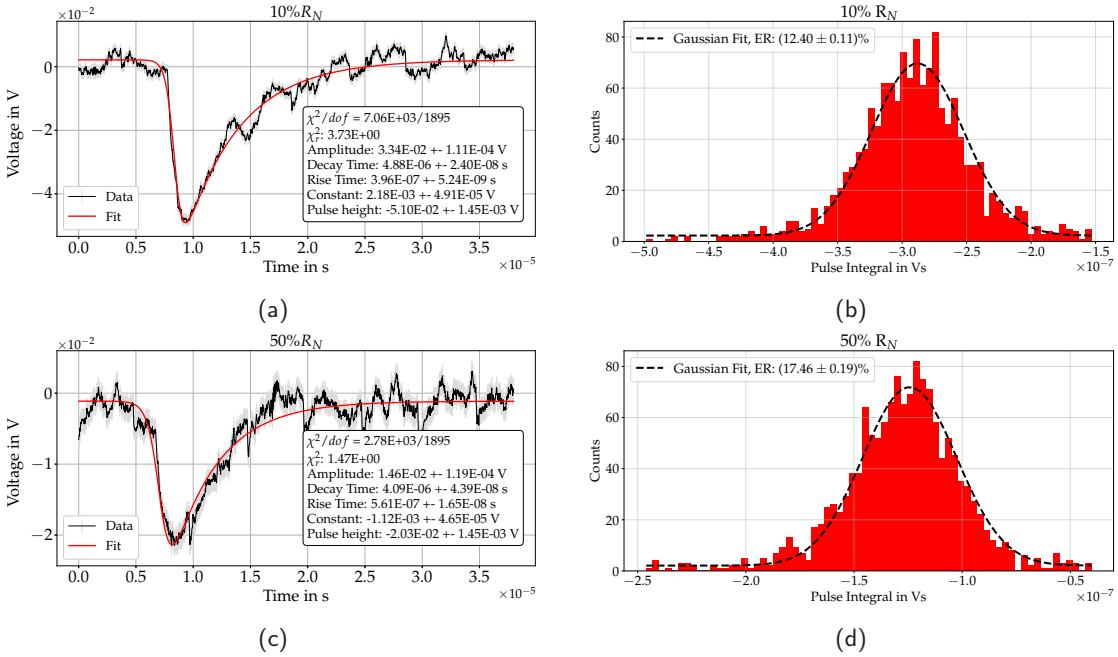

Fig. 3.2.: (a) and (c) show a 1064 nm photon pulse triggered in the TES at working points of 10%R_N and $50\%R_N$ respectively, fitted with the Trigger Time Fit scheme (as an example) like the pulse triggered at $30\%R_N$ in Figure 3.1e. The difference in the magnitude of the pulse height and the consequent influence of the electrical noise (see Figure 3.3) can be seen. (b) and (d) show the distribution of pulse integrals for 1500 such 1064 nm photon pulses triggered at working points of 10%R_N and $50\%R_N$ respectively. The corresponding energy resolution (at 1.165 eV) is $(12.4 \pm 0.11)\%$ and $(17.46 \pm 0.19)\%$ respectively.

From the small-signal theory, this is expected as the rise/decay times in a strong negative ETF setup with $\tau_- >> \tau_+$ are not dependent on the working point. The distribution of some fit parameters for varying working points is shown in Figure 3.4.
The energy resolution for 1064 nm photons also changes from one working point to another, typically worsening with higher working points. This is due to the increasing influence of the noise (Figure 3.3) in the signals. Using Eq. 3.4 to calculate these ERs, some examples are shown in Figure 3.2.

The overall fit parameters thus show significant difference due to a change in the TES working point. Ensuring the consistency of the working point via the necessary biasing

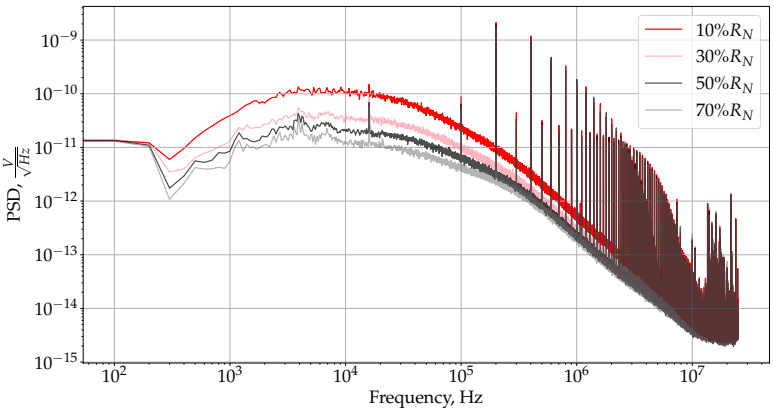

Fig. 3.3.: The spectral density for the electrical noise in the signal line is shown above, for different working points. Lower working points (like 10%R_N) have higher noise compared to working points with increasing normal conducting behaviour. The wholly unbiased TES signal noise is dominated by the load resistance R_L of the TES circuit. The $\mathcal{O}(100)$ kHz harmonics are suspected to originate in the SQUID electronics (connector box) from a dc-dc converter; these remain uncritical for signal and background measurements for a gain bandwidth product of 1.5 GHz (used here).

is thus essential for a consistent dataset of either 1064 nm photons and/or background pulses triggered in the TES. A working point of $30\%R_N$ as mentioned previously (Section 2.6) is the one used for data acquisition as it ensures a good ER and high dynamic range in the TES, and is not fully saturated by the absorption of a single 1064 nm photon.

3.3.1 Outlook

The various fit schemes mentioned can be used for pulse analysis depending on the final application intended. In order to best describe each TES pulse individually with no prior assumptions, the Free fit scheme assimilates the most variation in the fit parameters. Comparatively, the Pulse Shape fit captures lesser variation since the pulse shape (for photon incidence and absorption i.e. $\tau_{\pm}$) is assumed to be constant, though it has a better ER of $\sim 8\%$ compared to $\sim 12\%$ for the Free fits (considering 1064 nm photons).
The electrical noise fluctuation in the TES setup is understood to be the primary cause of this variation. The Pulse Shape fits can be used for the accurate description of those pulses which are expressly from photon incidence, i.e. pulses with rise and decay times similar to those of 1064 nm photons and consistent with small signal theory. This is inadequate when considering backgrounds, which may stem from various sources and not always from the direct incidence of photons on the TES. Free fits are best suited for

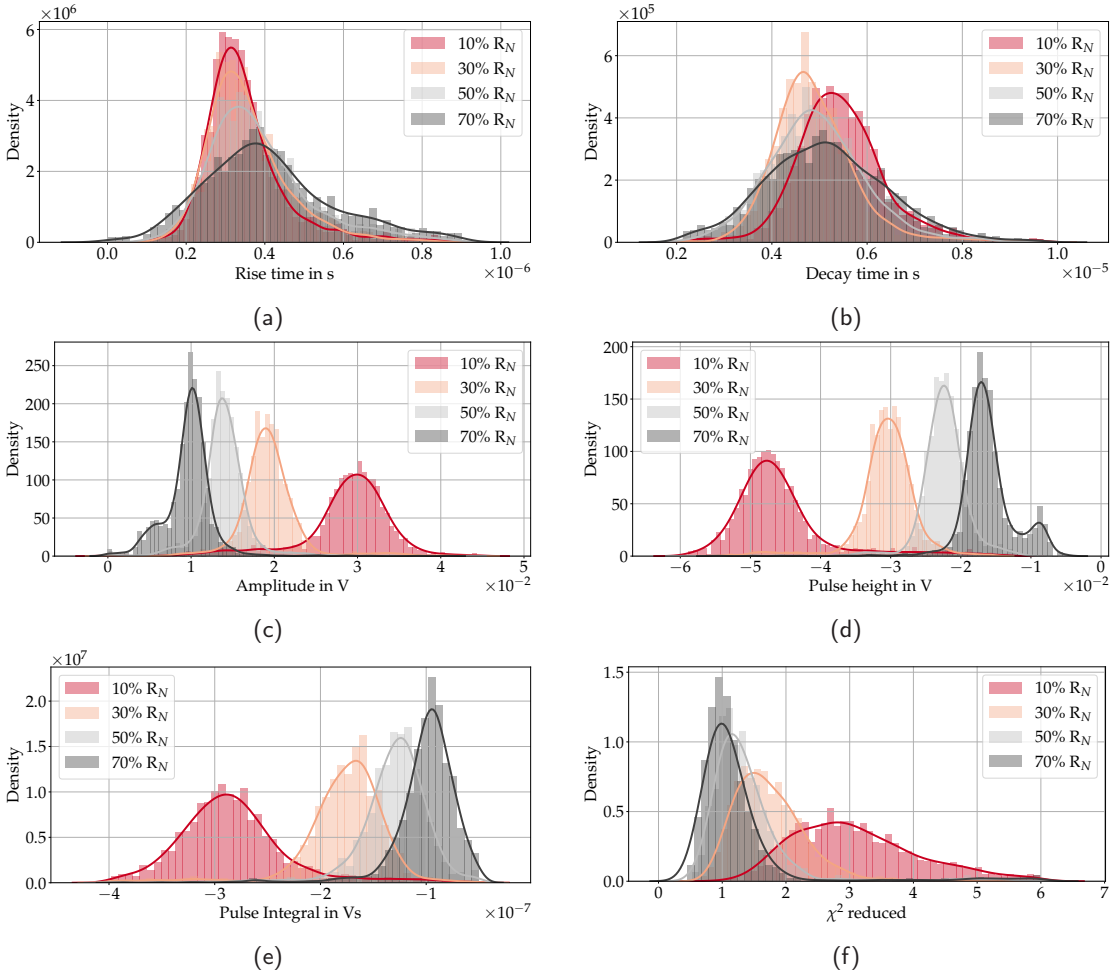

Fig. 3.4.: The histograms of various fit parameters for selected TES working points of 10%R_N, 30%R_N, 50%R_N and 70%R_N. The influence of electrical noise impacts the resolution as seen for the rise and decay time distributions in (a) and (b) though the central values ($\sim 0.34\,\mu$s and $\sim 5\,\mu$s respectively) are largely unaltered. This influence also shows up in the pulses triggered at the 70%R_N working point ((c) and (d)) where 1064 nm photon pulses have typically lower amplitude/pulse height.

purposes of pulse selection and background rejection, as will be discussed in Section 4.2. Multiple variables can be used to characterise the TES pulses, and these can be highly influenced by the electrical noise. This can hamper an efficient characterisation of the pulses. The use of filters can also decrease this influence, the investigations for which are out of the scope of this work and will be undertaken later. This can also be prevaricated by the use of other well-established pulse analysis methods, which we discuss next.

3.4 Principal Component Analysis (PCA)

The photon pulse as seen from the trigger in the TES is influenced by the electrical noise. The pulse, with minimal noise, has to be inferred from this, to achieve the full capacity of the TES detector and its functionality, as was done with the pulse fitting with the function Eq. (3.3). We pursue another method for pulse characterisation trying as best as possible to retrieve a TES pulse with the subverted impact of the electrical noise. Using the well-established Principal Component Analysis (PCA) method, we can obtain "cleaned" TES pulses and parameters akin to the fit parameters which could possibly be used for later pulse analysis and discrimination.
The PCA method, as outlined in [100, 101], reduces the inherent dimensionality of the dataset that the PCA is performed on, while largely maintaining its statistical variation i.e. its information.
Within a single dataset[8], each data point v_j is described as the linear sum of a basis set of orthonormal parameters called the principal components (PCs) represented by w_j:

$$v_j = \sum_i^T s_{ij} w_j \, (\implies v_1 = s_{11} w_1 + s_{12} w_2 + \ldots + s_{1T} w_T) \ , \tag{3.5}$$

where T is the total number of triggers/pulses in the dataset. A choice can be made for the bases w_j such that the first few PCs capture the most information of the original pulse, and succeeding PCs capture exponentially lesser and lesser information. The methodology for this is further described in Appendix C.
By retaining only the first N PCs, we can thus reduce the dimensionality of the dataset while still keeping the necessary information intact:

$$v_j = \sum_i^N s_{ij} w_j \, (\implies v_1 = s_{11} w_1 + \ldots + s_{1T} w_N) \ . \tag{3.6}$$

The higher, noise-carrying components are truncated and the acquired triggers can be reconstructed. These reconstructed pulses using the PCs, are shown in Figure 3.5, where the use of only the first PC already traces out the TES pulse faithfully. These recreated pulses are not further fitted using any function, such as Eq. 3.3.

The energy resolution (ER) of the TES detector with the PCA can be found, adopting a asimilar approach as was with the fitting procedure, from the distribution of the

[8] A dataset containing one kind of pulse only i.e. similar pulses originating from a single physical source.

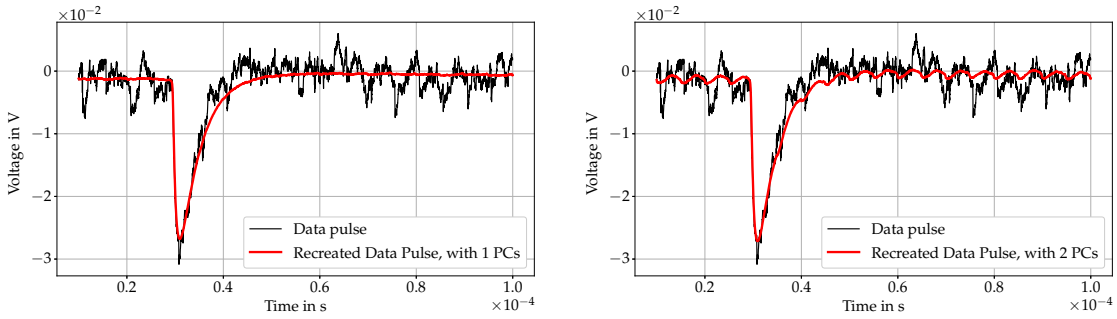

Fig. 3.5.: Recreating a TES pulse using PCA, with the first and then the first two PCs is shown in (a) and (b) respectively. Already the reconstruction of the pulse shows elements of noise influence when using the second PC. A dataset of ∼1000 1064 nm pulses from the detector via the acquisition scheme is used here, acquired within a few seconds, ensuring no significant variation due to a change in the working settings or inclusion of background pulses of other physical origins. This would hamper the performance of the PCA. The working point of the detector is fixed at $30\%R_N$, as before.

pulse integrals. This, for the pulses recreated with the PCA, is shown in Figure 3.6a, in comparison to the pulse integral distribution for the same dataset fitted with the Free fit scheme described in Section 3.2.1. A Gaussian function is used to describe the distributions, and the ER is obtained using Eq. 3.4. The PCA approach (with the first PC only) results in an ER of $(7.55 \pm 0.05)\%$, while the Free fits resulted in a worse ER of $(11.91 \pm 0.16)\%$. The use of successive PCs to further recreate the TES pulse contributes only to additional noise elements, resulting in an inferior ER. This is seen in Figure 3.6b, where the ER is significantly worsened when recreating the pulses with 3 or more PCs. The single contributions of each PC is further shown in Figure 3.8b (in comparison to the TES pulse from the data acquisition), where successive PCs confirm the addition of electrical noise to the recreated pulse. The statistical variance σ_j of the original dataset captured in each separate PC j is calculated using the coefficients s_{ij}:

$$\sigma_j = \langle s_{ij}^2 \rangle - \langle s_{ij} \rangle^2. \tag{3.7}$$

This variance, for each succeeding PC, reduces sharply as inferred from Figure 3.8b, and is shown in Figure 3.7.

The best ER achieved with the fitting schemes is $(7.79 \pm 0.1)\%$ with the Pulse Shape fits, and is only marginally worse than the one achieved with a basic PCA approach. However, the PCA proves inadequate on some fronts for our purposes:

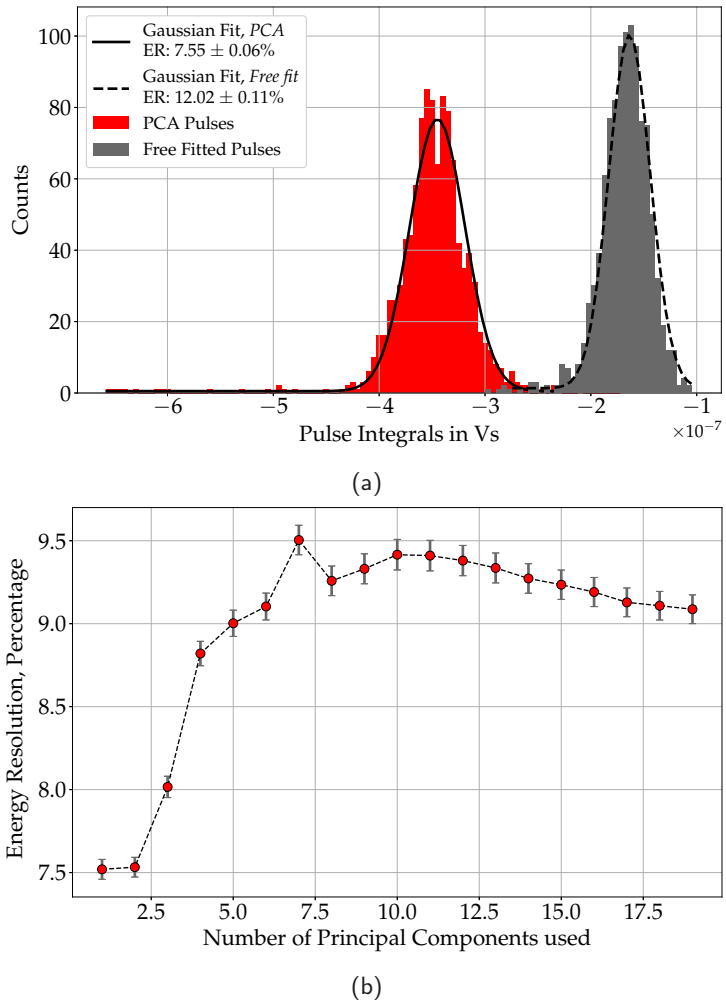

Fig. 3.6.: The distribution of the pulse integrals from the Free fit scheme and for PCA-recreated pulses is shown in (a), with the PCA approach resulting in a better ER of $\sim 8\%$ compared to $\sim 12\%$ for the Free fits. The pulse integrals from the Free fits are corrected for any DC offset within the pulse itself (see Section 3.2.1) while the PCA is not, leading to a difference in the central values of the distributions. The dataset used for both analyses is the same ∼1000 1064 nm pulse sample described in Figure 3.6a. (b) shows the evolution and deterioration of the ER when reconstructing TES pulses with increasing PCs.

1. The fitting scheme used most, the Free fit, has worse ER than the PCA but captures more information via multiple fit parameters. These can be used for pulse discrimination whereas the PCA has only the first PC which could do so. The distributions of the other PCs are not very localised, as seen in Figure 3.7, making them unfit for use in pulse selection.

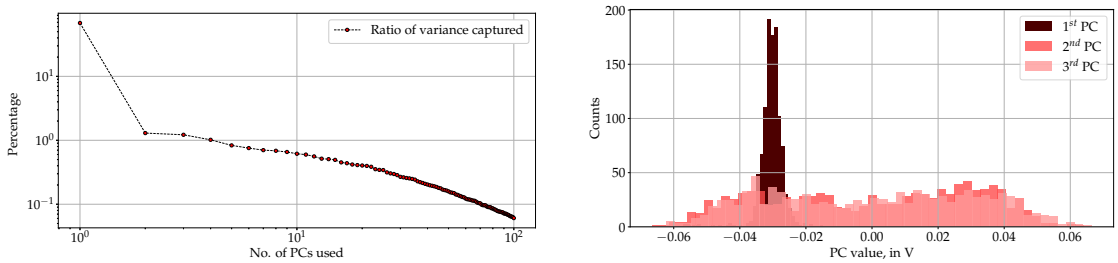

(a)

Fig. 3.7.: The percentage of variance explained by each independent PC is shown in (a), with the sum of all percentages (or ratios) over the dataset, i.e. over the number of pulses in the dataset is 100% (or 1). The PCs have been selected to ensure that the first few PCs retain the most statistical variance of the original dataset. The variance captured in the first PC (σ_{PC_1}) is about two orders of magnitude greater than the variances captured in the second and third PCs (σ_{PC_2}, σ_{PC_3}), and this course continues, with σ_{PC_j} rapidly decreasing as a function of j. (b) shows the distributions of the first few PCs for the ~1000 1064 nm photon pulses in the dataset. Using these PCs to recreate the pulse in Figure 3.8a would result in the independent contributions in Figure 3.8b. To recreate, for instance, the TES pulse in Figure 3.8a the corresponding PCs used include: $w_1 = -0.0289$, $w_2 = -0.0227$, and $w_3 = -0.0262$.

2. Using the first PC ($w_1(t)$) already results in a faithful trace of the TES pulse. This would be expected theoretically in the small-signal limit, in which the pulse height would be proportional to the incident energy or number of photons for a single pulse shape, i.e. for cases which could feature pile-up of multiple signal photons. This would make it a useful approach for only distinguishing TES pulses in the few-photon limit using only a single parameter (akin to [102]), and not further.

3. The PCA is also not very reliable as it can only work best with a dataset containing pulses of a single physical origin, and not multiple pulse types in the same dataset. This will lead to an inadequate reconstruction of TES pulses. The various pulse types and their populations can skew the reconstruction of the pulses. This drastically reduces its use for any pulse characterisation.

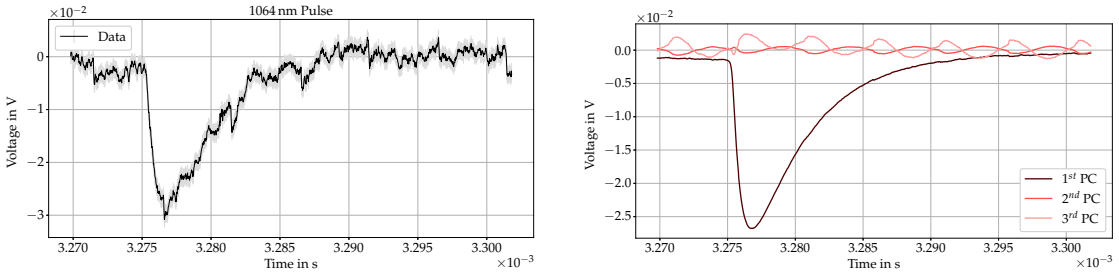

(a) (b)

Fig. 3.8.: A comparison of the single contributions of the first three PCs (in (b)) for the recreation of a 1064 nm pulse in (a) is shown above. The impact of the fluctuations assumed to be due to the electrical noise is captured in the contributions due to the 2^{nd} and 3^{rd} PC, which gets successively higher in magnitude for additional PCs.

3.5 Conclusion

The utility of the PCA for TES pulse discrimination is summarily limited, while it efficiently de-noises the pulse and leads to a good ER $< 8\%$ at 1.165 eV. Though the Free fit scheme entails a lower energy resolution (and possibly lower distinguishing power) of $\sim$12%, the use of other fit parameters assists in pulse discrimination. Thus, the Free fit scheme is adopted as the baseline for pulse analysis.

The analysis also benefits from the use of Machine Learning (ML) techniques as mentioned in Appendix D. This works alongside the fitting procedure, using the obtained fit parameters for a TES pulse and, for further investigation, will use the full TES pulse. It is also important to ascertain the performance of the fitting procedure for photons of other wavelengths, to understand the linearity of the TES response. For most pulse types, however, the (Free) fitting procedure is always successful. Pulse types (mostly background events) which are not related to the small signal theory and have other physical origins[9], can still be characterised well enough for them to be suppressed (further seen in Section 4.3.1).

[9]Such as energy deposition not on the TES directly.

4 TES for ALPS II

The TES must fulfil the criteria discussed in Section 1.3 in order to be implemented in the ALPS II experiment. The necessary achievement of an adequately low background rate in the TES is particularly challenging. Details regarding pulse characterisation have been discussed in Section 3.2.1, which will be used to understand and minimize the background events. This is done by employing the parameters from the fits performed on the pulses to construct pulse selection strategies and optimise them. The results of these analyses are also mentioned in [9]. Ongoing efforts to achieve a high system detection efficiency in the TES setup will be discussed in this section, along with the challenges involved therein. The application of different hardware options in order to suppress the backgrounds in the TES will also be discussed.

4.1 Signals

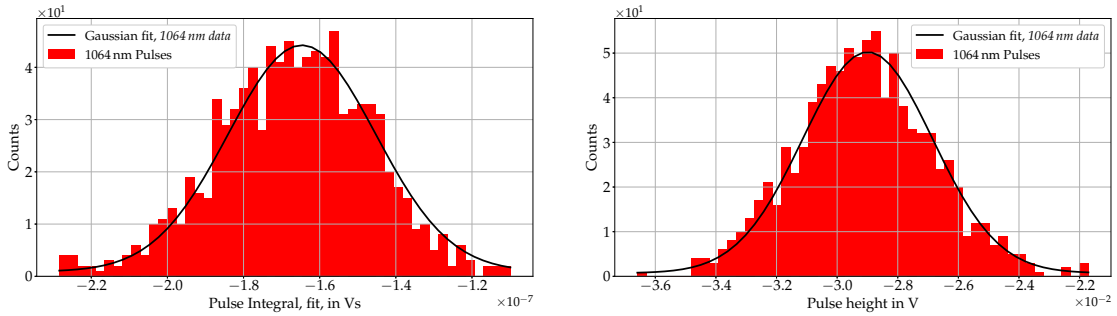

(a) (b)

Fig. 4.1.: (a) and (b) show the distribution of the pulse integrals and heights for a dataset of ∼1000 1064 nm pulses fitted following the Free fit scheme in Section 3.2.1. Similar distributions are also made for other fit parameters mentioned in Tables 3.1, 3.2 though not all are used for pulse selection. 1064 nm photons, with this working point, typically have a rise and decay time constant of 0.2 and 5 μs respectively, with a pulse height (-)30 mV.

A dataset of ∼1000 1064 nm single photon pulses is used to understand the response of the TES by fitting the pulses following the procedure outlined in Section 3.2.1. The

fit parameters obtained include the rise and decay time constants, pulse heights, etc. among other pulse characteristics (examples in Figures 4.1a, 4.1b). In their totality, they constitute the whole picture of a 1064 nm pulse in the TES and can be used to select 1064 nm pulses (or 1064 nm-like pulses) from a dataset also containing background pulses.

4.2 Backgrounds

In general, the TES can be susceptible to various kinds of background pulses [103]. These are triggered in the TES due to photon incidence or energy deposition in the TES (or the TES's immediate environment), with multiple sources. For our setup, we broadly differentiate the triggered background events into two categories:

- **Intrinsic background events**: These are pulses triggered in the TES when there is no optical fiber attached to it or in its vicinity. These are the backgrounds that would afflict the TES due to its design and setup, and are thus intrinsic to it. The background sources that can lead to such events are comprised of (but not limited to) energy deposition due to cosmic rays and their secondary effects such as Cherenkov and transition radiation, radioactivity in the setup, and the influence of electromagnetic fields in the setup environment [103].

- **Extrinsic background events**: These are pulses triggered in the TES when there is an optical fiber attached to it directly, i.e in the white ferrule on the detector module and without the input of any photons. These are the backgrounds afflicting the TES when external influences are introduced to it. As such, the extrinsic backgrounds include the intrinsics (and their general associated sources) as well but are suspected to be dominated by the photons originating from black body radiation coupling into the optical fiber [69] (from the laboratory environment) and their pile-ups. These backgrounds capture a fuller and more realistic picture of what the backgrounds in the final TES setup will look like when the optical fiber will be connected to the ALPS II experiment. Other sources of backgrounds include fluorescence and luminescence, parametric downconversion of 532 nm photons in the fiber and optical components, etc.

TESs typically have a low background rate of $\mathcal{O}(10^{-2})$ cps, which is negligible for most experiments in comparison to a signal rate of $\mathcal{O}(100)$ cps (as in [104, 105]).

With the pulse characterisation using the Free fit scheme, the individual fit parameters for each background pulse can be reliably calculated (Section 3.2.1). The methods adopted for pulse discrimination follow a more phenomenological approach.
This is important, bearing in mind that it is essentially necessary for the ALPS II experiment to detect a single 1064 nm photon signal sufficiently distinguishable from a background event, and is necessary to confirm that the adequately low background levels (with respect to 1064 nm photons) can be achieved.
Ascertaining the influence of different background sources is also equally important, but this is beyond the scope of this work and forms the next phase of investigations. It remains an important goal for the development of a TES detector system, enabling possibly also the direct detection of dark matter [106]. In the following section we will examine different background events and the methods adopted to obtain a low background rate.

4.3 Intrinsic Backgrounds

Keeping the detector setup in its most skeletal form, i.e. without any external input from the optical fiber to the TES (or its vicinity), the corresponding 'intrinsic' background pulses collected are investigated. These are triggered in the detector when it is maintained at a working point of 30%R_N, and the trigger setup described in Appendix 3.1 is active. Though the final setup of the TES detector for the ALPS II experiment will feature an optical fiber connected to the TES, it is important to investigate the intrinsics (as they will be referred to hence) to:

1. Determine the (lowest possible) intrinsic background rate. In the case that this rate is impractically high (after pulse selection), the TES is a poor candidate for ALPS II as a detection scheme.

2. Determine the influence of the optical fiber on the backgrounds, and ascertain how the additional backgrounds due to it will compare to estimates (and suspected sources) for these backgrounds, and

3. Determine the use of a TES detector for other physics goals as well, which require satisfactorily low background rates, such as direct dark matter searches.[1]

[1]The application of similar sensitive cryogenic photon detectors such as superconducting nanowires has been accomplished too for such searches [107].

ALPS II aims to detect 50 1064 nm signal photons[2] ($N_s = 50$) over a data taking period of 20 days with a significance $S = 5\sigma$, and a detection efficiency $\epsilon = 50\%$ [108]. Using this to calculate the number of background events N_b in (from [109])

$$S = 2\left(\sqrt{\epsilon \cdot N_s + N_b} - \sqrt{N_b}\right) \tag{4.1}$$

results in a maximum of 14 background events collected over 20 days, entailing an **upper limit on the dark rate**: $8.1 \cdot 10^{-6}$ cps.

In order to check the background rate over this period, a data acquisition was set up to collect background pulses over 20 days. Checks were periodically made over this period to ensure that the system settings (such as SQUID FLL-mode activity and TES working point) did not waiver and the cryostat functioned smoothly. Separate runs were then stitched together yielding a final count of ∼37,000 intrinsic background events, with a raw dark rate $2.13 \cdot 10^{-2}$ cps (Figure 4.2a).

4.3.1 Pulse Selection

The majority of the background pulses triggered can be, like the example in Figure 4.2b, easily discerned from a 1064 nm photon pulse, using, for example, the decay time constant or the pulse height. An approach to reject such events and select pulses indistinguishable from 1064 nm photon pulses is discussed next.

Symmetric Cuts

The collected intrinsic background pulses are compared directly to the 1064 nm single photon pulses. All pulses are fitted following the Free fit scheme described in Section 3.2.1, resulting in multiple fit parameters which are used to reliably distinguish pulses from each other. A sample of ∼1000 1064 nm photon events is used and the histograms of fit parameters of these 'signal' photons are fitted with a Gaussian distribution.
This is used to define a selection region around each fit parameter:

$$\mu_{\text{ fit parameter}} \pm n \cdot \sigma_{\text{ fit parameter}}\,, \tag{4.2}$$

[2] Amounting to a photon regeneration rate $\sim 2.8 \cdot 10^{-5}$ cps.

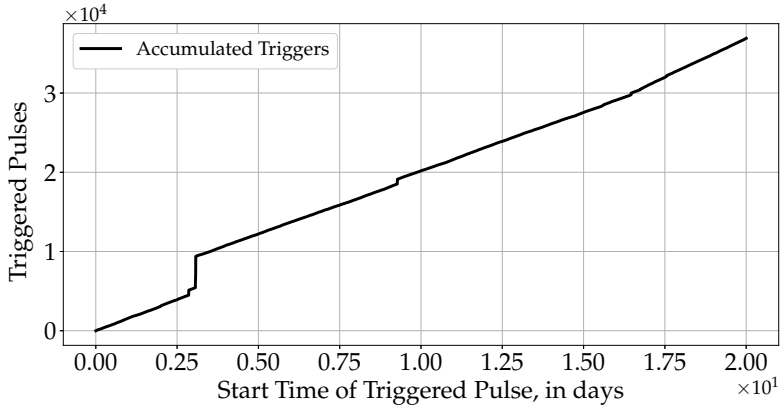

(a)

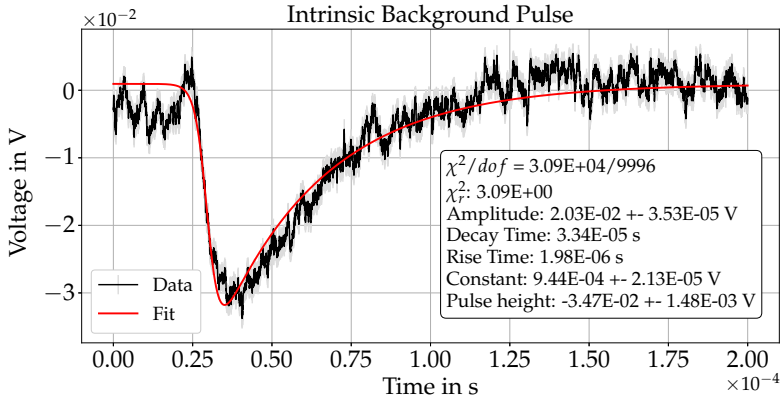

(b)

Fig. 4.2.: (a) shows the background pulses triggered in the detector over the course of the 20 day-long DAQ, an example of which is shown in (b). The abrupt increases in the number of pulses triggered, such as those near the 3-day mark, are caused due to electromagnetic activity near the detector setup from electronic devices. The exemplary intrinsic background pulse in (b) is characterised following the Free fit scheme, with fit parameters also shown in the plot.

where $\mu_{\text{fit parameter}}$ is the mean of the Gaussian distribution and $\sigma_{\text{fit parameter}}$ is its standard deviation[3]. For various values of $n \in \mathbb{R}_{\geq 0}$ this region can be made either more or less confined. Selecting pulses (which have fit parameters) within this region ensures the acceptance of as many 1064 nm photon pulses as possible while rejecting the background pulses. These regions, which establish symmetric cuts at $\mu \pm n \cdot \sigma$ around the peaks of the respective distributions for the fit parameters, are shown in Figures 4.3, 4.4 for $n = 3$.

[3]These fit parameters are described in Tables 3.1, 3.2.

n	**Surviving Events**	**Dark Rate**, in 10^{-6} cps	**Signal photon acceptance**	**Significance**
2	2	$1.15^{+1.51}_{-0.362}$	65.09%	7.56
2.5	9	$5.20^{+2.36}_{-1.21}$	81.18%	5.66
3	12	$6.9^{+2.62}_{-1.47}$	89.8%	5.24
3.5	24	$13.88^{+3.43}_{-2.28}$	96.7%	4.2
4	44	$25.46^{+4.42}_{-3.27}$	100%	3.35

Tab. 4.1.: The cuts $\mu_{\text{fit parameter}} \pm n \cdot \sigma_{\text{fit parameter}}$ for varying n are applied to the datasets, for the fit parameters shown in Figures 4.3, 4.4. For $n = 3$, this yields a dark rate $6.9 \cdot 10^{-6}$ cps with an acceptance $\sim 90\%$, which is compatible with the limit of $8.101 \cdot 10^{-6}$ cps. The significance S is calculated from Eq. (4.1) using a detection efficiency $\epsilon = 50\%$ for illustration.

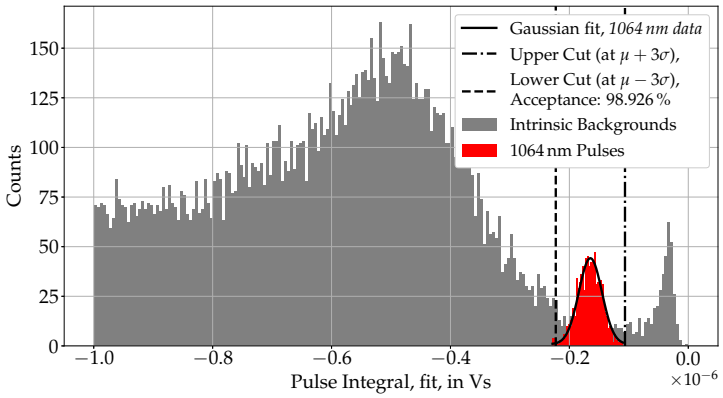

(a)

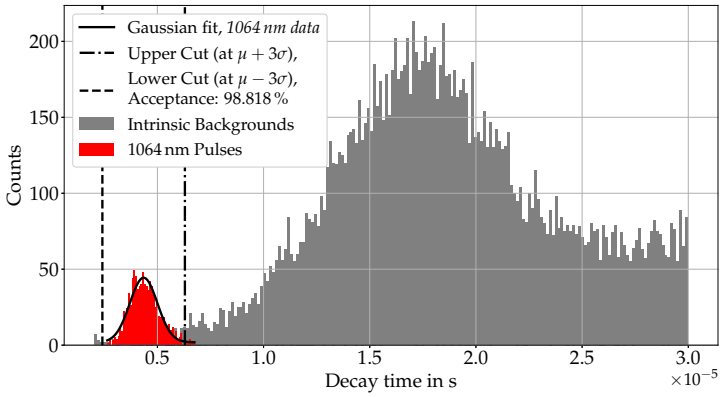

(b)

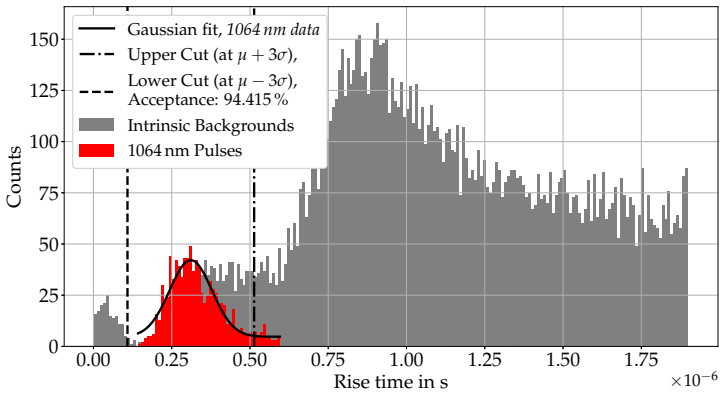

(c)

Fig. 4.3.: The distributions for the pulse integral and time constants of the intrinsic background events and 1064 nm photons is shown, with exemplary cuts at $\mu \pm 3\sigma$. About 37,000 intrinsic background events (collected over 20 days), and ∼1,000 1064 nm photon pulses (collected over ∼1 s) are used here. The distribution of the pulse integral (theoretically proportional to the energy deposited in the TES) continues on below $-1 \cdot 10^{-6}$ Vs but is not shown above. The background pulse integrals with magnitude lesser than the 1064 nm photon pulses are typically dominated by electronic noise triggers.

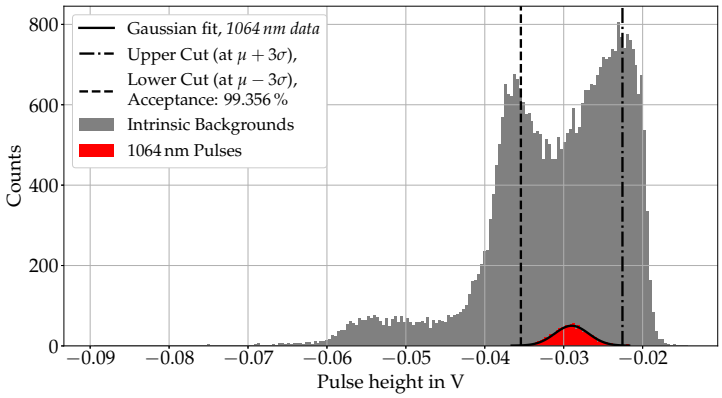

(a)

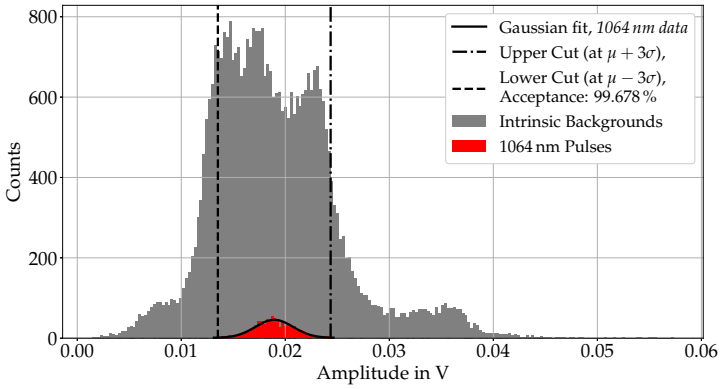

(b)

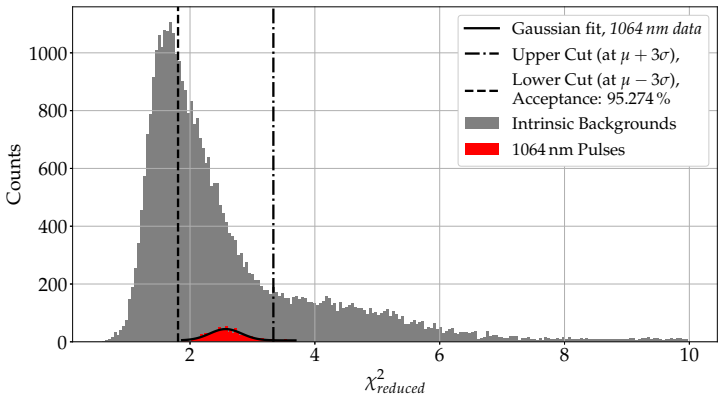

(c)

Fig. 4.4.: As in Figure 4.3, the distributions for the pulse height and other fit parameters of the intrinsic background events and 1064 nm photons is shown, with similar exemplary cuts at $\mu \pm 3\sigma$. From the distributions of the pulse heights (and amplitude) we see that within the intrinsic background, there are distinct pulse types, which could be from different background sources.

The cuts established for various n are applied to the signal and background datasets. The percentage of the 1064 nm 'signal' photon pulses which survive the cuts is called the signal photon acceptance, and pulses which remain after the cuts are applied to intrinsic background pulses are termed the surviving events. Over the 20 day period, these typically result in dark rates $\mathcal{O}(10^{-6})$ cps; these results are summarised in Table 4.1.

Figure 4.6 shows the time each specific background event, which survives the $\mu \pm n \cdot \sigma$ cuts applied to it, was originally triggered in the 20 day long data taking period. The evolution of the accumulated (remnant) background events and their rate is shown. With the $n = 3$ cuts used, 12 events remain over 20 days which is lesser than the limit specified. This results in a low enough (intrinsic) background level for the TES, with respect to ALPS II requirements.
An example of a background pulses which survive the stringent $n = 2$ cuts is shown in Figure 4.5, compared to a 1064 nm pulse. This is indistinguishable (with a cursory look, and within the selection procedure) from 1064 nm photon pulses and could constitute a near-irreducible background population.

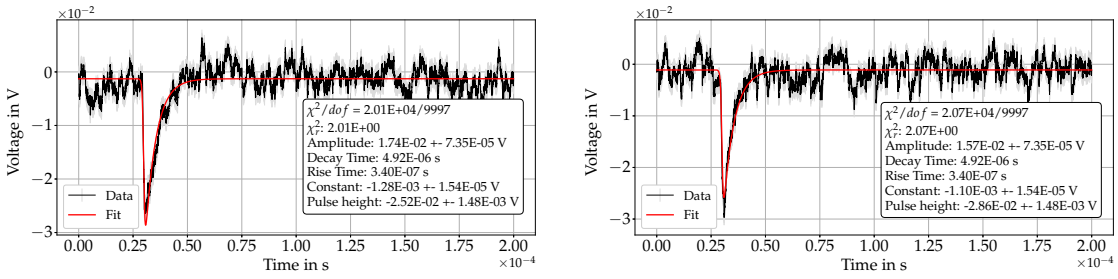

(a) (b)

Fig. 4.5.: (a) shows an intrinsic background pulse which remained after stringent $n = 2.5$ (symmetric) cuts were applied to the background dataset. This is indistinguishable from a 1064 nm photon pulse, shown in (b), and constitutes a near-irreducible background population.

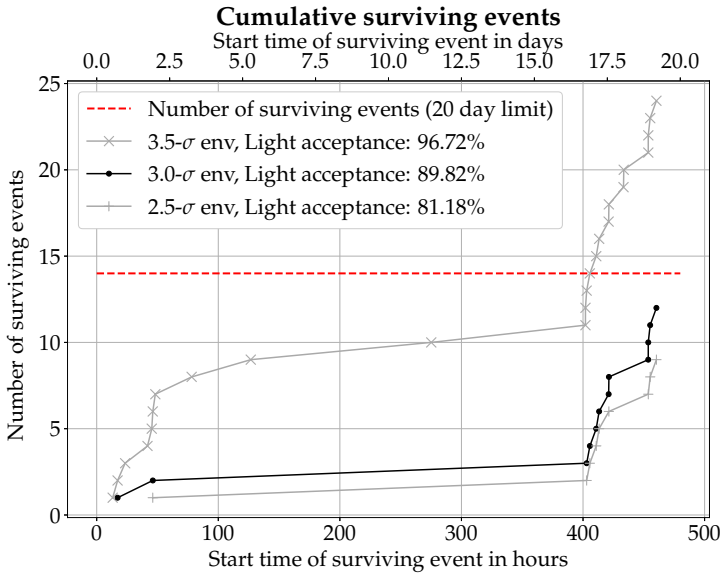

(a)

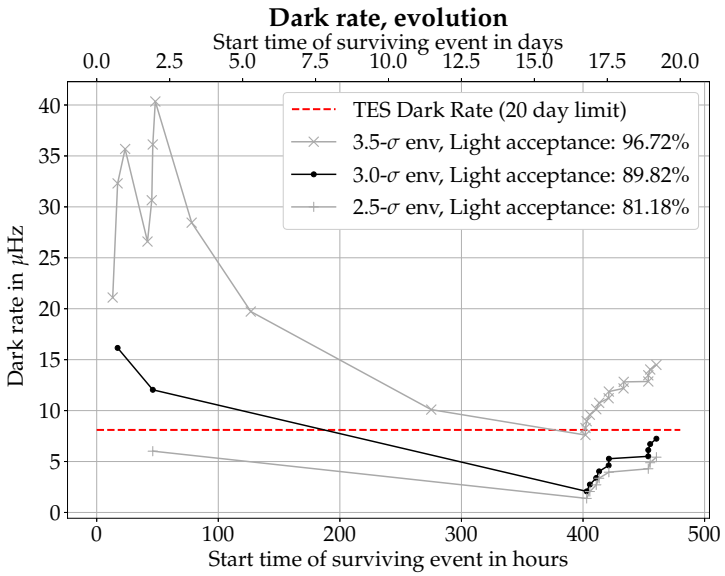

(b)

Fig. 4.6.: (a) shows the time each specific background event, which survives the $\mu \pm n \cdot \sigma$ cuts applied to it, was originally triggered in the 20 day long data taking period. With the cut used here we obtain 12 events over 20 days, lesser than the limit specified. The burst of 1064 nm-photon-like events seen near the 400-hour mark is being investigated, they could originate from electromagnetic fields around the TES or some luminescence effects, and do not survive the cuts due to their difference from the goal photon regeneration rate of ∼1-2 photons per day.

Fine-tuned Cuts

The symmetric cuts established in Figures 4.3 and 4.4 feature a drawback: the distributions of the fit parameter of signal events is not a perfectly Gaussian distribution and is only modelled as one. The selection of 1064 nm photons can be optimised and made more efficient, as for some fit parameter distributions this method of finding cuts can inadvertently de-select some 1064 nm photons. Another important drawback is that this method also does not take into account the contribution of the intrinsic background pulses in these distributions.

For a fit parameter distribution, a cut decision should also factor in the number of background pulses contributing to each bin. This can help ensure that background pulses can be more efficiently rejected. These improvements are made by fine-tuning the pre-existing symmetric cuts. This is done by defining a ratio ζ:

$$\zeta_{bin} = \left[\frac{\text{Number of } (\textit{weighted}) \text{ 1064 nm pulse entries}}{\text{Number of background pulse entries}}\right]_{bin} \tag{4.3}$$

which compares, for every fit parameter distribution, the number of entries from 1064 nm signal photons and background pulses, in each bin. The signal 1064 nm photon entries in each bin are weighted using a dynamic weight, differing from bin to bin, such that the sum of all signal events in the histogram finally amounts to 50 signal photons. This is done to compare the backgrounds directly to the signals expected to be collected over the 20 day period in the detector. This normalized histogram provides a more clear visualization of what the histograms of the fit parameters (for signal photons) will look like.

An algorithm fine-tunes cuts in the region where the symmetric cuts are first established, by choosing a pre-decided ratio limit ζ_{limit}. This can depend on the number of pulses (1064 nm signal photon pulses or background pulses) and is as such an arbitrary number depending on the analysis and dataset size. The bin with a value of ζ_{bin} which is larger (or smaller) than a pre-decided ratio limit is used to establish a fine-tuned cut. The cut can be at either bin edge to include or exclude the bin in question. Emphasis is laid on the binning procedure, as this must have the same bins (number and bin width) for the distributions of the backgrounds and signal photons, and no bin can go empty with respect to background pulses.

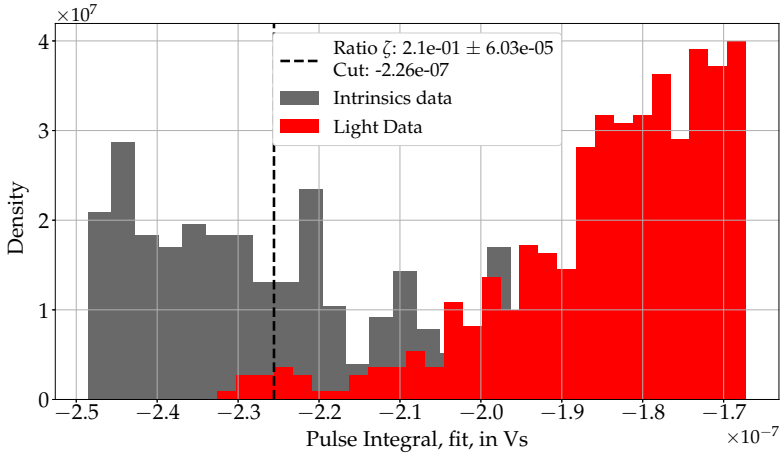

(a)

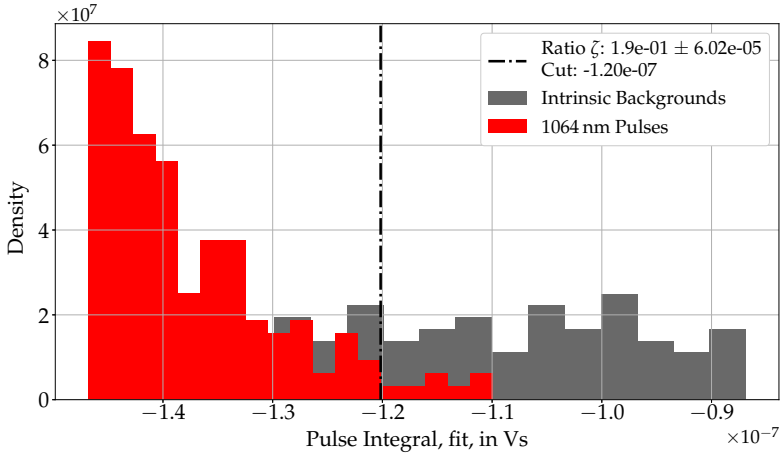

(b)

Fig. 4.7.: (a) shows the updated, fine-tuned cut as dictated by the ratio limit $\zeta_{limit} = 0.2$ and the bin (edge) where this value is exceeded in the distributions of the pulse integrals of the 1064 nm photons pulses and intrinsic background pulses. In (b) the opposite is true; with the cut at the bin edge where the ratio ζ_{bin} is lower than the limit of 0.2. The fine-tuning of the symmetric cuts shown in Figures 4.3, 4.4 can be found in Appendix B.

An example is shown for the pulse integral, in Figure 4.7, where a ratio limit of $\zeta_{limit} = 0.2$ is used. Here, the cut is instated at the bin edge where this ratio ζ_{bin} exceeds or is exceeded by ζ_{limit}. The application of these cuts derived using different values of ζ is summarised in Table 4.2. Figure 4.8 shows, with the fine-tuned cuts, the evolution of the background rate over the 20 day long DAQ akin to Figure 4.6. The fine-tuned cuts result in a slightly better signal photon acceptance compared to the symmetric cuts, while the number of 1064 nm-like background photons remains the same. The application of these cuts

(symmetric and/or fine-tuned) to select 1064 nm photon pulses (and 1064 nm-like pulses) will be used again when the entire detector line is implemented and investigations into the total backgrounds of the TES will be conducted; which are expected be dominated by the extrinsic background pulses. The cuts, however, are bound to change with these new background pulses, and can serve as a major improvement over the more standard symmetric cuts.

ζ_{limit}	**Surviving Events**	**Dark Rate**, in 10^{-6} cps	**Signal photon acceptance**	**Significance**
0.3	10	$5.7^{+2.45}_{-1.3}$	87.86%	5.51
0.2	12	$6.9^{+2.62}_{-1.47}$	93.01%	5.24
0.1	16	$9.2^{+2.96}_{-1.77}$	97.85%	4.81

Tab. 4.2.: The ratio limits ζ_{limit} for varying values results in different fine-tuned cuts. These are applied to the datasets, for the fit parameters shown in Figure 4.7, and in Appendix B. For $\zeta_{limit} = 0.2$, this yields a dark rate $6.9 \cdot 10^{-6}$ cps with an acceptance $\sim 93\%$, which is compatible with the limit of $8.1 \cdot 10^{-6}$ cps and is an improvement over the symmetric cuts. The significance S is again calculated from Eq. (4.1) with a detection efficiency $\epsilon = 50\%$ for illustration.

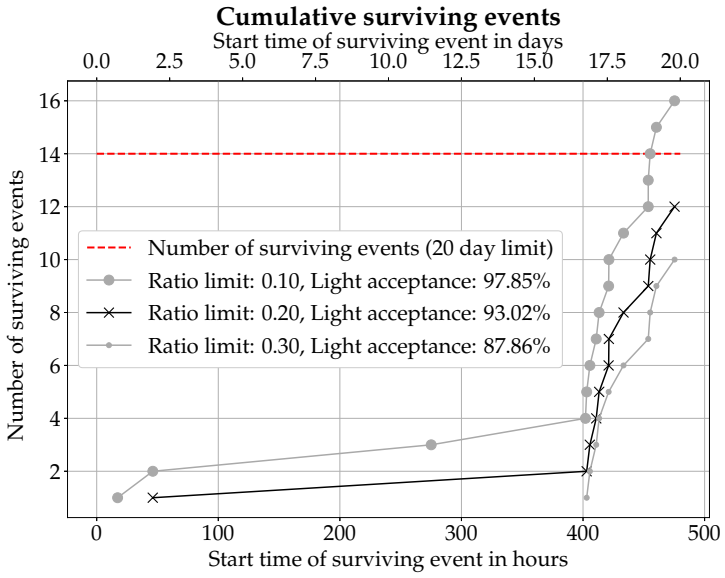

(a)

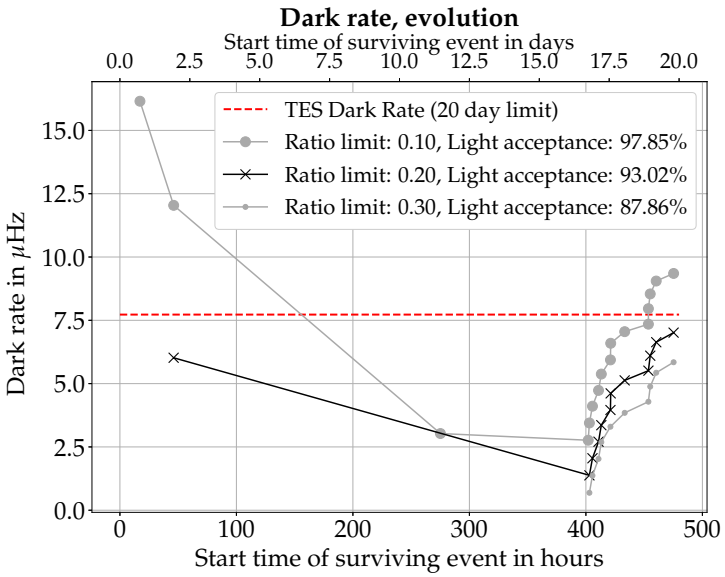

(b)

Fig. 4.8.: (a) shows the time each specific background event, which survives the fine-tuned cuts applied to it, was originally triggered in the 20 day DAQ period, akin to Figure 4.6. Again, with the cut used here 12 events were obtained over 20 days, lesser than the limit specified. The burst of photon-like events seen near the 400-hour mark is again noted, as in Figure 4.6, and is to be investigated. Using the fine-tuned cuts results in a slightly better signal photon acceptance compared to the symmetric cuts, while the number of 1064 nm-like background photons remains the same.

Parameter	**Cut**	**Symmetric Cut**, Lower limit	**Symmetric Cut**, Upper limit	**Fine-tuned Cut**, Lower limit	**Fine-Tuned Cut**, Upper limit
Pulse Integral [Vs]	Yes	$-2.29 \cdot 10^{-7}$	$-1.065 \cdot 10^{-7}$	$-2.27 \cdot 10^{-7}$	$-1.18 \cdot 10^{-7}$
Pulse Height, [V]	Yes	$-3.54 \cdot 10^{-2}$	$-2.25 \cdot 10^{-2}$	$-3.46 \cdot 10^{-2}$	$-2.35 \cdot 10^{-2}$
Decay Time, [s]	Yes	$2.409 \cdot 10^{-6}$	$6.295 \cdot 10^{-6}$	$2.68 \cdot 10^{-6}$	$6.52 \cdot 10^{-6}$
Rise Time, [s]	Yes	$1.087 \cdot 10^{-7}$	$5.13 \cdot 10^{-7}$	$1.64 \cdot 10^{-7}$	$6.02 \cdot 10^{-7}$
Amplitude, [V]	Yes	$1.35 \cdot 10^{-2}$	$2.43 \cdot 10^{-2}$	$1.39 \cdot 10^{-2}$	$2.47 \cdot 10^{-2}$
$\chi^2_{reduced}$	Yes	1.80	3.335	1.87	3.8

Tab. 4.3.: The fit parameters used to select pulses are shown in this table, along with the corresponding values for the cuts established on them. The values for the cut limits from the symmetric and fine-tuned cuts are both stated, to emphasise the fine-tuning aspect and the small deviations from the symmetric cuts. The fine-tuned cuts are for a ratio limit $\zeta = 0.2$.

4.3.2 Backgrounds & Working Points

The influence of different working points on the 1064 nm photon pulses has been described in Section 3.3. This also influences background pulses, and may lead to a

significant variation in the number of pulses in the TES. The influence of the TES working conditions on the background pulses, with the TES being either more or less susceptible to background pulses, needs to be investigated.
The choice of a working point where the number of (1064 nm-like) background pulses is minimal would be an ideal choice for the TES. To do this, the complete scenario of the TES backgrounds would be necessary after its implementation in the ALPS II experiment, such that the contribution of the extrinsic backgrounds is also considered. For now, we are restricted to investigate the impact of the intrinsic background pulses only. For this:

- The TES is operated for DAQ at a working point of $30\%R_N$, and the collected (triggered) background pulses are compared to a dataset of 1064 nm photons.
- This is expanded to analyse working points (WPs) $10\%R_N$ and $50\%R_N$ for intrinsic backgrounds triggered against a 24 hour DAQ period for comparison.
- These backgrounds will be directly analysed with 1064 nm pulse datasets for the same WPs. The resultant number of background pulses which remain after a pulse selection procedure is implemented will be of interest.
- The pulse selection procedure follows the symmetric cut approach mentioned earlier. However, due to the low statistics (only 24 hr DAQ periods) cuts are instated only on the pulse integrals, pulse heights and the (reduced) χ^2.
- For illustration, the cuts resulting in a $\sim 95\%$ 1064 nm photon 'light' acceptance will be used for comparison of the WPs (with respect to the number of surviving 1064 nm-like background pulses).

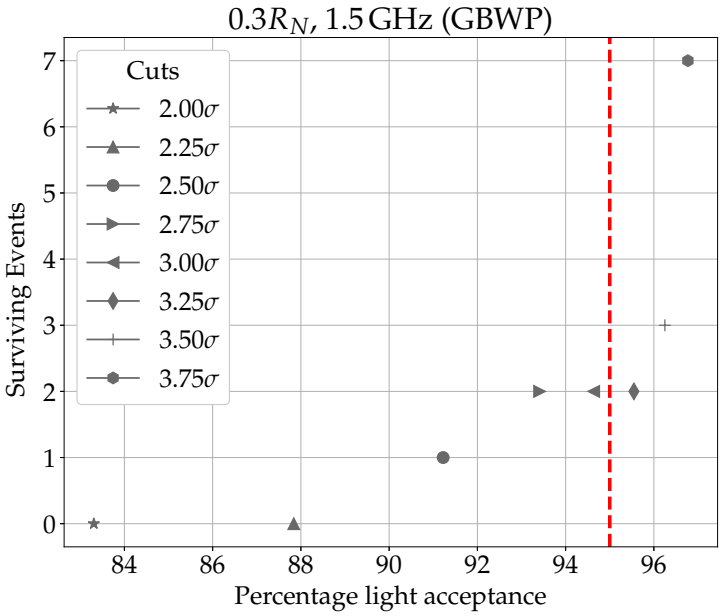

Fig. 4.9.: The 24 hr DAQ period for intrinsic background pulses collects 1410 triggers. With symmetric cuts on the pulse integrals, pulse heights and $\chi^2_{reduced}$, the background pulses remaining are shown above for a selection of cuts. For $\sim 95\%$ light acceptance, only 3 1064 nm-like pulses survive (example in Figure 4.11d).

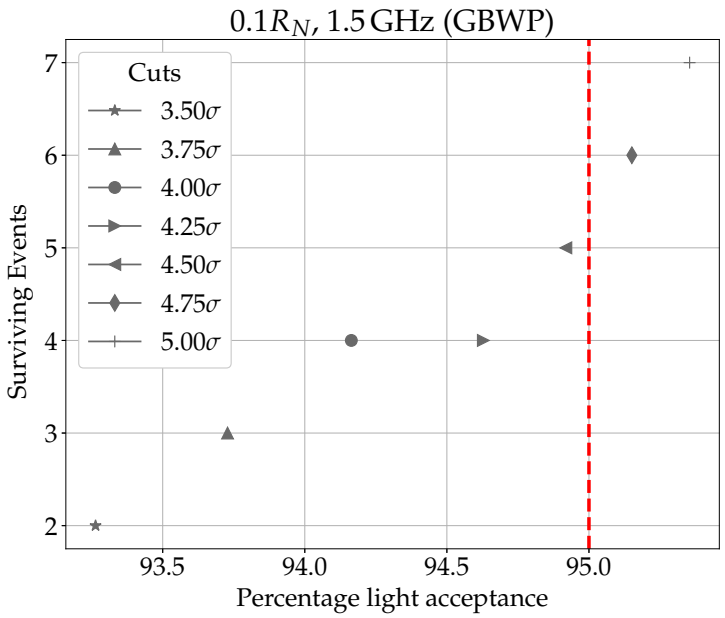

(a)

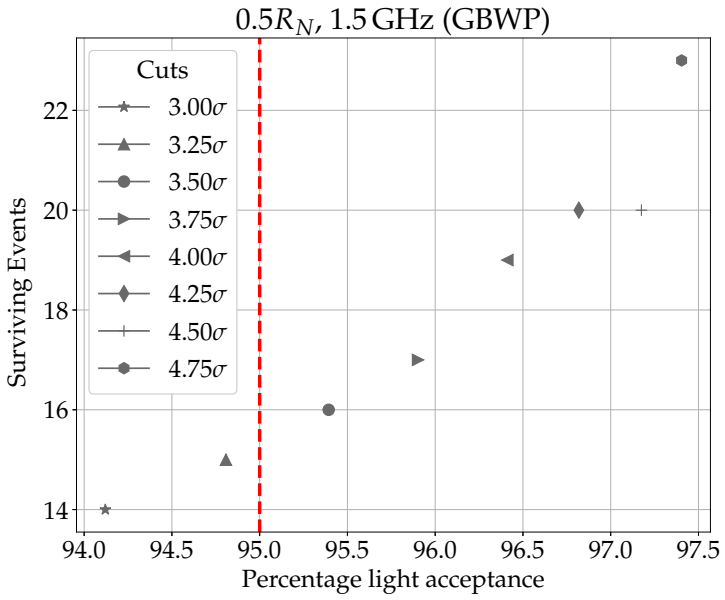

(b)

Fig. 4.10.: Similar to Figure 4.9, the 24 hr DAQ period for intrinsic background pulses for $10\%R_N$ and $50\%R_N$ is investigated. The DAQ collected 1842 triggers and 1703 triggers for the $10\%R_N$ and $50\%R_N$ WPS respectively. The remnant background pulses surviving the pulse selection are shown above in (a) and (b) for a selection of cuts. For $\sim 95\%$ light acceptance, only 4 1064 nm-like pulse survive (example in Figure 4.11b) for the $10\%R_N$ WP and 15 for the $50\%R_N$ WP (example in Figure 4.11f).

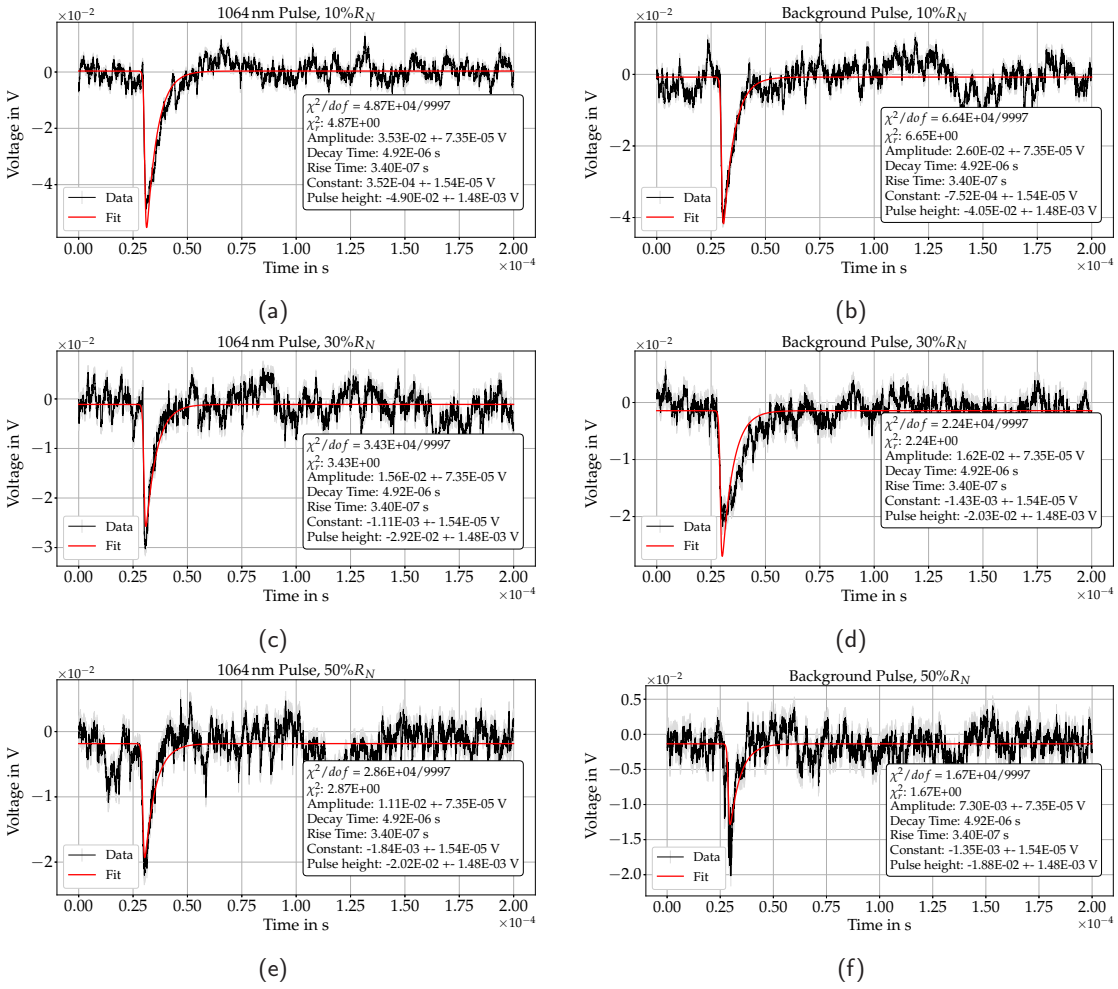

Fig. 4.11.: Exemplary 1064 nm photon pulses at the WPs $10\%, 30\%, 50\%R_N$ are shown in (a), (c) and (e). The corresponding intrinsic background pulses which remain after the (lenient) pulse selection procedure has been used are shown in (b), (d) and (f). The decrease in the pulse heights with increasing WPs is noted again, as well as the increasing influence of the electrical noise which can lead to a larger number of triggers being collected in the DAQ.

A single 24 hr DAQ period for intrinsic background pulses proves inconclusive regarding which WP would be best suited for TES operation. The background pulses surviving the cuts can (for WPs higher than $30\%R_N$) be easily further rejected with additional cuts on other fit parameters. However, the remnant background pulses are inadequate to draw any inferences from as $\lesssim 5$ pulses survive the cuts (with WPs $10\%R_N$ and $30\%R_N$).
In either case, this would provide only the best picture with respect to the intrinsic backgrounds, and not the extrinsic backgrounds which are expected to have higher statistics. Among other tests, this one also requires repeating as the choice of the

working point, as has been noted, can impact the TES pulse acquired and the (extrinsic) background pulses collected.

4.3.3 Setup Modifications

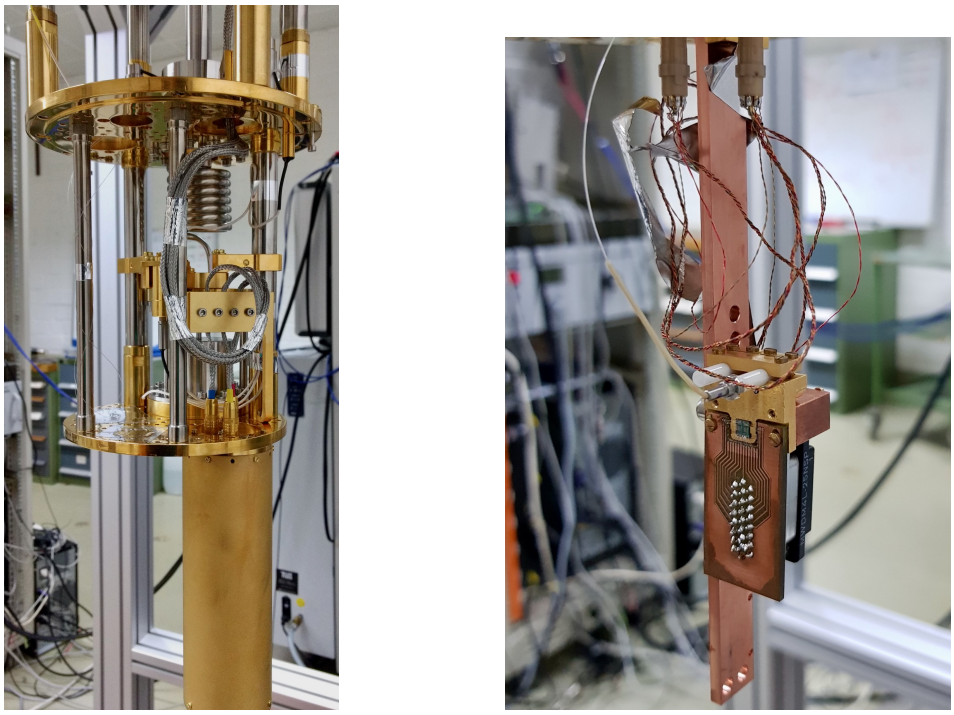

(a) (b)

Fig. 4.12.: The TES detector module on a copper cold finger, attached lengthways, is shown in (b). The TES chips (and stack) are within the white ferrules on the module, to which one optical fiber is connected. (b) shows the setup inside (a), enclosed within the gold-plated aluminium can, which is connected (as is the cold finger) to the coldest stage in the cryostat. The thermalised wiring above this stage is connected from the SQUIDs on the detector module to the SQUID electronics.

In the setup discussed so far, the TES detector module was:

- Mounted on a copper 'cold' finger attached to the coldest stage (achieving a temperature $\leq 25\,\mathrm{mK}$) of the cryostat.
- This was in turn enclosed in a gold-plated aluminium can also attached to the coldest stage of the cryostat, to serve as an additional thermal and electromagnetic shield and provide mechanical protection (Figure 4.12a).

- The TES detector was mounted in such a way that the TES chip (and the white ferrules atop them) were facing the inner wall of the aluminium can (Figure 4.12b).

The utility of this setup was found lacking as it did not leave enough room for the adequate attachment of an optical fiber to the TES (via the white ferrules), requiring a redesign and enlargement of the aluminium can. For additional thermalisation of the detector module, a new cold finger was also designed to be used for this updated setup (Figure 4.13a), where the detector module can be mounted facing the ceiling ('upwards' instead of 'sideways' as before), seen in Figure 4.13b.

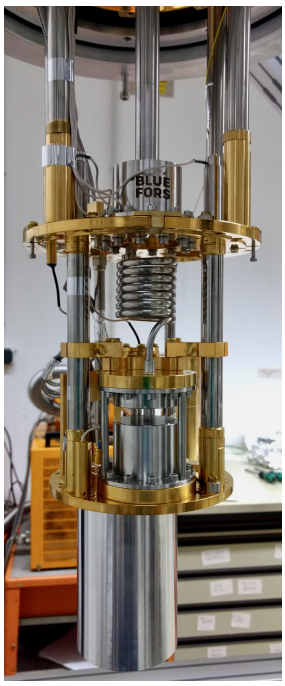

(a)

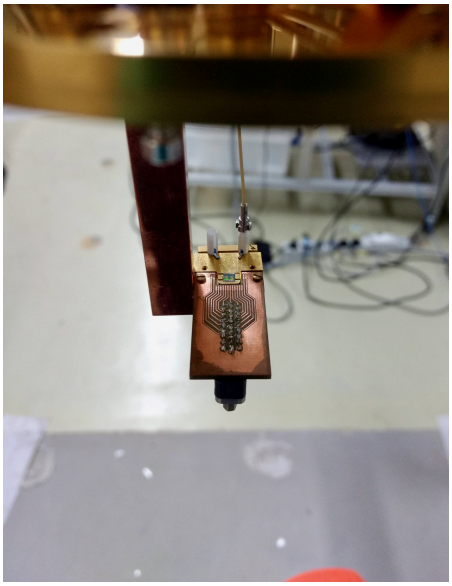

(b)

Fig. 4.13.: (a) shows this setup enclosed in the wider, redesigned aluminium can. This too is attached to the the coldest stage of the cryostat, along with the copper finger. The modified setup in which the TES detector module is attached facing 'upwards' on a redesigned, thicker copper cold finger is shown in (b). An optical fiber is connected to one of the white ferrules as in Figure 4.12b but the additional SQUID output wires are disconnected.

This was the main point of difference from the previous setup where such a position could not be achieved. This is expected to help as it involved minimal bending of the attached optical fiber (albeit only in the final setup, and not for acquiring intrinsic background pulses) but can lead to increased exposure of the detector module to background pulses accrued due to cosmic rays. This has yet to be investigated and is being tested with

simulation strategies. The intrinsic background pulses for this modified setup need to be investigated, as with the previous setup.
Following the same data taking period of 20 days, a similar (symmetric cut) pulse selection procedure can then be applied to this dataset (Figure 4.14). These cuts are derived from a sample of ~ 9000 1064 nm photon pulses collected from the TES in this setup.

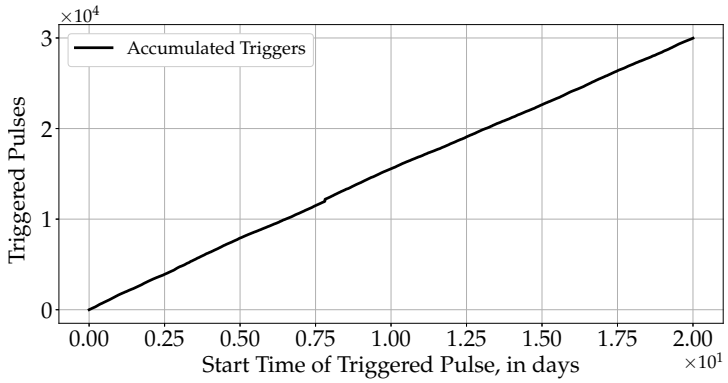

Fig. 4.14.: The 20 day long DAQ for intrinsic background pulses in the modified setup. About 30,000 pulses are collected, a raw trigger rate of $1.73 \cdot 10^{-2}$ cps.

The remnant background events are shown in Figure 4.15, where the cuts result in ≥ 60 1064 nm-like background events. The corresponding dark rate ($\sim 40 \cdot 10^{-6}$ cps) also slightly exceeds the limit required by the TES experiment ($\sim 8.1 \cdot 10^{-6}$ cps) but (considering Eq.1.13) the sensitivity scales as $\sqrt[1/8]{DC}$ so this does not prove to be a roadblock. The excess background events could be from an increase in exposure to cosmic rays or due to a change in the setup itself.

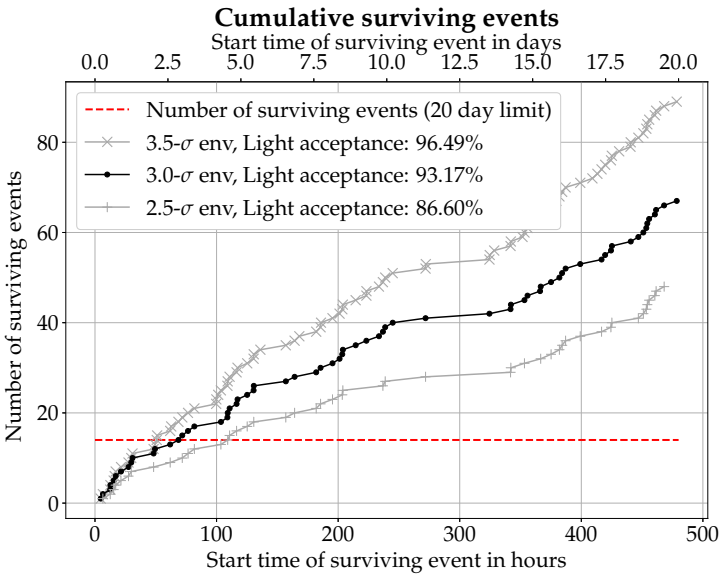

(a)

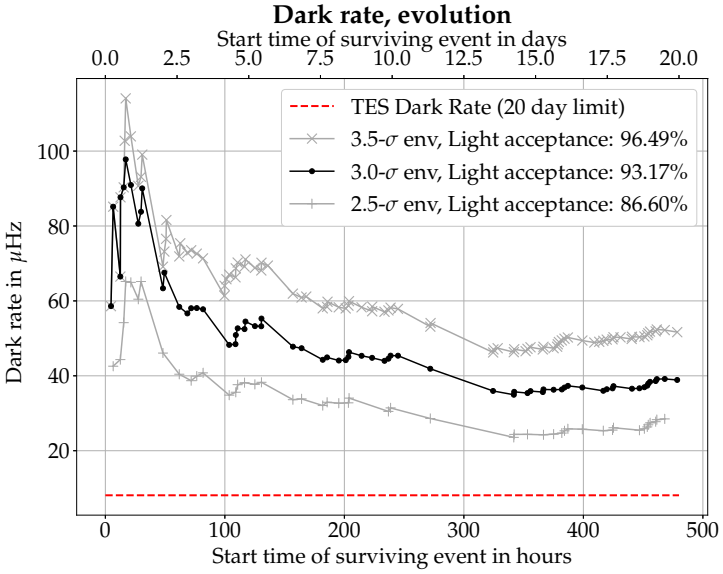

(b)

Fig. 4.15.: With the same approach as in Figure 4.6, surviving background events are plotted in (a) against the time they were originally triggered. The $\mu \pm n \cdot \sigma$ cuts are applied to it, resulting in ≥ 60 1064 nm-like background events which remain after the cuts at $n = 3$ are used. This exceeds the limit of 14 background events over 20 days. The corresponding evolution of the dark rate is shown in (b), where the final dark rate ($\sim 40 \cdot 10^{-6}$ cps) also slightly exceeds the limit required by the TES experiment ($\sim 8.1 \cdot 10^{-6}$ cps). This increase in the number of irreducible backgrounds could be due the increase in exposure to cosmic rays or due to a change in the setup itself, but does not prove to be a showstopper (considering Eq.1.13), the sensitivity scales as $\sqrt[1/8]{DC}$.

4.3.4 Viability for ALPS II

Implementing the TES detection scheme in the ALPS II experiment requires (among other things) the successful detection of single 1064 nm photons with a corresponding dark rate lower than $8.101 \cdot 10^{-6}$ cps. With the selection procedure(s) laid out previously, this limit can be met with a intrinsic background count of 12 pulses (indistinguishable from a single 1064 nm photon pulse) over 20 days, amounting to a dark rate $6.9 \cdot 10^{-6}$ cps.

With the unmodified setup described in the previous section, and pertaining only to the intrinsic background events, the TES is viable for use in the ALPS II experiment (Figures 4.6 and 4.8) with the analysis conditions laid out in Table 4.1. Further tests and checks, such as those for efficiency and with extrinsic backgrounds notwithstanding, the usability of the TES as a single photon detector for a ultra-low background, ultra-low signal rate experiment can be further investigated and invested in. Further:

- The TES and all the different components used to operate it, such as the cryostat and the attachment pieces (examples in Figures 4.13b and 4.12b) are not manufactured to be highly radiopure (or with expressly radiopure materials, in a radiopure environment). A low background level with respect to 1064 nm photons can nonetheless be achieved.
- This low rate is also obtained using a straightforward pulse selection approach, and without any added vetoes or selection mechanisms working in tandem with the DAQ. These, of course, can be adopted in the future should tests with backgrounds necessitate it. Other more sophisticated approaches (such as machine learning applications, discussed in Appendix D) have not yet shown any improvement yet over this approach.

4.4 Detection Efficiency

The previous sections have shown that while the intrinsic background rate in the TES for 1064 nm photons is $\mathcal{O}(10^{-6})$ cps, the full utility of the TES is derived only from a fiber-coupled setup. For the full description of the background events (and sources) that the TES system contends with (i.e. the extrinsic background events), knowing the efficiency of the fiber-coupled setup is essential. Such a fiber-coupled TES setup has been shown to achieve detection efficiencies of 95% [110], and 87% [111]; the latter with a similar TES microchip.

The goal of our TES setup is to measure ∼50 photons (for a 5σ detection confidence) over 20 days with a detection efficiency of 50%. A higher detection efficiency would mean a shorter time window to reach 5σ confidence. While the TES chip itself has a high quantum efficiency of ∼99% ([93, 112]), there are other areas where a loss in the final efficiency can (and will) be incurred. Here, the TES or TES chip refers to the TES stack (as described in Section 2.4.2). These are taken into account and split into two broad categories:

- **(Raw) System Detection Efficiency (SDE)**: Any efficiency loss incurred in the main line of the fiber-coupled system, for the direct measurement of 1064 nm photons, is accounted for here. This includes any losses possible due to:
  1. The innate quantum efficiency of the TES
  2. The alignment of the optical fiber to the TES
  3. The losses due to the fiber length and splices and in the fiber feedthrough to the cryostat
  4. The efficiency of the pulse analysis algorithm to correctly select 1064 nm photons (seen in Section 4.3.1)
  5. The coupling of the optical fiber to the ALPS central optical bench (COB)[4]
- **Additional Components:** Any efficiency loss added to the main line of the fiber coupled TES, such as the addition of any additional component or features, is accounted for here. These include, but are not limited, to:

[4]The design of the final COB for the TES is yet to be finalised.

1. A filtering system for non-1064 nm photons, based on fiber-to-free space couplers (Filter bench scheme, in the cryostat, described further in Section 4.5)

2. Fiber curling to suppress the transmission of photons with wavelengths $\geq$ 1064 nm.

The aforementioned methods are implemented to contend with extrinsic background pulses expected in the detection system, and will be discussed in the following section.

Setup Design

The measurement of the SDE (without the COB) is designed to be done following a scheme adapted from [113]. A photon source (a 1064 nm laser) is used to make a reference power measurement and consecutively send photons to the TES. This reference measurement will be made to know the power i.e. number of photons sent to the TES, and will be compared to the number of photons seen in the TES signal (from the DAQ scheme).
This presents some challenges as the TES is a highly sensitive microcalorimeter which can easily be overwhelmed by the simultaneous incidence of multiple photons. The number of incident 1064 nm photons thus cannot exceed $\mathcal{O}(10^5)$ cps[5], in order to ensure a proper detection of the photons and successfully count them, while also not driving the TES out of its dynamic range. This corresponds to a power (incident on the detector) of $\leq \mathcal{O}(10)$ fW. The basic outline of this setup is depicted pictorially in Figure 4.16. Salient features of this are described below:

- The attenuated output of the 1064 nm laser is split using a 99:1 beamsplitter, with $\sim$99% of the power used to make a reference measurement with the calibrated power meter.

- The remaining power is further attenuated and split into two optical fibers (with a 50:50 beamsplitter) connected then directly to the two TESs in the cryostat via fiber feedthroughs.

[5]Estimating a decay time constant of $5\,\mu$s for single 1064 nm photons in the TES, and a negligible rise time constant.

- The attenuation is measured before each calculation, as well as the transmission of the fiber feedthroughs themselves. Polarisation maintaining mating sleeves are used wherever possible.

The 1064 nm single photons thus triggered in the DAQ scheme can be used to estimate the efficiency of the TES setup. The efficiency (SDE) can then be given by:

$$SDE = \frac{P_{TES}}{A \cdot P_{ref}}, \tag{4.4}$$

where P_{TES} is the power registered in the TES via the number of incident photons, A is the calibrated attenuation, and P_{ref} is the reference power measurement, from the 99% output of the first beamsplitter. The reference measurement is made using a dedicated power meter calibrated by the PTB, which is sensitive to the ultra-low power levels ($\mathcal{O}(10)$ pW) required. The fiber splitters and attenuators in the optical fiber lines, to the power meter and to the TES, will require an in-situ calibration before each measurement. Another efficiency measurement setup, described in [111] but not currently realised or planned, includes the use of a pulsed laser source and largely precludes the need for explicit photon counting currently planned. Other strategies for the same are under discussion as well, with the use of a separate heterodyne system in conjunction with the TES system or from a purely statistical standpoint by calculating possible pile-up events with the monochromatic 1064 nm laser.

4.4.1 Measurement and Challenges

Calibrating the attenuation depends on the dynamic range of the calibrated power meter, and leads to a reliable measurement of the attenuation to a value ∼500-1000. The lowest possible power for P_{ref} (as measured, again, at the power meter, of $\mathcal{O}(1)$ pW) serves as an input to this attenuation line. The power introduced thus to the optical fiber (via a mating sleeve) coupled to the TES is $\mathcal{O}(10)$ fW. This estimates a photon flux of ∼100,000 per second at the TES. Using Eq. 4.4, the corresponding SDE for each TES chip can be calculated. This first measurement results in an SDE of at least 5% for the TESs.
This preliminary test was performed with non-optimal fibers connected the TESs, lacking an anti-reflection coating on each fiber tip. These were also suspected to be improperly aligned to the TESs, which could themselves be obstructed due to dust or dirt collected on them. The measurement, due to the use of optical fibers and mating sleeves, has larger uncertainty as well. These challenges are being mitigated by using the correct

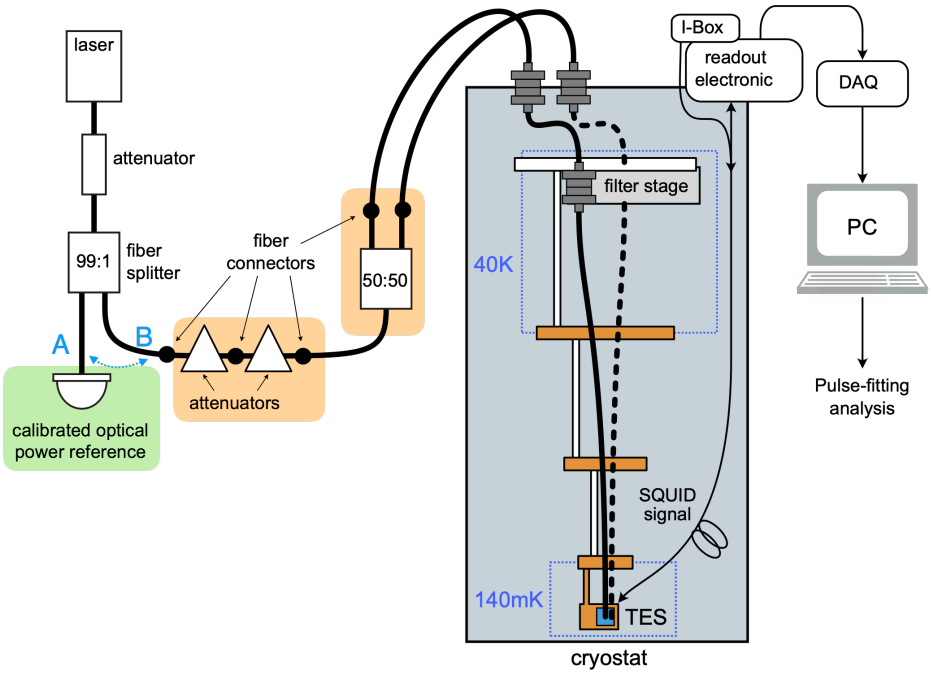

Fig. 4.16.: The experimental setup to measure the efficiency of the fiber-coupled TESs in the detector module is represented here pictorially. The filter stage also shown above is currently bypassed and is not featured in the main line of the TES itself, and will be included after further optimisation tests are concluded. Figure and setup from Katharina-Sophie Isleif.

fiber tips on the TESs and planning spliced connections wherever possible. Other sources of uncertainty also include a Poissonian (statistical error) on the number of photons triggered from the TESs and voltage measurements from uncalibrated oscilloscopes, which is also being investigated. Nonetheless, this preliminary efficiency measurement has already shown that this approach is viable and needs to be optimised.

4.5 Extrinsic Backgrounds

From the two broad background pulse categories established in Section 4.2, the influence of the intrinsic background pulses on the dark rate (for 1064 nm photons) is seen in Section 4.3. With an optimal detection efficiency, estimating the influence of the extrinsic background pulses when the optical fiber is connected to the TES can also be done.
In the DAQ scheme, a background pulse is triggered from the TES only when a voltage threshold of -20 mV is surpassed. For the intrinsic background pulses, this lead to a

rate of $\mathcal{O}(10^{-2})$ cps (Section 4.3, Figure 4.2a) before any pulse selection procedure was implemented. Similarly, estimating the extrinsic background pulses triggered in the modified setup described in Section 4.3.3, a (raw) trigger rate of $2.3 \cdot 10^{-2}$ cps is achieved over a period of 2.5 days (Figure 4.17). This short test run was performed to estimate the influence of just connecting the optical fiber to the TES.

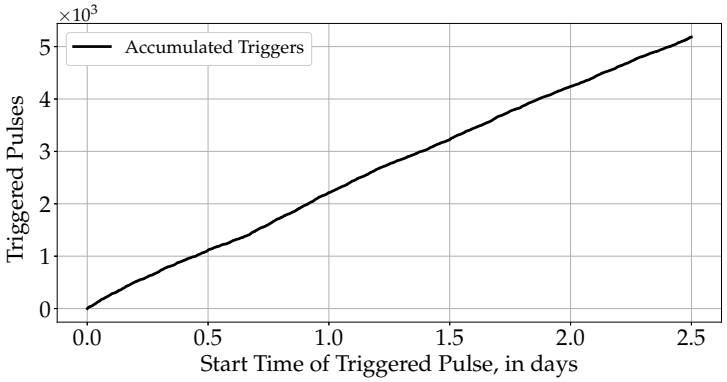

Fig. 4.17.: The background pulses collected once the optical fiber is connected to the TES, over a period of 2.5 days, is shown above. Approx. 5,000 pulses are collected. This can be compared directly to the intrinsic background pulses collected in Figure 4.14, which also counts a trigger rate $\sim 2 \cdot 10^{-2}$ cps.

The raw trigger rate, without any pulse selection procedure, is mostly the same as the one from the intrinsic background pulses (for the same setup) seen in Figure 4.14. This is explained by the low detection efficiency with the optical fiber connected to the TES chip. Running the pulse selection procedure, we obtain similar results (albeit only over the 2.5 day period) to those in Figure 4.15, these are shown in Figure 4.18.

After the planned optimisation of the detector efficiency, with its myriad challenges, the extrinsic backgrounds can be better understood. However, the main contributors to this can already be shortlisted and are suspected to be photons originating from blackbody radiation [114].

Blackbody Radiation

The extrinsic backgrounds can be dominated by the photons from blackbody radiation (BBR) from the optical fiber, coupling into it from its environment. This optical fiber was not connected to the TES previously (i.e. for the intrinsics). The background pulses can be detected in the TES due to direct 1064 nm photons or due to pile-ups of multiple

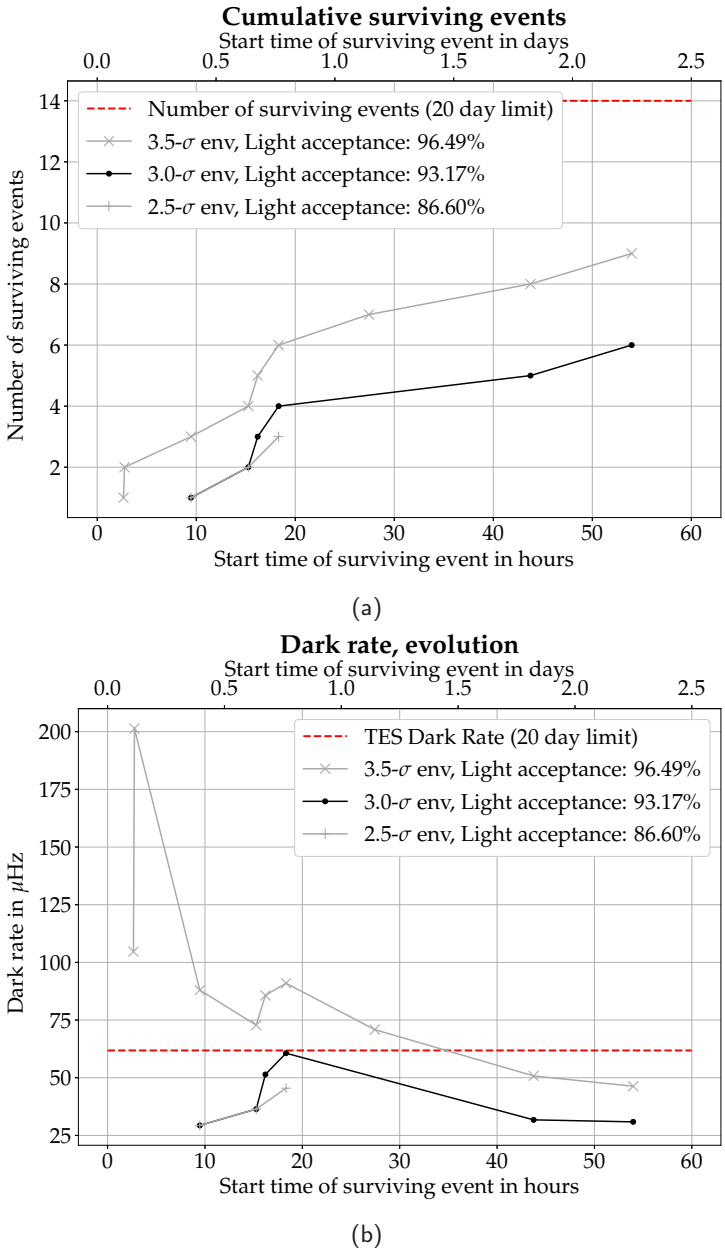

Fig. 4.18.: With the same approach as in Figure 4.6 and 4.15, the surviving background events are plotted in (a) against the time they were originally triggered. (b) shows the corresponding dark rate achieved due to the surviving background pulses, and seems to follow a similar trend as in Figure 4.15. The pulse selection is based on the same 1064 nm photon sample, and the DAQ and the readout settings remain the same as they are for the intrinsic background pulse collection.

photons. As the optical fiber will be entering the cryostat from a room temperature environment, the background pulses due to these photons (referred to hence as BBR

photons) is non-negligible. The rates at which direct 1064 nm (BBR) photons can be incident on the TES are $\mathcal{O}(10^{-2})$ cps considering an energy resolution of 10%. These are heavily influenced by the temperature at the warm and 'open' end of the optical fiber in the lab environment, where a decrease of 10 K in this temperature can reduce the rate by an order of magnitude. A higher energy resolution for 1064 nm photons can also reduce this rate by 2 or more orders of magnitude (Figure 4.19), by increasing the discrimination power of the detection system.

In order to ensure that the TES is not blackbody-background limited, the realisation of the detector setup will include some strategies to mitigate or discriminate these backgrounds (from 1064 nm photon signals):

- **Mitigation**

  Filtering:
  To cull the number of BBR photons, a filtering setup (Figure 4.20) has been previously designed and is being tested currently. This will be an in-cold setup installed within the cryostat, with a narrow bandpass filter for 1064 nm. As a consequence of the design, the efficiency of this bench (with the filter) is expected to be $\leq 80\%$ due to the fiber to free-space coupling involved twice over. The setup of this is described in [115].
  This can mitigate the number of backgrounds that could possibly be triggered due to the pile-ups caused by BBR photons. The filter bench will be used to essentially only transmit 1064 nm photons with narrowband filtering. The use of these filters can also impact the efficiency of the full line. The filter peak can also shift due to temperature changes [116].
  The implementation of this bench is also challenging due the optimisation of the couplers involved so as to achieve the highest possible transmission through them. Special care and work is involved to use the bench. The operation of the bench under the ultra-high vacuum of the cryostat and at a temperature of $\sim$40 K will also reduce its transmission (due to misalignments in the cold environment), affecting its efficiency [115].

  Fiber Curling:
  To suppress the photons with wavelengths differing from those of the 1064 nm photons, the curling of the optical fiber can be used. This phenomenon of macrobending of optical fibers leading to mode-deformation is described in [117] and

[118]. The bending losses have been shown to efficiently suppress these less energetic photons with very negligible losses to the transmission of the 1064 nm signal photons. This is shown in Figure 4.21, where multiple loops of different radii are used to measure the transmission of two wavelengths. Increasing number of loops with larger radii suppress 'signal' 1062 nm photons negligibly for multiple loops of radii larger than 17 mm while the transmission drops rapidly for 1550 nm photons beyond this radius. A section of the optical fiber will be looped and installed in the cryostat before attaching to the TES.
This curling has only been tested thus far for 1550 nm and will need to be confirmed for other higher wavelengths. Suppressing these larger-wavelength photons can reduce their contribution to the pile-up events seen at the TES eventually.

- **Discrimination**

  Pulse Processing: The other aspect of dealing with these backgrounds is the use of the pulse selection procedure, which has been outlined in previous sections. With a high discriminating power, i.e. higher energy resolution, we can better distinguish among photons with differing energy. This approach rests more on pulse processing and while we have seen differing energy resolutions with various pulse processing/fitting techniques (Figure 3.1), it has also been demonstrated that the energy resolution of the TES is electrical noise-limited[6].

[6]Simulation of the electrical noise in the TES added to theoretically ideal TES pulses lead to the observed energy resolutions. Result from José Alejandro Rubiera Gimeno, Internal Communication.

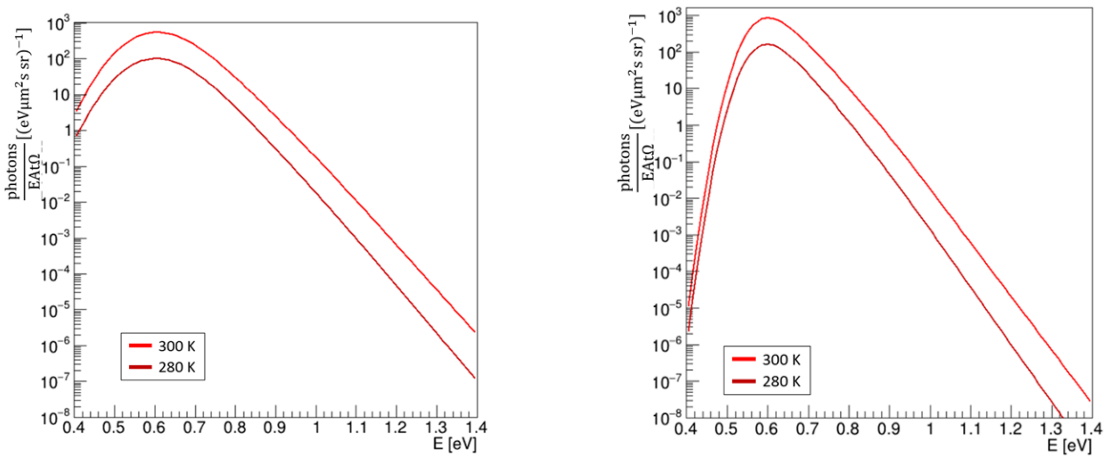

(a) (b)

Fig. 4.19.: (a) and (b) show the simulated spectra of the blackbody photons modelled with a TES energy resolution ($\Delta E/E$) of 10% and 5% respectively. These have taken into account the features of the TES with respect to incident photon reflection, etc. The two temperatures considered here are the temperatures of one end of the optical fiber which is in the lab at approximately room temperature, to estimate its influence. Considering other setup features such as the solid angle and and area of the optical fiber opening on the TES chip, the rate of photons is estimated $\mathcal{O}(10^{-3}, 10^{-4})$ cps. Figures from José Alejandro Rubiera Gimeno.

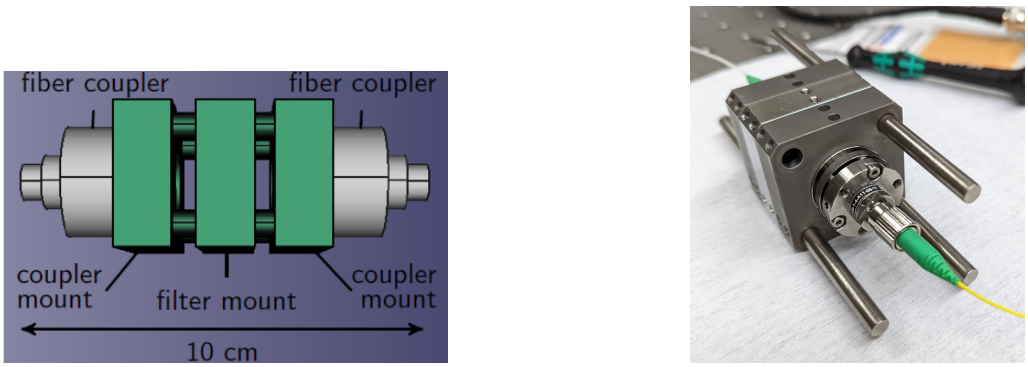

(a) (b)

Fig. 4.20.: The schematic of the filter bench [120], in (a), shows its constituent parts: three titanium mounting plates (green) and two fiber couplers. The fiber couplers are made of amagnetic titanium. These couplers are each placed on a mount, whereas the filter itself can be inserted into the filter mount in the middle. The whole setup is held in place by four metal rods. Titanium has been chosen due to its comparable thermal expansion coefficient to glass (in the filters) for minimal relative shrinkage for operation in the cryostat. (b) shows the realisation of this scheme with the fiber couplers and the optical fiber. This will be further mounted on a bracket, attached in turn to the 40 K stage of the cryostat.

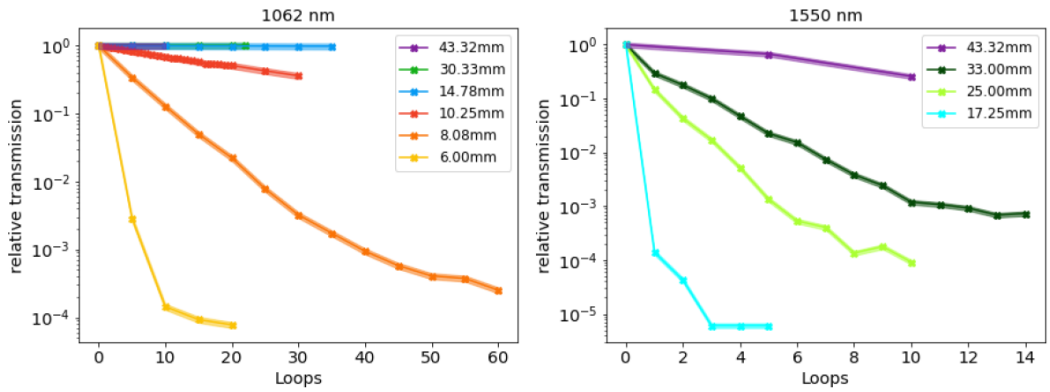

Fig. 4.21.: For the wavelengths 1062 nm and 1550 nm, the fiber curling method was tested to estimate the relative transmission through the windings. Increasing number of loops or windings of larger radii (bending radius of the HI1060 fiber used is ∼15 mm) are used. Figure from [119].

The direct 1064 nm BBR photons could comprise an irreducible background that mitigation and discrimination techniques will not be effective against. However, the reduction in the temperature of the optical fiber's opening environment by even 20 K already reduces the final trigger rate of the direct BBR photons by 2 orders of magnitude. The utilisation of such a setup is yet to be investigated and implemented. The contribution of the BBR photons to pile-ups is also $\mathcal{O}(10^{-3})$ cps primarily from the pile-up of two photons of approximately 0.5 eV. The filtering and suppression of these higher wavelengths is aimed at alleviating backgrounds from these pile-ups.

The discussion of these filtering and selection techniques is heavily linked to the overall detection efficiency. While the fiber curling does not suppress signal photons (1064 nm) it has yet to be tested for wavelengths higher than 1550 nm and for a longer term in the cold cryostat. All tests conducted thus far have shown that the mechanical hardness and the transmission of the optical fiber under curling are unhampered from exposure to cryogenic temperatures. A filter bench setup, with its limited transmission, and pulse discrimination approach, with its strict selection, can impact the overall efficiency of the TES line but benefit with respect to background suppression.

5 Conclusion

A cryogenic superconducting detector, the transition edge sensor (TES), can be a viable option for use in ALPS II. This low background detector, read out with SQUIDs, is housed in a cryogenic environment provided by a dilution refrigerator capable of stable long term operation at temperatures < 25 mK. The sensor module from PTB has tungsten TESs designed and manufactured by NIST, and SQUIDs manufactured by PTB. This is mounted in the cryostat and operated with dedicated SQUID electronics. With the I-V characteristic of the TES and stable settings for the SQUIDs, a suitable working point for the TES (and SQUIDs) is found. The analysis of triggered 1064 nm pulses in the TES is carried out, at these working settings, with a multitude of pulse fitting schemes. These are tested to achieve the best possible characterisation of the TES pulses. The robust Free fit scheme serves this purpose best; with multiple fit parameters assimilating the most information about the TES pulses. These fit parameters are also used for pulse selection. A principal component analysis (PCA) approach is also tested in this regard, but does not perform as well, save as a method for de-noising pulses. With these characterisation schemes, an energy resolution $\Delta E/E$ of 7-12% can be achieved depending on the approach used.

The backgrounds seen in the TES are broadly divided into two categories: extrinsic and intrinsic backgrounds. These are pulses recorded in the TES when no signal are is to them, and depending on whether an optical fiber is connected to the TES or not respectively. These backgrounds need to be investigated, following a phenomenological approach, to confirm the viability of the TES for use in ALPS II. For this, over a 20 day period, an upper limit of $8.1 \cdot 10^{-6}$ cps on the dark count rate is required (with other assumptions), for a detection system. This is tested for the intrinsic backgrounds, which are collected over this period and subjected to a pulse selection algorithm based on the fit parameters derived from the signal 1064 nm photons. This discrimination is implemented using cuts dictated by the distributions of the fit parameters, which can also be further fine-tuned. The resultant low background rate achieved $6.9^{+2.62}_{-1.47} \cdot 10^{-6}$ cps shows the viability of a native TES setup for ALPS II, pending tests for the extrinsic backgrounds. Setup modifications required yielded a marginally higher background rate ($\sim 40 \cdot 10^{-6}$ cps) due to a change in the sensor module orientation. For all the selection procedures, these

ensure that $>$ 90% of the original 1064 nm signal photons are retained when the cuts are applied to the signal dataset.

With the connection of the optical fiber to the TES, the extrinsic background pulses are also detected. These are expected to be dominated by blackbody radiation. Prior to this, the efficiency of the detection setup must first be ascertained, to optimise in particular the efficiency of the fiber-to-TES coupling. A test for this has been set up, using a specially calibrated power meter to work with the extremely power levels required. A preliminary run of this test measured an efficiency of about 5% in either TES of the detector module. Before other investigations, the efficiency needs to be optimised. Other losses along the detector line are also expected, from the filter bench and fiber curling. This will be an in-cold system to filter out photons (from blackbody radiation) in the optical fiber to the TES which can cause pile-up background events. The filter bench, and the fiber curling tests, are important for the reduction of these extrinsic backgrounds and have shown promising results. These will also need to be aided by improvements in the pulse selection procedure by making it more stringent, or working with other strategies such as machine learning.

Understanding the response of the TES to photons of different energies is important to confirm the nature of the extrinsic backgrounds. The lower end of these energies that can be reliably detected in the TES is an important feature also for the realisation of other physics goals, which require also a low energy detection system with low (or next to no) background events. This works to create a full understanding of the TES backgrounds seen thus far as well, which will include simulations for the backgrounds, accounting for the TES design and general setup.
All these needs lay the basis for the next investigations:

- Optimising the efficiency of the detection setup.
- Determining the background rate due to the extrinsic background events, and the mitigation strategies to reduce them, such that the fiber couples TES is ready for use in ALPS II.
- Understanding the sources of the TES's backgrounds and simulating them in the TES module.
- Modifying and/or redesigning the TES module itself to better fit other physics goals, such as a direct dark matter search.

These are also steps taken in addition to the final move of the detector and cryostat to the experimental hall in HERA (North), DESY, in a new TES Room. The characterisation of the TES achieved thus far will be repeated there, in its final environment, where the backgrounds and efficiency of the TES will be retested. The TES detector line will then connected to ALPS II for data taking in 2023.

Appendices

Dilution refrigeration

A

Principle

Dilution refrigeration systems are one of the only methods to supply continuous cooling power to a system at temperatures below $\mathcal{O}(100)$ mK. The final temperatures achieved also have no theoretical minima and can reach values below 10 mK. Using dilution refrigerators (henceforth called DRs) also does not involve any moving parts in the low-temperature stages. They are typically easier to operate, especially long-term, than an adiabatic demagnetisation refrigerator, which was used in a previous iteration of this setup described in [69]. Successful commercial DRs have been available since the 1970s [121], able to cool down to temperatures below 10 mK. For most setups, these DRs have replaced the adiabatic demagnetisation refrigerators (which used paramagnetic salts). Following [122] and [121] (other comprehensive textbooks and reviews also exist, such as [123]), the working of DRs is sketched out below.
The principle of dilution refrigeration is a consequence of distinctive features exhibited by a mixture of ^{3}He and ^{4}He, at sufficiently low temperatures. First proposed by London in 1951 and by London, Clarke, Mendoza in 1962 [124], successful prototypes reaching a temperature of 0.22 K were already operating by the 1960s. Subsequent developments have pushed this technology further.

For temperatures below $\sim$1 K, a mixture containing ^{3}He and ^{4}He will spontaneously separate into two marked phases: one phase is dominated by ^{3}He and one by ^{4}He (Figure A.1). For temperatures below about 40 mK, one phase is practically pure ^{3}He and the other, dilute phase is made of 6.4% ^{3}He and 93.6% ^{4}He. The possibility to dissolve 6.4% ^{3}He in liquid ^{4}He even at absolute zero is of essential importance to the success of the DR.
^{4}He undergoes a transition at temperatures below 2.17 K from normal fluid to superfluid, and 'contamination' of this with ^{3}He leads to decreasing superfluid transition temperature. The enthalpy of ^{3}He in the ^{3}He-dilute phase is larger than that in the ^{3}He-concentrated phase. Thus, the mixing of the ^{3}He atoms into the dilute phase is an endothermic process, and cools its environment down even at mK-level temperatures. This cooling happens in

a container called the mixing chamber, and the process is made continuous by pumping ^{3}He into the line and pumping the ^{3}He-vapour out.

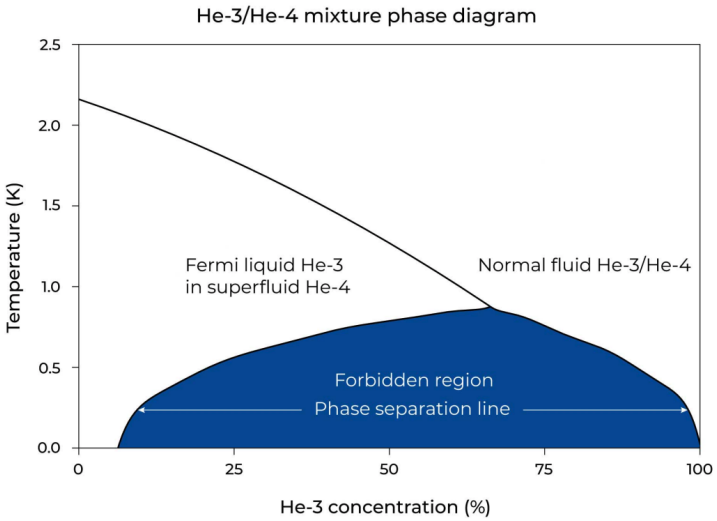

Fig. A.1.: The phase diagram for a ^{3}He-^{4}He mixture, which separates into two phases at temperatures < 0.8 K. As the temperature decreases further, one phase gets more and more concentrated (almost purely) in ^{3}He, while the other in ^{4}He, with some ^{3}He. Figure from BlueFors LD250 operation manual.

Dilution Cycle

The cycle of cooling the refrigerator and setup is discussed here, in particular with respect to the DR used. For our setup, this is the SD250 system from BlueFors. The full dilution cycle is started by cooling the refrigerator down to the requisite temperature using a pulse tube. These are variations of a Stirling or Gifford-McMahon refrigerators, with an oscillating piston and helium as the working gas to cool systems down [125]. The added advantage is that they have no moving parts at the cold end. The Helium-mixture is pumped in, cooled to a temperature < 4.2 K using various heat exchangers. It condenses to some extent and is pumped through the internal system. The dilution cycle is done in this internal or dilution unit of the cryostat, shown in Figure A.2. This condensed mixture fills up the still (only partially) and mixing chambers, and the condensing lines. Starting the pumping procedure on the still chamber initiates the evaporative cooling and reduces the temperature; below 0.8 K the dilution refrigeration is started as the phases separate.

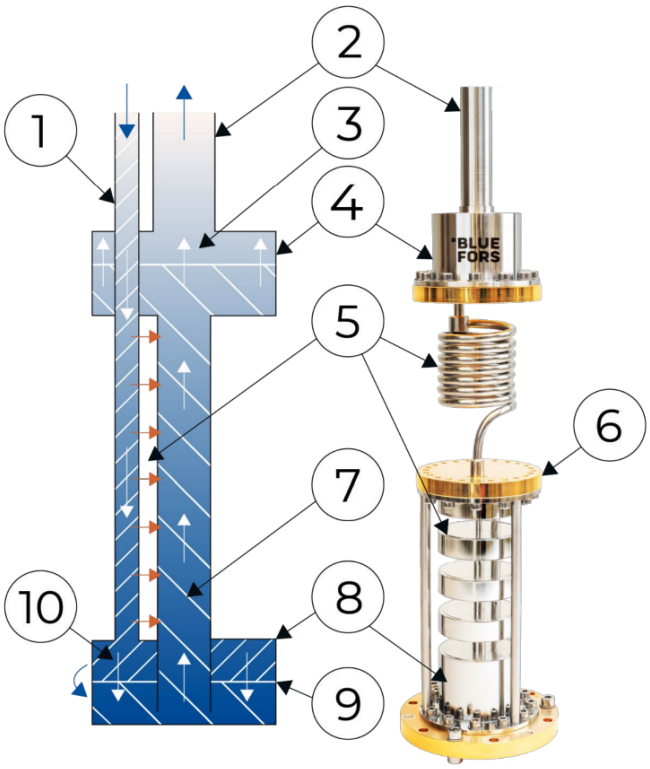

Fig. A.2.: The parts of the dilution cycle, in the internal unit, are shown above. (1) and (2) are the condensing and still lines respectively, which pump in and out the He-mixture (predominantly ^{3}He, over time). (3) is this ^{3}He-rich phase, in the still chamber (4) which reaches a temperature of 1.1 K. (5) is the heat exchanger winding which pre-cools the mixture coming in to the mixing chamber in (8) past the cold plate (6). Here the phases of the mixture which are separated by the schematic boundary (9) mix again. The ^{3}He-rich phase in (10), after mixing, is pumped out in (7). The cooling is achieved in the mixing chamber, and the attached thermalisation plate reaches the low temperatures of $\sim$20 mK. This continuous operation, with evaporative cooling, is achieved by the pumping of the still line. To increase the cooling power, the rate of flow of the mixture to and from the mixing chamber can be increased by directly heating the still line, to pump it faster. During normal operation, without any excess heating, a flow value of 0.67 mmol/s is observed. Figure from BlueFors.

Over time, the heavier phase, i.e. rich in ^{4}He will settle to lower sections of the dilution unit, in the mixing chamber, and below the ^{3}He-rich phase.

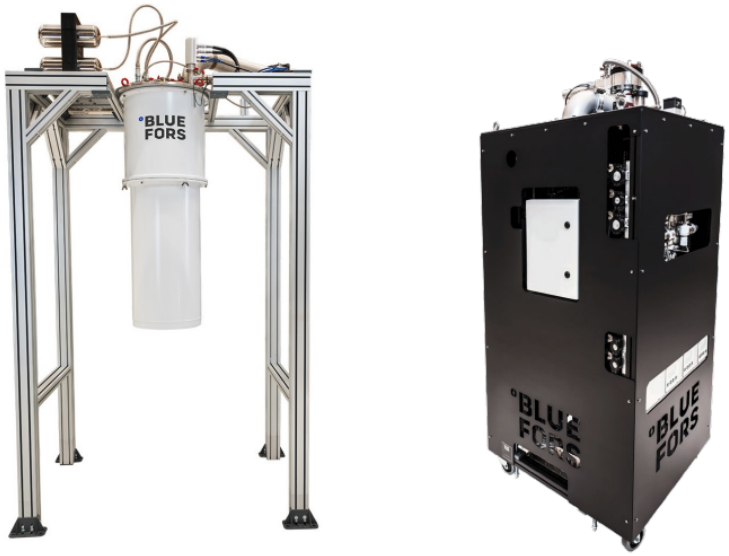

Fig. A.3.: The vacuum can on the frame is shown on the left, and the gas handling unit on the right. These are connected by bellows for the pulse tube, pumps and the He-mixture inlet/outlet.

System Description

The entire system shares a common vacuum, shown in Figure 2.10. In order to ensure that sufficient cooling from the pulse tube is provided to the dilution unit in order to start condensing, heat switches are used between the stages of the cryostat. These are made of two copper heat exchanger parts (at the warmer and colder ends) and filled with helium gas which transfers heat. In addition to this, they are also the support pillars of the cryostat. The cryostat is pre-cooled with a Cryomech pulse tube, which is in turn cooled by a ThermoFischer 1500 water chiller. The cryostat can also be operated to reach temperatures 4.2 K with just the pulse tube. With a stable dilution cycle, a base temperature of $<$30 mK can be reached. At a temperature of 100 mK, the system has a cooling power of at least 200 μW, and at its base temperature (30 mK) a cooling power $\sim$10 μW.

The cryostat can be split into two parts: one is the vacuum can in Figure 2.10, and another is the gas handling system (GHS), shown in Figure A.3 which houses all the various pumps and a compressor used to operate the internal unit in the vacuum can. This also has the control panel (details in Figure A.4) on it, which can be used to manually operate the cryostat, i.e. the valves, pumps, heat switches and the pulse tube. At each stage of the cryostat, the temperature is monitored.

Operation

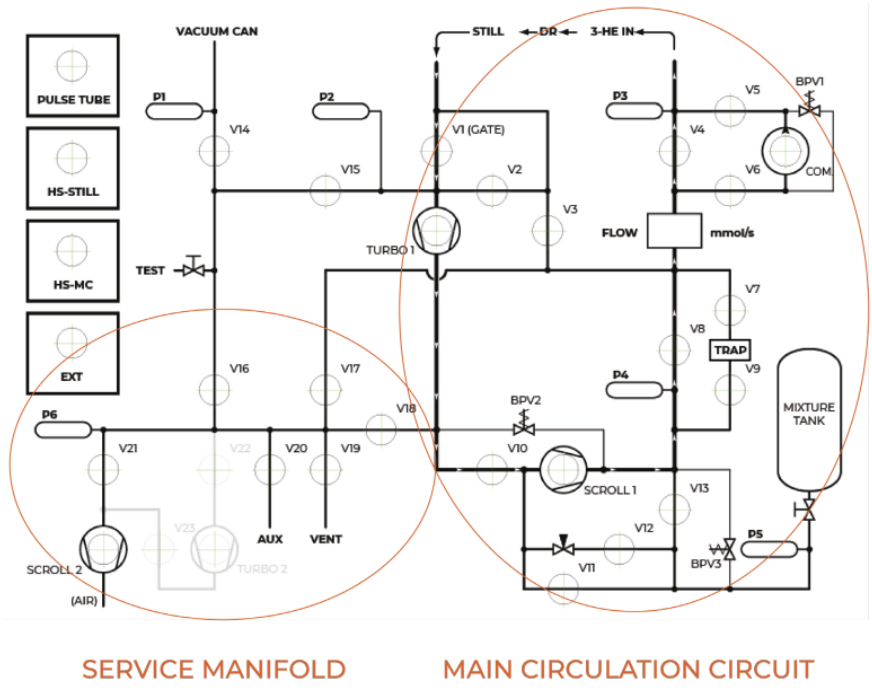

Fig. A.4.: The control panel for cryostat operation is shown here, with the service manifold and the main circulation (dilution) circuits. The service manifold are the components which connect the internal dilution cycle/unit to the air, and have to be used with care and not while under stable cooling/operation. The DR is as such within the vacuum can. There 6 pressure values tracked in the system to ensure its correct operation, with P1 being the main and shared vacuum pressure in the can. P3 and P4 are the pressures in the main working line, P5 is pressure of the mixture tank valve and P6 is the pressure at the outlet of the service manifold. The main dilution unit is run with the external trap engaged. The heat switches (HSs) are also seen in the panel and can be operated from here.

The cryostat can be operated remotely using the PC allowing for a more automated running, with a dedicated software from the manufacturer BlueFors. This ValveControl software is used to execute scripts that can be written to instruct the cryostat to operate as needed. Such scripts can be executed once other checks have been made to ensure the smooth operation and correct settings of all related equipment such as the water chiller. Scripts from the the manufacturer are used to initiate cooldowns from a fully warm system, cooling down to <30 mK. This typically takes about 14 hours and can be run until the difference in the working pressures (P3 and P4, seen in Figure A.4) is about 100 mbar and/or P6 rises beyond 10 mbar. A typical cool down run time of 30 days has been done. The main impediment to the long term cool down is also the use of the

external trap. The DR is run in the 'wet' mode, i.e. an external trap, cooled by a bath of liquid nitrogen, is used in the main dilution line to serve as a cleaning mechanism for the gases being pumped. Any impurities can be collected in the activated charcoal in the external trap and not lead to blockages in the dilution line. This bath of liquid nitrogen needs to be replaced every 11 days or so for optimal operation of the cryostat during a stable cool down. This is also another important feature of the cryostat operation, as cleaning of this trap before every cool down is essential. The same applies also for the internal trap; this is basically the dilution unit when the helium mixture has been safely collected and the system is warmed up and at room temperature. Without this, blockages can be created in the system which can lead to failure of the cool downs.
The warm up of the cryostat from a stable cool down is also done in a similar fashion to the cool down, with the execution of a script from the software. It can also be done manually and takes about 24 hours for the system to return to room temperature. Figure A.5 shows an exemplary data set of temperature over time, during the cooldown and warm up of the system.

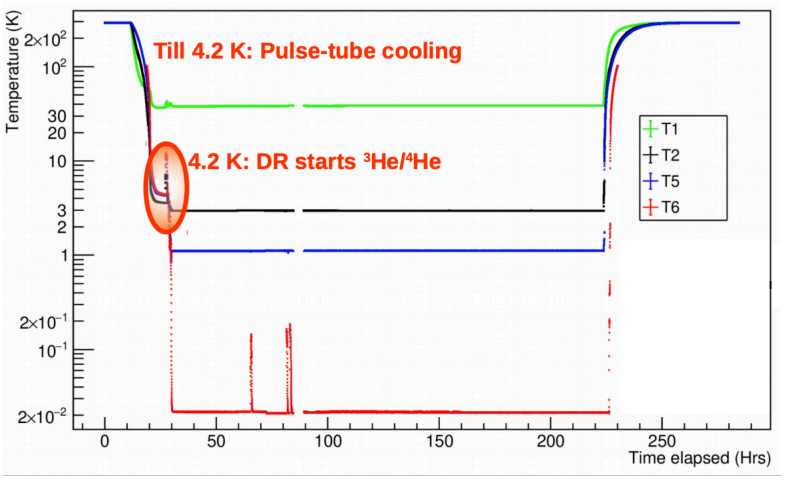

Fig. A.5.: The plot above shows the start of a cool down from room temperature. T1, T2, T5 and T6 correspond to the 40 K, 4.2 K, 1.1 K and 20 mK stages in the cryostat. The primary cooling of the system with a pulse tube and then the stable operation with the helium mixture is performed over a week. The heater at the mixing chamber (or 30 mK) stage can also be used to heat the system, as was tested around the 80-hour mark, to check the operation of the detectors. A warm up is then initiated which allows the system to return to room temperature.

Fine-tuned Cuts

B

Following from Section 4.3.1, the fine-tuned cuts for a specific ratio limit ζ_{limit} are found for a selection of fit parameters. These cuts are used for improving the pulse selection procedure. The 1064 nm photons forming the signal dataset includes ~ 1000 pulses, and the intrinsic background dataset it is compared against is comprised of $\sim 37,000$ pulses collected over 20 days of DAQ.

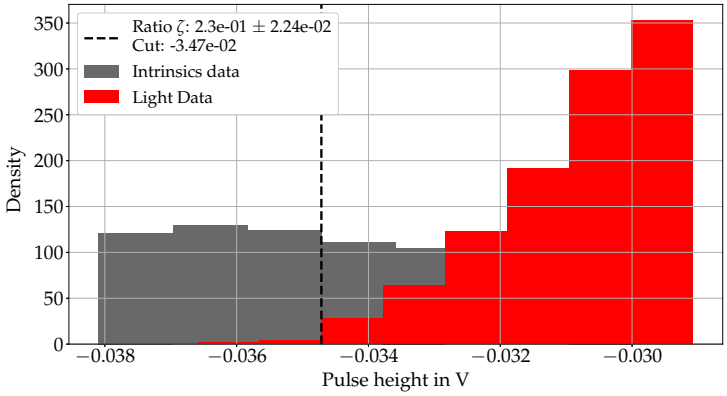

(a)

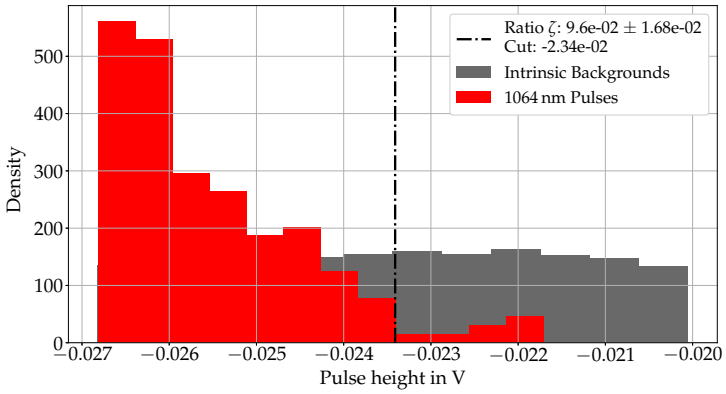

(b)

Fig. B.1.: (a) and (b) depict the fine-tuned cuts as dictated by the ratio limit $\zeta_{limit} = 0.2$ for pulse heights of the 1064 nm photons pulses and intrinsic background pulses.

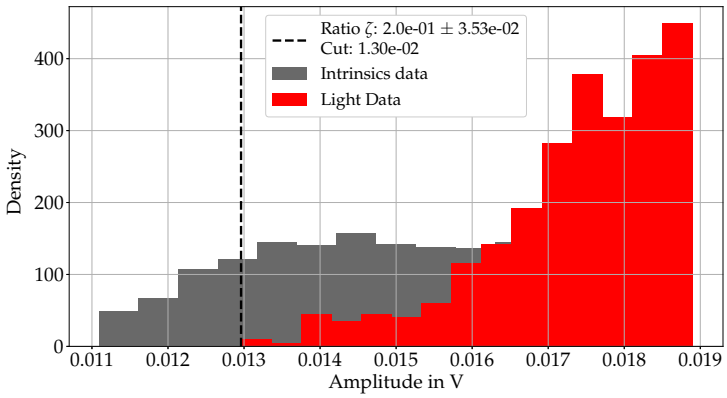

(a)

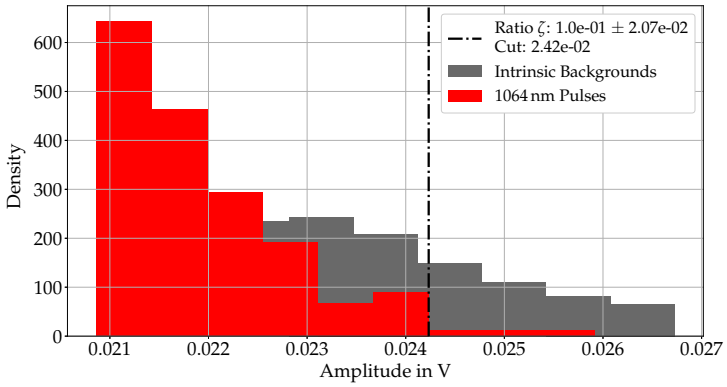

(b)

Fig. B.2.: (a) and (b) depict the fine-tuned cuts as dictated by the ratio limit $\zeta_{limit} = 0.2$ for amplitudes of the 1064 nm photons pulses and intrinsic background pulses.

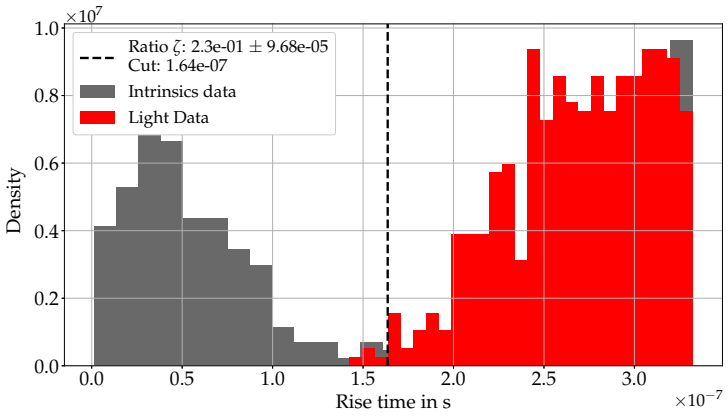

(a)

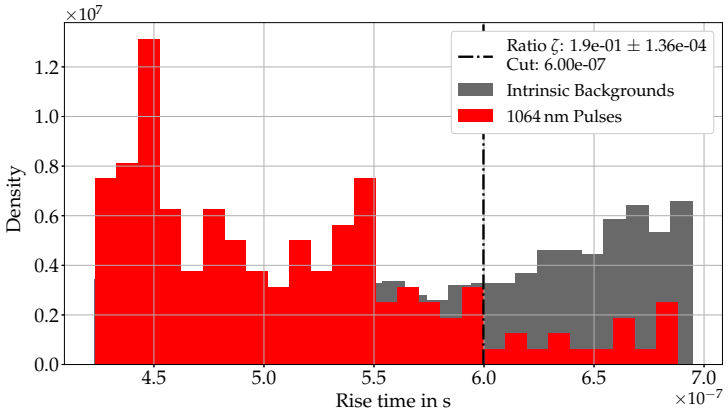

(b)

Fig. B.3.: (a) and (b) depict the fine-tuned cuts as dictated by the ratio limit $\zeta_{limit} = 0.2$ for the rise time constants of the 1064 nm photons pulses and intrinsic background pulses.

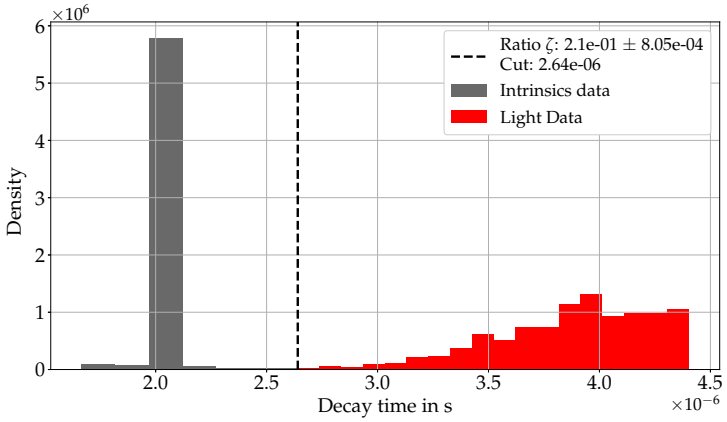

(a)

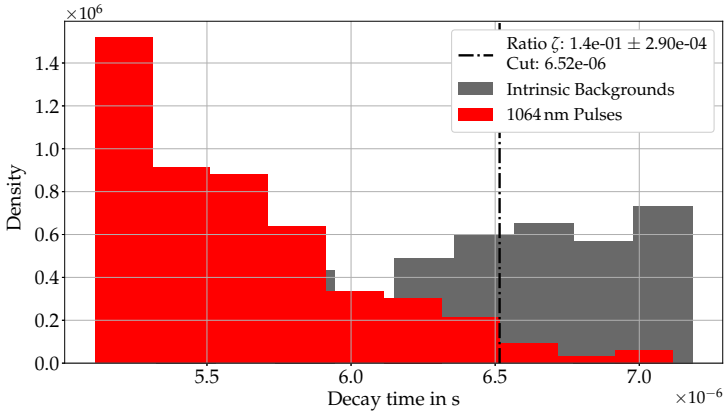

(b)

Fig. B.4.: (a) and (b) depict the fine-tuned cuts as dictated by the ratio limit $\zeta_{limit} = 0.2$ for the decay time constants of the 1064 nm photons pulses and intrinsic background pulses. The peak in the distribution at $\sim 2\,\mu$s is due the population of noise triggers which are fitted by the pulse fitting scheme with just the start values of the rise and/or decay time constants which is $2\,\mu$s. Such pulses have a large $\chi^2_{reduced}$ and can be easily rejected by the pulse selection procedure.

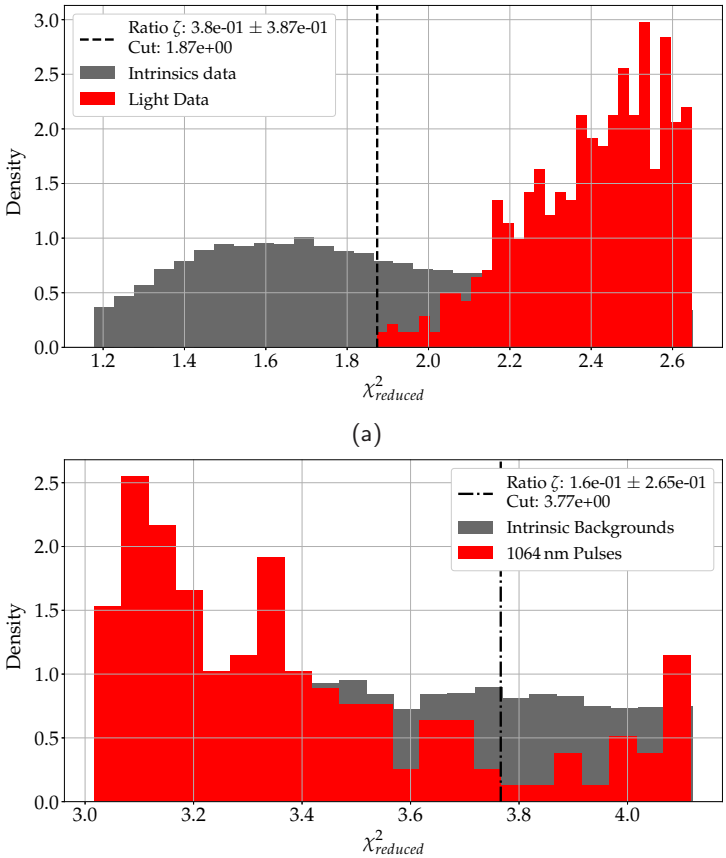

Fig. B.5.: (a) and (b) depict the fine-tuned cuts as dictated by the ratio limit $\zeta_{limit} = 0.2$ for the $\chi^2_{reduced}$ of the 1064 nm photons pulses and intrinsic background pulses.

C

Principal Component Analysis (PCA)

The PCA is used to find linear combinations of features in the original high dimensional dataset (or data matrix), i.e. interrelations in the data from the measurement, and representing the dataset in terms of its most useful components. The PCA is a well established approach, and the procedure adopted here to realize this for our setup is outlined here. A small dedicated python package *TESPCA* (using the *scikit-learn* library) is written for this.

We commence with a dataset matrix $\mathcal{V}$ which contains all triggered TES pulses (now referred to simply as triggers). Each column in this matrix is a trigger. For a dataset with T triggers of M data points in each trigger, we thus have:

$$\mathcal{V} = \Big[\text{Trigger } 1 \quad \Big| \ldots \Big| \quad \text{Trigger } T\Big]_{M\times T} . \tag{C.1}$$

Each trigger is decomposed into $\{v_i(t)\}$, where v_i is the measured voltage at a time t, and $0 \leq i \leq M$. Each v_i is further decomposed and expressed as the weighted sum of an orthonormal basis $\{w_j\}$:

$$v_i = \sum_j^T s_{ij} w_j \; (\implies v_1 = s_{11}w_1 + \ldots + s_{1T}w_T) \; . \tag{C.2}$$

Here, the s_{ij} are the coefficients or the mixing factors and the w_j are the principal components (PCs). We assume that only the first N components will be retained ($N \leq T$, and such that most of the variance of the original dataset is captured in these PCs).

For the matrix $\mathcal{V}$ we can construct its covariance matrix $\mathcal{C} = \tilde{\mathcal{V}}^T\tilde{\mathcal{V}}$ where $\tilde{\mathcal{V}}$ is the data set with the mean signal subtracted. The matrix $\mathcal{C}$ is decomposed to obtain its eigenvectors (and corresponding eigenvalues). The matrix comprised of its eigenvectors

$\mathcal{W} = \text{eigenvectors}(\mathcal{C})$ is the matrix of the PCs corresponding to each trigger in the original dataset $\mathcal{V}$:

$$\mathcal{V} = \Big[\text{Trigger } 1\Big|\ldots\Big|\text{Trigger } T\Big]_{M\times T} \tag{C.3}$$

$$\implies \mathcal{W} = \Big[\text{Column of } N \text{ PCs for Trigger } 1\Big|\ldots \ldots\Big|\text{Column of } N \text{ PCs for Trigger } T\Big]_{N\times T}. \tag{C.4}$$

Each row in $\mathcal{W}$ is then the arrays of PCs, i.e. the first row of $\mathcal{W}$ contains T entries of the first PC corresponding to each trigger respectively. To represent the original dataset $\mathcal{V}$ in terms of $\mathcal{W}$ we use $\mathcal{V} = \mathcal{S}\cdot\mathcal{W}$; and calculate the coefficient matrix $\mathcal{S}$ using:

$$\mathcal{S} = \left[\mathcal{V}\cdot\mathcal{W}^T\right]_{(M\times N)} \tag{C.5}$$

We thus have $\mathcal{W}$ which is the matrix of the PCs (reduced dimensionality compared to $\mathcal{V}$) and the coefficient matrix $\mathcal{S}$ for this specific $\mathcal{W}$.
To obtain the recreated dataset $\mathcal{V}'$ we need only perform $\mathcal{V}' = \mathcal{S}\cdot\mathcal{W}$. Performing $\mathcal{V}' = \mathcal{S}\cdot\mathcal{W}$ here will not directly reproduce the full dataset $\mathcal{V}$ as $\mathcal{W}$ features a reduction in dimensionality since $N \leq T$. If we use $N = T$ then we will be back to the beginning with $\mathcal{V}' = \mathcal{V}$.
The higher the value of N the more close we will be to the data pulse in our recreation, in general, as seen in Figure C.2. We note that $\mathcal{V}'$ has the same dimensions as $\mathcal{V}$, but each measured v_i has lesser noise-carrying contributions which come from higher PCs. As seen also in Figure 3.8b, the independent contributions from PCs other than the first are not significant. This is seen also from Figure C.1

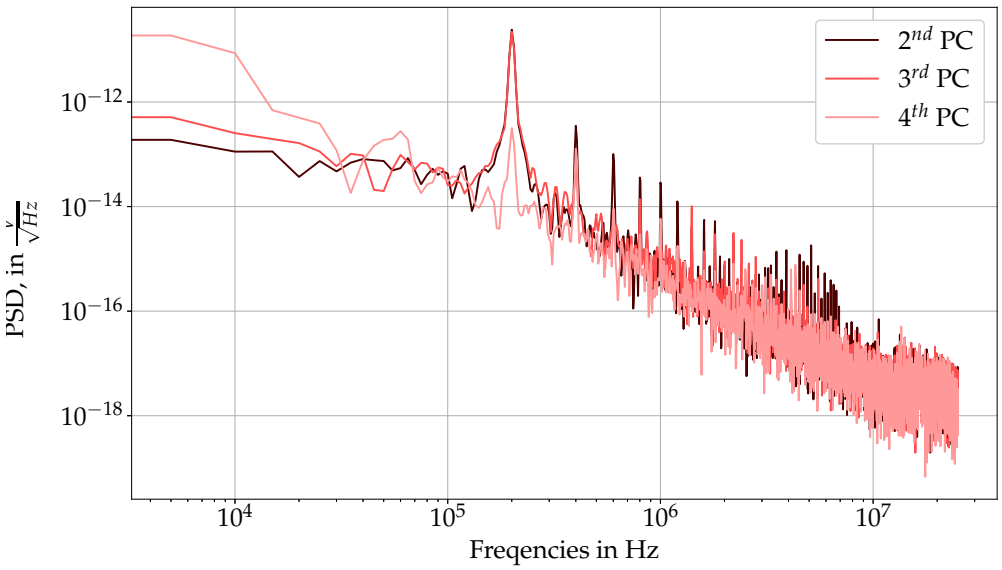

Fig. C.1.: The power spectral density for the noise-carrying single contributions of the 2^{nd}, 3^{rd}, and 4^{th} PCs is shown, as seen from Figure 3.8b. The noise fluctuations due to the $\mathcal{O}(100)$ kHz harmonics is seen, in particular from the contributions due to the 2^{nd} and 3^{rd} PC.

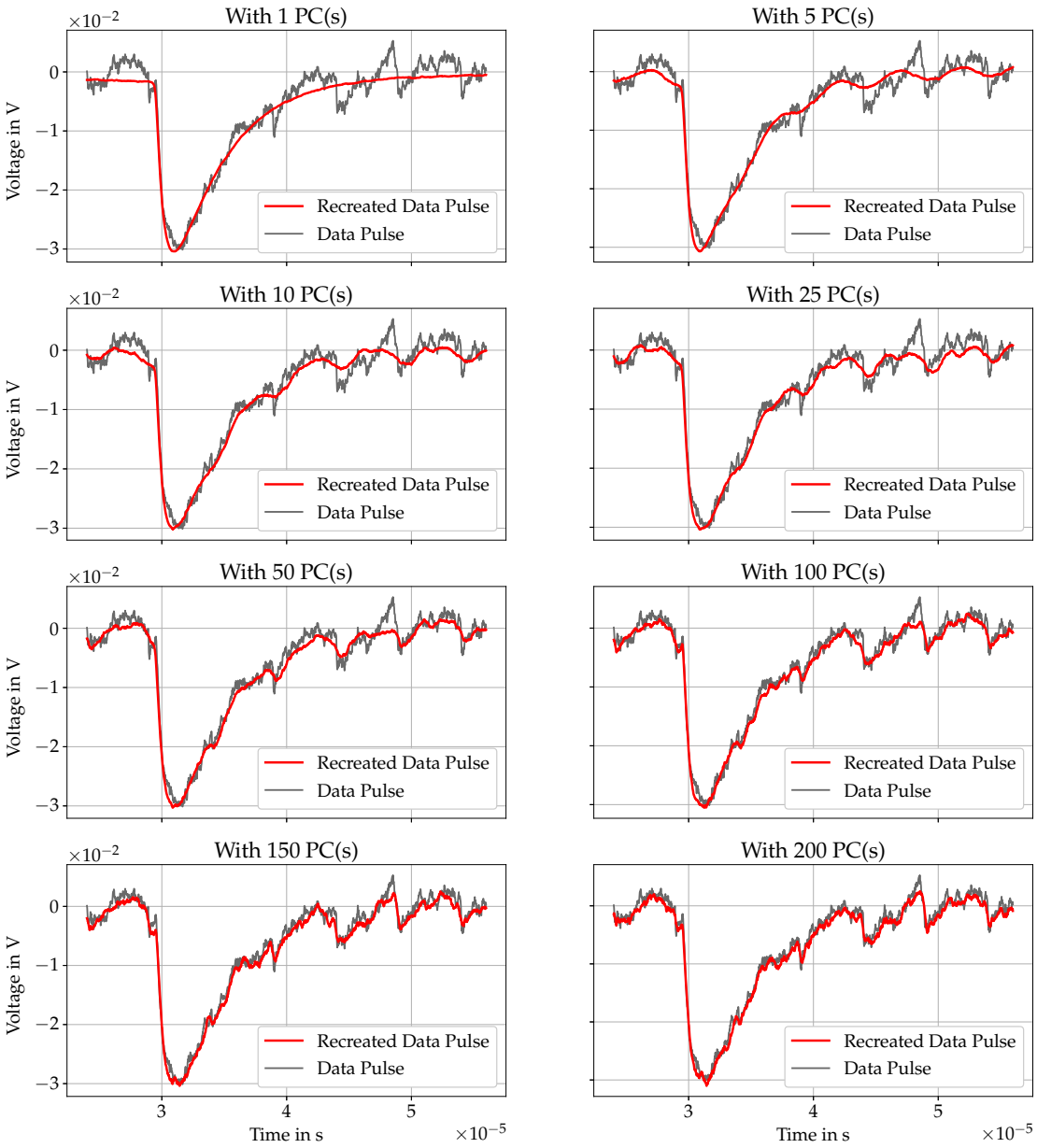

Fig. C.2.: The recreation of a 1064 nm TES pulse with increasing number of PCs, which are noted to add noise elements to the recreated pulse. With higher PCs, the recreated pulse traces the raw triggered pulse more faithfully.

D

In Tandem with Machine Learning

The use of machine learning has also been investigated for pulse discrimination. The proliferation of machine learning techniques for use in data analysis in high-energy particle physics is highly pervasive, and has been well documented [126]. For processing multiple pulses and 'tagging' them as a signal or background event, the implementation of a machine learning algorithm can be useful. Pre-studies using machine learning techniques have been done for TES pulses[1], and achieves results similar to those found by the pulse selection methods discussed in this work. The full reproduction of this is not done here, but some results are described.

In a rudimentary scheme, the fitting parameters obtained from the free fit approach (or indeed, any other approach) are used to train a model to select and categorise TES pulses as either background pulses or signal photons. In this format, this works in tandem with the fitting procedure and can be compared to it for a pulse selection scheme. In essence, the idea is to train a model with a dataset comprising of (in this case, intrinsic) background pulses and 1064 nm photon pulses with some classifier. This classifier can be different and a few different ones are tested, such as Decision Tree, Boosted Decision Tree, Random Forest etc. This trained model is then tested on a test dataset also comprising of background and signal pulses as before, in order to see how well it can perform. The datasets are split typically 80%-20% in training and test datasets respectively. With such a routine, a machine learning approach can also obtain a dark rate (over a 20 day period, with intrinsic backgrounds only) of $\mathcal{O}(10^{-5})$ cps, a significance $S < 10\sigma$ (as in Table 4.1) and a signal selection efficiency of nearly 100%.

The pulse selection procedure (Section 4.3.1) outlined first in this work has been dictated by only the 1064 nm signal photon pulses, following a more classical approach. The machine learning approach receives input also from the background pulses, expanding its scope and moving it closer to the fine-tuned cuts (Section 4.3.1) in essence. The full

[1] Manuel Meyer, Internal Communication.

details of the machine learning techniques is beyond the scope of this work, but the results achieved by a machine learning approach can be emulated with the fined-tuned cuts.
A separate analysis was made to mimic this approach, by:

- Combining 20 days worth of intrinsic background events (∼37,000 pulses) with nearly 1000 1064 nm signal photon pulses
- Fitting these following the free fit approach, each one independently, while maintaining the identity of each pulse as either a background or signal pulse
- Splitting this large dataset of the fitted pulses into a training and testing dataset
- Finding fine-tuned cuts on on the training dataset, from the 1064 nm photon pulses. These are the fine-tuned cuts on the parameters as mentioned in Table 4.3
- Finding the remnant signal photons once the fine-tuned cuts have been applied, and the background pulses which survive the cuts as well.

The results of this analysis line, to imitate to some extent the machine learning algorithm, are summarised for some fine-tuned cuts (with the parameter ζ_{limit} as in Section 4.3.1) in Tables D.2 and D.1.

Setting up this analysis to reproduce the results from the machine learning based selection, we obtain again a comparable dark rate $\mathcal{O}(10^{-5})$ cps. The general pulse selection procedure also achieved this dark rate. The analysis outlined above is only a simple reproduction made to investigate the procedure of the machine learning technique with some success. In its current form, the machine learning analysis works with the fitting procedure, but other analyses are also being constructed. The major difference the use of the raw timeline of the triggered TES pulses, and not the fitting procedure's parameters. The fitting reduced the TES pulse to a few parameters, which may or not be all equally useful. The next machine learning tests can help understand which sections of the TES pulses are of higher importance when it comes to pulse discrimination, etc.

ζ_{limit}	**No. of surviving pulses**	**Dark Rate** in 10^{-6} cps	**Percentage Signal Acceptance**
0.15	16	$9.25^{+2.9}_{-1.7}$	83.86%
0.2	10	$5.78^{+2.4}_{-1.3}$	80.3%
0.25	9	$5.20^{+2.3}_{-1.2}$	80.11%
0.3	9	$5.20^{+2.3}_{-1.2}$	78.98%

Tab. D.1.: With the fine-tuned cuts obtained with some ratio limits ζ_{limit}, the different surviving pulses from the collected background pulses are shown. The corresponding dark rate, over the 20 day period, is shown as well.

Dataset Type	ζ_{limit}	Percentage Signal Acceptance	Percentage Background Acceptance (as signal)
Test	0.1	88.3%	0.02709%
Train	0.1	83.4%	0.0508%
Test	0.2	85%	0%
Train	0.2	79.1%	0.0338%

Tab. D.2.: For a dataset split 80%-20% into training and testing datasets, the fine-tuned cuts obtained for two exemplary values of the ratio limit ζ_{limit} are shown above. The dataset as a whole contains ∼37,000 intrinsic background events over 20 days and about 1,000 1064 nm photon pulses. The signal acceptance is the ratio of signal photons which survive the cuts imposed on them to the original number of signal photons that comprised the corresponding dataset (test or train). The background acceptance is the the ratio of the surviving background pulses which survive the cuts to the original number of background pulses in that particular dataset. These surviving background pulses are indistinguishable from 1064 nm signal photons, should the cuts be strict enough.

List of Tables

List of Figures

Bibliography

[1] Mary K. Gaillard et al. “The standard model of particle physics”. In: *Rev. Mod. Phys.* 71 (2 1999), S96–S111. DOI: 10.1103/RevModPhys.71.S96 (cit. on p. 1).

[2] ATLAS Collaboration. “Observation of a new particle in the search for the Standard Model Higgs boson with the ATLAS detector at the LHC”. In: *Physics Letters B* 716.1 (2012), pp. 1–29. DOI: https://doi.org/10.1016/j.physletb.2012.08.020 (cit. on p. 1).

[3] CMS Collaboration. “Observation of a new boson at a mass of 125 GeV with the CMS experiment at the LHC”. In: *Physics Letters B* 716.1 (2012), pp. 30–61. DOI: https://doi.org/10.1016/j.physletb.2012.08.021 (cit. on p. 1).

[4] Hai-Yang Cheng. “The strong CP problem revisited”. In: *Physics Reports* 158.1 (1988), pp. 1–89. DOI: https://doi.org/10.1016/0370-1573(88)90135-4 (cit. on p. 1).

[5] Gianfranco Bertone. “The moment of truth for WIMP dark matter”. In: *Nature* 468.7322 (2010), pp. 389–393 (cit. on p. 1).

[6] Anadi Canepa. “Searches for supersymmetry at the Large Hadron Collider”. In: *Reviews in Physics* 4 (2019), p. 100033. DOI: https://doi.org/10.1016/j.revip.2019.100033 (cit. on p. 1).

[7] Laura Baudis. “Dark matter searches”. In: *Annalen der Physik* 528.1-2 (2016), pp. 74–83. DOI: https://doi.org/10.1002/andp.201500114. eprint: https://onlinelibrary.wiley.com/doi/pdf/10.1002/andp.201500114 (cit. on p. 2).

[8] Rikhav Shah et al. “Characterising a Single-Photon Detector for ALPS II”. In: 2022. DOI: 10.1007/s10909-022-02720-0 (cit. on pp. 3, 43).

[9] Rikhav Shah et al. “TES Detector for ALPS II”. In: *PoS* EPS-HEP2021 (2022), p. 801. DOI: 10.22323/1.398.0801 (cit. on pp. 3, 58).

[10] Andreas Ringwald. “Searching for axions and ALPs from string theory”. In: *Journal of Physics: Conference Series* 485 (2014), p. 012013. DOI: 10.1088/1742-6596/485/1/012013 (cit. on p. 4).

[11] P. G. Harris et al. “New Experimental Limit on the Electric Dipole Moment of the Neutron”. In: *Phys. Rev. Lett.* 82 (5 1999), pp. 904–907. DOI: 10.1103/PhysRevLett.82.904 (cit. on p. 4).

[12] Joerg Jaeckel and Andreas Ringwald. “The Low-Energy Frontier of Particle Physics”. In: *Annual Review of Nuclear and Particle Science* 60.1 (2010), pp. 405–437. DOI: 10.1146/annurev.nucl.012809.104433. eprint: https://doi.org/10.1146/annurev.nucl.012809.104433 (cit. on pp. 4–6).

[13] R. D. Peccei and Helen R. Quinn. “CP Conservation in the Presence of Pseudoparticles”. In: *Phys. Rev. Lett.* 38 (25 1977), pp. 1440–1443. DOI: 10.1103/PhysRevLett.38.1440 (cit. on p. 4).

[14] R. D. Peccei and Helen R. Quinn. “Constraints imposed by CP conservation in the presence of pseudoparticles”. In: *Phys. Rev. D* 16 (6 1977), pp. 1791–1797. DOI: 10.1103/PhysRevD.16.1791 (cit. on p. 4).

[15] F. Wilczek. “Problem of Strong P and T Invariance in the Presence of Instantons”. In: *Phys. Rev. Lett.* 40 (5 1978), pp. 279–282. DOI: 10.1103/PhysRevLett.40.279 (cit. on p. 4).

[16] Steven Weinberg. “A New Light Boson?” In: *Phys. Rev. Lett.* 40 (4 1978), pp. 223–226. DOI: 10.1103/PhysRevLett.40.223 (cit. on p. 4).

[17] Luca Di Luzio et al. “The landscape of QCD axion models”. In: *Physics Reports* 870 (2020). The landscape of QCD axion models, pp. 1–117. DOI: https://doi.org/10.1016/j.physrep.2020.06.002 (cit. on p. 4).

[18] Michael Dine et al. “A simple solution to the strong CP problem with a harmless axion”. In: *Physics Letters B* 104.3 (1981), pp. 199–202. DOI: https://doi.org/10.1016/0370-2693(81)90590-6 (cit. on p. 4).

[19] Jihn E. Kim. “Weak-Interaction Singlet and Strong CP Invariance”. In: *Phys. Rev. Lett.* 43 (2 1979), pp. 103–107. DOI: 10.1103/PhysRevLett.43.103 (cit. on p. 4).

[20] Marco Farina et al. “The photo-philic QCD axion”. In: *Journal of High Energy Physics* 2017.1 (2017), p. 95. DOI: 10.1007/JHEP01(2017)095 (cit. on p. 4).

[21] Anson Hook. “Solving the Hierarchy Problem Discretely”. In: *Phys. Rev. Lett.* 120 (26 2018), p. 261802. DOI: 10.1103/PhysRevLett.120.261802 (cit. on p. 4).

[22] Alberto Salvio. “A fundamental QCD axion model”. In: *Physics Letters B* 808 (2020), p. 135686. DOI: https://doi.org/10.1016/j.physletb.2020.135686 (cit. on p. 4).

[23] Anton V. Sokolov and Andreas Ringwald. “Photophilic hadronic axion from heavy magnetic monopoles”. In: *Journal of High Energy Physics* 2021.6 (2021), p. 123 (cit. on p. 5).

[24] Mark Srednicki. “Axion couplings to matter: (I). CP-conserving parts”. In: *Nuclear Physics B* 260.3 (1985), pp. 689–700. DOI: https://doi.org/10.1016/0550-3213(85)90054-9 (cit. on p. 5).

[25] Masahiro Kawasaki and Kazunori Nakayama. “Axions: Theory and Cosmological Role”. In: *Annual Review of Nuclear and Particle Science* 63.1 (2013), pp. 69–95. DOI: 10.1146/annurev-nucl-102212-170536. eprint: https://doi.org/10.1146/annurev-nucl-102212-170536 (cit. on p. 5).

[26] Peter Svrcek and Edward Witten. “Axions in string theory”. In: *Journal of High Energy Physics* 2006.06 (2006), pp. 051–051. DOI: 10.1088/1126-6708/2006/06/051 (cit. on p. 5).

[27] Joseph P Conlon. “Hierarchy problems in string theory and large volume models”. In: *Modern Physics Letters A* 23.01 (2008), pp. 1–16 (cit. on p. 5).

[28] Sudhakar Panda et al. “Axions as quintessence in string theory”. In: *Phys. Rev. D* 83 (8 2011), p. 083506. DOI: 10.1103/PhysRevD.83.083506 (cit. on p. 5).

[29] Bob Holdom. “Two $U(1)$’s and ϵ charge shifts”. In: *Physics Letters B* 166.2 (1986), pp. 196–198. DOI: https://doi.org/10.1016/0370-2693(86)91377-8 (cit. on p. 5).

[30] John Preskill et al. “Cosmology of the invisible axion”. In: *Physics Letters B* 120.1 (1983), pp. 127–132. DOI: https://doi.org/10.1016/0370-2693(83)90637-8 (cit. on p. 6).

[31] L.F. Abbott and P. Sikivie. “A cosmological bound on the invisible axion”. In: *Physics Letters B* 120.1 (1983), pp. 133–136. DOI: https://doi.org/10.1016/0370-2693(83)90638-X (cit. on p. 6).

[32] Max Tegmark et al. “High resolution foreground cleaned CMB map from WMAP”. In: *Phys. Rev. D* 68 (12 2003), p. 123523. DOI: 10.1103/PhysRevD.68.123523 (cit. on p. 6).

[33] Pierre Sikivie. “Evidence for ring caustics in the Milky Way”. In: *Physics Letters B* 567.1 (2003), pp. 1–8. DOI: https://doi.org/10.1016/S0370-2693(03)00863-3 (cit. on p. 6).

[34] P. Sikivie and Q. Yang. “Bose-Einstein Condensation of Dark Matter Axions”. In: *Phys. Rev. Lett.* 103 (11 2009), p. 111301. DOI: 10.1103/PhysRevLett.103.111301 (cit. on p. 6).

[35] F. et al Aharonian. “A low level of extragalactic background light as revealed by γ-rays from blazars”. In: *Nature* 440.7087 (2006), pp. 1018–1021 (cit. on p. 6).

[36] Alessandro De Angelis et al. “Evidence for a new light spin-zero boson from cosmological gamma-ray propagation?” In: *Phys. Rev. D* 76 (12 2007), p. 121301. DOI: 10.1103/PhysRevD.76.121301 (cit. on p. 6).

[37] Melanie Simet et al. “Milky Way as a kiloparsec-scale axionscope”. In: *Phys. Rev. D* 77 (6 2008), p. 063001. DOI: 10.1103/PhysRevD.77.063001 (cit. on p. 6).

[38] Manuel Meyer et al. “First lower limits on the photon-axion-like particle coupling from very high energy gamma-ray observations”. In: *Phys. Rev. D* 87 (3 2013), p. 035027. DOI: 10.1103/PhysRevD.87.035027 (cit. on p. 6).

[39] Georg G Raffelt. *Stars as laboratories for fundamental physics: The astrophysics of neutrinos, axions, and other weakly interacting particles*. University of Chicago press, 1996 (cit. on p. 6).

[40] Georg G. Raffelt. “Astrophysical axion bounds diminished by screening effects”. In: *Phys. Rev. D* 33 (4 1986), pp. 897–909. DOI: 10.1103/PhysRevD.33.897 (cit. on p. 6).

[41] Paolo Gondolo and Georg G. Raffelt. “Solar neutrino limit on axions and keV-mass bosons”. In: *Phys. Rev. D* 79 (10 2009), p. 107301. DOI: 10.1103/PhysRevD.79.107301 (cit. on p. 6).

[42] J Isern et al. “Axions and the cooling of white dwarf stars”. In: *The Astrophysical Journal* 682.2 (2008), p. L109 (cit. on p. 6).

[43] P. Sikivie. “Experimental Tests of the "Invisible" Axion”. In: *Phys. Rev. Lett.* 51 (16 1983), pp. 1415–1417. DOI: 10.1103/PhysRevLett.51.1415 (cit. on p. 6).

[44] Peter W. Graham et al. “Experimental Searches for the Axion and Axion-Like Particles”. In: *Annual Review of Nuclear and Particle Science* 65.1 (2015), pp. 485–514. DOI: 10.1146/annurev-nucl-102014-022120. eprint: https://doi.org/10.1146/annurev-nucl-102014-022120 (cit. on pp. 6, 9, 11).

[45] Ian P. Stern et al. “Axion dark matter searches”. In: *AIP Conference Proceedings* 1604.1 (2014), pp. 456–461. DOI: 10.1063/1.4883465. eprint: https://aip.scitation.org/doi/pdf/10.1063/1.4883465 (cit. on p. 7).

[46] Dmitry Budker et al. “Proposal for a Cosmic Axion Spin Precession Experiment (CASPEr)”. In: *Phys. Rev. X* 4 (2 2014), p. 021030. DOI: 10.1103/PhysRevX.4.021030 (cit. on p. 7).

[47] K. Zioutas et al. “A decommissioned LHC model magnet as an axion telescope”. In: *Nuclear Instruments and Methods in Physics Research Section A: Accelerators, Spectrometers, Detectors and Associated Equipment* 425.3 (1999), pp. 480–487. DOI: https://doi.org/10.1016/S0168-9002(98)01442-9 (cit. on p. 7).

[48] A. et al. Abeln and the IAXO Collaboration. “Conceptual design of BabyIAXO, the intermediate stage towards the International Axion Observatory”. In: *Journal of High Energy Physics* 2021.5 (2021), p. 137. DOI: 10.1007/JHEP05(2021)137 (cit. on pp. 7, 8).

[49] E Armengaud et al. “Conceptual design of the International Axion Observatory (IAXO)”. In: *Journal of Instrumentation* 9.05 (2014), T05002–T05002. DOI: 10.1088/1748-0221/9/05/t05002 (cit. on p. 7).

[50] Klaus Ehret et al. “New ALPS results on hidden-sector lightweights”. In: *Physics Letters B* 689.4 (2010), pp. 149–155. DOI: https://doi.org/10.1016/j.physletb.2010.04.066 (cit. on pp. 8, 9).

[51] Pierre Pugnat et al. “Results from the OSQAR photon-regeneration experiment: No light shining through a wall”. In: *Phys. Rev. D* 78 (9 2008), p. 092003. DOI: 10.1103/PhysRevD.78.092003 (cit. on pp. 8, 9).

[52] Jan Eike von Seggern. “Constraining weakly interacting slim particles with a massive star and in the laboratory”. PhD thesis. DESY, 2014 (cit. on pp. 9, 12).

[53] A. V. Afanasev et al. *Production and detection of very light spin-zero bosons at optical frequencies*. 2006. arXiv: hep-ph/0605250 [hep-ph] (cit. on p. 9).

[54] A. S. Chou et al. “Search for Axionlike Particles Using a Variable-Baseline Photon-Regeneration Technique”. In: *Phys. Rev. Lett.* 100 (8 2008), p. 080402. DOI: 10.1103/PhysRevLett.100.080402 (cit. on p. 9).

[55] C. Robilliard et al. “No “Light Shining through a Wall”: Results from a Photoregeneration Experiment”. In: *Phys. Rev. Lett.* 99 (19 2007), p. 190403. DOI: 10.1103/PhysRevLett.99.190403 (cit. on p. 9).

[56] R. Cameron et al. “Search for nearly massless, weakly coupled particles by optical techniques”. In: *Phys. Rev. D* 47 (9 1993), pp. 3707–3725. DOI: 10.1103/PhysRevD.47.3707 (cit. on p. 9).

[57] R Bähre et al. “Any light particle search II — Technical Design Report”. In: *Journal of Instrumentation* 8.09 (2013), T09001–T09001. DOI: 10.1088/1748-0221/8/09/t09001 (cit. on pp. 10–14).

[58] Clemens Albrecht et al. “Straightening of superconducting HERA dipoles for the any-light-particle-search experiment ALPS II”. In: *EPJ Techniques and Instrumentation* 8.1 (2021), p. 5. DOI: 10.1140/epjti/s40485-020-00060-5 (cit. on p. 10).

[59] M. Diaz Ortiz et al. “Design of the ALPS II optical system”. In: *Physics of the Dark Universe* 35 (2022), p. 100968. DOI: https://doi.org/10.1016/j.dark.2022.100968 (cit. on p. 10).

[60] Paola Arias et al. “Optimizing light-shining-through-a-wall experiments for axion and other weakly interacting slim particle searches”. In: *Phys. Rev. D* 82 (11 2010), p. 115018. DOI: 10.1103/PhysRevD.82.115018 (cit. on p. 11).

[61] Zachary R. Bush et al. “Coherent detection of ultraweak electromagnetic fields”. In: *Phys. Rev. D* 99 (2 2019), p. 022001. DOI: 10.1103/PhysRevD.99.022001 (cit. on p. 14).

[62] Katharina-Sophie Isleif. “The Any Light Particle Search experiment at DESY”. In: *arXiv preprint arXiv:2202.07306* (2022) (cit. on p. 14).

[63] Ayman Hallal et al. “The heterodyne sensing system for the ALPS II search for sub-eV weakly interacting particles”. In: *Physics of the Dark Universe* 35 (2022), p. 100914. DOI: https://doi.org/10.1016/j.dark.2021.100914 (cit. on p. 14).

[64] E. Previtali. “20 years of cryogenic particle detectors: past, present and future”. In: *Nuclear Physics B - Proceedings Supplements* 150 (2006). Proceedings of the 9th Topical Seminar on Innovative Particle and Radiation Detectors, pp. 3–8. DOI: https://doi.org/10.1016/j.nuclphysbps.2005.04.060 (cit. on p. 14).

[65] Dmitry V. Morozov et al. “Superconducting photon detectors”. In: *Contemporary Physics* 0.0 (2022), pp. 1–23. DOI: 10.1080/00107514.2022.2043596. eprint: https://doi.org/10.1080/00107514.2022.2043596 (cit. on p. 14).

[66] Joel N Ullom and Douglas A Bennett. “Review of superconducting transition-edge sensors for x-ray and gamma-ray spectroscopy”. In: *Superconductor Science and Technology* 28.8 (2015), p. 084003 (cit. on pp. 14, 16, 29).

[67] Kent D Irwin and Gene C Hilton. “Transition-edge sensors”. In: *Cryogenic particle detection* (2005), pp. 63–150 (cit. on pp. 16, 19, 21, 23).

[68] Dan McCammon. “Thermal equilibrium calorimeters–an introduction”. In: *Cryogenic particle detection* (2005), pp. 1–34 (cit. on p. 16).

[69] Jan Dreyling-Eschweiler. *A superconducting microcalorimeter for low-flux detection of near-infrared single photons*. Tech. rep. Deutsches Elektronen-Synchrotron (DESY), 2014 (cit. on pp. 16, 22, 24, 27, 33, 41, 43, 59, 97).

[70] John Clarke and Alex I Braginski. *The SQUID handbook*. Vol. 1. Wiley Online Library, 2004 (cit. on pp. 16, 24, 25).

[71] J. Bardeen et al. “Theory of Superconductivity”. In: *Phys. Rev.* 108 (5 1957), pp. 1175–1204. DOI: 10.1103/PhysRev.108.1175 (cit. on p. 16).

[72] Reinhold Kleiner and Werner Buckel. *Superconductivity: an introduction*. John Wiley & Sons, 2016 (cit. on p. 17).

[73] Sergey V Vonsovsky et al. *Superconductivity of transition metals: their alloys and compounds*. Springer, 1982 (cit. on p. 17).

[74] A. Zehnder. “Response of superconductive films to localized energy deposition”. In: *Phys. Rev. B* 52 (17 1995), pp. 12858–12866. DOI: 10.1103/PhysRevB.52.12858 (cit. on p. 17).

[75] A. G. Kozorezov et al. “Quasiparticle-phonon downconversion in nonequilibrium superconductors”. In: *Phys. Rev. B* 61 (17 2000), pp. 11807–11819. DOI: 10.1103/PhysRevB.61.11807 (cit. on p. 17).

[76] Walther Meissner and Robert Ochsenfeld. “Ein neuer effekt bei eintritt der supraleitfähigkeit”. In: *Naturwissenschaften* 21.44 (1933), pp. 787–788 (cit. on p. 17).

[77] Aaron J Miller et al. “Demonstration of a low-noise near-infrared photon counter with multiphoton discrimination”. In: *Applied Physics Letters* 83.4 (2003), pp. 791–793 (cit. on p. 18).

[78] Mark Anton Lindeman. *Microcalorimetry and the transition-edge sensor*. University of California, Davis, 2000 (cit. on p. 21).

[79] Daniel S Swetz et al. “Current distribution and transition width in superconducting transition-edge sensors”. In: *Applied Physics Letters* 101.24 (2012), p. 242603 (cit. on p. 22).

[80] John Clarke et al. *The Squid Handbook.Vol. 2 Applications of SQUIDS and SQUID systems*. English. Germany: WILEY-VCH VERLAG, 2006 (cit. on p. 23).

[81] D. Drung et al. “Highly Sensitive and Easy-to-Use SQUID Sensors”. In: *IEEE Transactions on Applied Superconductivity* 17.2 (2007), pp. 699–704. DOI: 10.1109/TASC.2007.897403 (cit. on p. 23).

[82] Dietmar Drung et al. “Low-noise ultra-high-speed dc SQUID readout electronics”. In: *Superconductor Science and Technology* 19.5 (2006), S235–S241. DOI: 10.1088/0953-2048/19/5/s15 (cit. on p. 23).

[83] Fritz London. *Superfluids: Macroscopic theory of superconductivity*. Vol. 1. Dover publications, 1961 (cit. on p. 23).

[84] Bascom S Deaver Jr and William M Fairbank. “Experimental evidence for quantized flux in superconducting cylinders”. In: *Physical Review Letters* 7.2 (1961), p. 43 (cit. on p. 23).

[85] Robert Doll and M Näbauer. “Experimental proof of magnetic flux quantization in a superconducting ring”. In: *Physical Review Letters* 7.2 (1961), p. 51 (cit. on p. 23).

[86] Brian David Josephson. “Possible new effects in superconductive tunnelling”. In: *Physics letters* 1.7 (1962), pp. 251–253 (cit. on p. 24).

[87] Konstantin K Likharev. *Dynamics of Josephson junctions and circuits*. Routledge, 2022 (cit. on p. 24).

[88] Thomas Gerrits et al. *Superconducting Transition Edge Sensors for Quantum Optics*. en. Springer, Berlin, -1, 2015 (cit. on p. 28).

[89] Andrea Giachero et al. “Progress in the Development of TES Microcalorimeter Detectors Suitable for Neutrino Mass Measurement”. In: *IEEE Transactions on Applied Superconductivity* 31.5 (2021), pp. 1–5. DOI: 10.1109/TASC.2021.3051104 (cit. on p. 28).

[90] Thomas Gerrits et al. “On-chip, photon-number-resolving, telecommunication-band detectors for scalable photonic information processing”. In: *Phys. Rev. A* 84 (6 2011), p. 060301. DOI: 10.1103/PhysRevA.84.060301 (cit. on p. 28).

[91] Matteo D’Andrea et al. “Single Pixel Performance of a 32 × 32 Ti/Au TES Array With Broadband X-Ray Spectra”. In: *IEEE Transactions on Applied Superconductivity* 31.5 (2021), pp. 1–5. DOI: 10.1109/TASC.2021.3065303 (cit. on p. 28).

[92] A Kozorezov et al. “Electrical noise in a TES as a resistively shunted conducting junction”. In: *Journal of low temperature physics* 167.3 (2012), pp. 108–113 (cit. on p. 29).

[93] A. E. Lita et al. “Superconducting transition-edge sensors optimized for high-efficiency photon-number resolving detectors”. In: *Advanced Photon Counting Techniques IV*. Ed. by Mark A. Itzler and Joe C. Campbell. Vol. 7681. International Society for Optics and Photonics. SPIE, 2010, pp. 71 –80. DOI: 10.1117/12.852221 (cit. on pp. 29, 30, 82).

[94] A.E. Lita et al. “Tuning of tungsten thin film superconducting transition temperature for fabrication of photon number resolving detectors”. In: *IEEE Transactions on Applied Superconductivity* 15.2 (2005), pp. 3528–3531. DOI: 10.1109/TASC.2005.849033 (cit. on p. 30).

[95] F. C. Wellstood et al. “Hot-electron effects in metals”. In: *Phys. Rev. B* 49 (9 1994), pp. 5942–5955. DOI: 10.1103/PhysRevB.49.5942 (cit. on p. 30).

[96] A. E. Lita et al. “Superconducting transition-edge sensors optimized for high-efficiency photon-number resolving detectors”. In: *Advanced Photon Counting Techniques IV*. Ed. by Mark A. Itzler and Joe C. Campbell. Vol. 7681. International Society for Optics and Photonics. SPIE, 2010, pp. 71 –80. DOI: 10.1117/12.852221 (cit. on p. 32).

[97] Noemie Bastidon. *The cryogenic photon detection system for the ALPS II experiment: characterization, optimization and background rejection.* Tech. rep. Deutsches Elektronen-Synchrotron (DESY), 2016 (cit. on p. 33).

[98] KD Irwin. “An application of electrothermal feedback for high resolution cryogenic particle detection”. In: *Applied Physics Letters* 66.15 (1995), pp. 1998–2000 (cit. on p. 37).

[99] Christoph Weinsheimer. “Light-Shining-through-a-Wall : Searching for Axion-Like Particles with the OSQAR and ALPS II experiments”. PhD thesis. Mainz, 2018. DOI: http://doi.org/10.25358/openscience-2629 (cit. on p. 44).

[100] Hervé Abdi and Lynne J Williams. “Principal component analysis”. In: *Wiley interdisciplinary reviews: computational statistics* 2.4 (2010), pp. 433–459 (cit. on p. 53).

[101] Peter C Humphreys et al. “Tomography of photon-number resolving continuous-output detectors”. In: *New Journal of Physics* 17.10 (2015), p. 103044. DOI: 10.1088/1367-2630/17/10/103044 (cit. on p. 53).

[102] Zachary H. Levine et al. “Algorithm for finding clusters with a known distribution and its application to photon-number resolution using a superconducting transition-edge sensor”. In: *J. Opt. Soc. Am. B* 29.8 (2012), pp. 2066–2073. DOI: 10.1364/JOSAB.29.002066 (cit. on p. 56).

[103] Peizhi Du et al. *Sources of Low-Energy Events in Low-Threshold Dark Matter Detectors*. 2020. arXiv: 2011.13939 [hep-ph] (cit. on p. 59).

[104] Blas Cabrera et al. “Cryogenic detectors based on superconducting transition-edge sensors for time-energy-resolved single-photon counters and for dark matter searches”. In: *Physica B: Condensed Matter* 280.1 (2000), pp. 509–514. DOI: https://doi.org/10.1016/S0921-4526(99)01849-9 (cit. on p. 59).

[105] Aaron J. Miller et al. “Demonstration of a low-noise near-infrared photon counter with multiphoton discrimination”. In: *Applied Physics Letters* 83.4 (2003), pp. 791–793. DOI: 10.1063/1.1596723. eprint: https://doi.org/10.1063/1.1596723 (cit. on p. 59).

[106] Yonit Hochberg et al. “Superconducting Detectors for Superlight Dark Matter”. In: *Phys. Rev. Lett.* 116 (1 2016), p. 011301. DOI: 10.1103/PhysRevLett.116.011301 (cit. on p. 60).

[107] Yonit Hochberg et al. “Detecting Sub-GeV Dark Matter with Superconducting Nanowires”. In: *Phys. Rev. Lett.* 123 (15 2019), p. 151802. DOI: 10.1103/PhysRevLett.123.151802 (cit. on p. 60).

[108] Hartmut Grote and Jan Hendrik Põld. “ALPS II Design Requirement Document”. In: *Internal Communication* (2019) (cit. on p. 61).

[109] S.I. Bityukov and N.V. Krasnikov. “On the observability of a signal above background”. In: *Nuclear Instruments and Methods in Physics Research Section A: Accelerators, Spectrometers, Detectors and Associated Equipment* 452.3 (2000), pp. 518–524. DOI: https://doi.org/10.1016/S0168-9002(00)00454-X (cit. on p. 61).

[110] Adriana E. Lita et al. “Counting near-infrared single-photons with 95%”. In: *Opt. Express* 16.5 (2008), pp. 3032–3040. DOI: 10.1364/OE.16.003032 (cit. on p. 82).

[111] M Schmidt et al. “Photon-number-resolving transition-edge sensors for the metrology of quantum light sources”. In: *Journal of Low Temperature Physics* 193.5 (2018), pp. 1243–1250 (cit. on pp. 82, 84).

[112] D Rosenberg et al. “Near-unity absorption of near-infrared light in tungsten films”. In: *Nuclear Instruments and Methods in Physics Research Section A: Accelerators, Spectrometers, Detectors and Associated Equipment* 520.1 (2004). Proceedings of the 10th International Workshop on Low Temperature Detectors, pp. 537–540. DOI: https://doi.org/10.1016/j.nima.2003.11.308 (cit. on p. 82).

[113] Marco López et al. “Detection efficiency calibration of single-photon silicon avalanche photodiodes traceable using double attenuator technique”. In: *Journal of Modern Optics* 62.20 (2015). PMID: 25892852, pp. 1732–1738. DOI: 10.1080/09500340.2015.1021724. eprint: https://doi.org/10.1080/09500340.2015.1021724 (cit. on p. 83).

[114] Aaron J Miller et al. “Superconducting photon number resolving detectors: Performance and promise”. In: *Proc. 8th Int. Conf. Quantum Communication, Measurement and Computing (QCMC’06)*. 2007, pp. 445–450 (cit. on p. 86).

[115] Christina Schwemmbauer. “Cold filtering of photons for a TES detector”. In: *Internal Communication, Summer Student Report, DESY* (2019) (cit. on p. 88).

[116] Julian Dietz. “Thermal effects in the detection of single photons”. In: *Bachelor Thesis* (2021) (cit. on p. 88).

[117] John A Jay. “An overview of macrobending and microbending of optical fibers”. In: *White paper of Corning* (2010), pp. 1–21 (cit. on p. 88).

[118] R. C. G. Smith et al. “Direct measurement of bend-induced mode deformation in large-mode-area fibers”. In: *Opt. Express* 20.4 (2012), pp. 4436–4443. DOI: 10.1364/OE.20.004436 (cit. on p. 89).

[119] Carolin Kohl. “Internship Report”. In: *Internal Communication* (2020) (cit. on p. 91).

[120] Klaus Zenker. “Construction of a filter bench for ALPS II”. In: *Internal Communication* (2017) (cit. on p. 90).

[121] O V Lounasmaa. “Dilution refrigeration”. In: *Journal of Physics E: Scientific Instruments* 12.8 (1979), pp. 668–675. DOI: 10.1088/0022-3735/12/8/001 (cit. on p. 97).

[122] John C. Wheatley et al. “Principles and methods of dilution refrigeration”. In: *Physics Physique Fizika* 4 (1 1968), pp. 1–64. DOI: 10.1103/PhysicsPhysiqueFizika.4.1 (cit. on p. 97).

[123] K.W. Taconis. “Dilution refrigerators”. In: *Physica B+C* 109-110 (1982). 16th International Conference on Low Temperature Physics, Part 3, pp. 1753–1763. DOI: https://doi.org/10.1016/0378-4363(82)90198-X (cit. on p. 97).

[124] H. London et al. “Osmotic Pressure of He^3 in Liquid He^4, with Proposals for a Refrigerator to Work below 1°K”. In: *Phys. Rev.* 128 (5 1962), pp. 1992–2005. DOI: 10.1103/PhysRev.128.1992 (cit. on p. 97).

[125] Ray Radebaugh et al. “Development of the pulse tube refrigerator as an efficient and reliable cryocooler”. In: *Proc. Institute of Refrigeration (London)* 1999 (2000), p. 00 (cit. on p. 98).

[126] Matthew D. Schwartz. “Modern Machine Learning and Particle Physics”. In: *Harvard Data Science Review* 3.2 (May 13, 2021). https://hdsr.mitpress.mit.edu/pub/xqle7lat. DOI: 10.1162/99608f92.beeb1183 (cit. on p. 112).

Acknowledgements